Universidade Estadual de Londrina

GABRIEL DELONGUI POLVANI

VAZÃO, EFICIÊNCIA ENERGÉTICA E ESPECTRAL E EQUIDADE PARA PROTOCOLOS DE ACESSO ALEATÓRIOS AUXILIADOS POR RIS PARA REDES B5G DE COMUNICAÇÃO SEM FIO

LONDRINA
2025

GABRIEL DELONGUI POLVANI

VAZÃO, EFICIÊNCIA ENERGÉTICA E ESPECTRAL E EQUIDADE PARA PROTOCOLOS DE ACESSO ALEATÓRIOS AUXILIADOS POR RIS PARA REDES B5G DE COMUNICAÇÃO SEM FIO

Dissertação apresentada ao Programa de Mestrado em Engenharia Elétrica da Universidade Estadual de Londrina para obtenção do título de Mestre em Engenharia Elétrica.

Orientador: Prof. Dr. Taufik Abrão

LONDRINA
2025

Ficha de identificação da obra elaborada pelo autor, através do Programa de Geração Automática do Sistema de Bibliotecas da UEL

Polvani, Gabriel Delongui.
Vazão, Eficiência Energética e Espectral e Equidade para Protocolos de Acesso Aleatórios Auxiliados por RIS para Redes B5G de Comunicação sem Fio / Gabriel Delongui Polvani. - Londrina, 2025.
108 f.

Orientador: Taufik Abrão.
Dissertação (Mestrado em Engenharia Elétrica) - Universidade Estadual de Londrina, Centro de Tecnologia e Urbanismo, Programa de Pós-Graduação em Engenharia Elétrica, 2025.
Inclui bibliografia.

1. Superfícies inteligentes reconfiguráveis - Tese. 2. Eficiência espectral - Tese. 3. Eficiência energética - Tese. 4. Protocolos de acesso aleatório - Tese. I. Abrão, Taufik. II. Universidade Estadual de Londrina. Centro de Tecnologia e Urbanismo. Programa de Pós-Graduação em Engenharia Elétrica. III. Título.

CDU 62

GABRIEL DELONGUI POLVANI

VAZÃO, EFICIÊNCIA ENERGÉTICA E ESPECTRAL E EQUIDADE PARA PROTOCOLOS DE ACESSO ALEATÓRIOS AUXILIADOS POR RIS PARA REDES B5G DE COMUNICAÇÃO SEM FIO

Dissertação apresentada ao Programa de Mestrado em Engenharia Elétrica da Universidade Estadual de Londrina para obtenção do título de Mestre em Engenharia Elétrica.

BANCA EXAMINADORA

Orientador: Prof. Dr. Taufik Abrão
Universidade Estadual de Londrina

Prof. Dr. Richard Demo de Souza
Universidade Federal de Santa Catarina – UFSC

Prof. Dr. Cristiano Magalhães Panázio
Escola Politécnica da Universidade de São Paulo – EPUSP

Londrina, 27 de Fevereiro de 2025.

Dedico esta Dissertação de Mestrado à todas as pessoas que, de alguam forma, me incentivaram e contribuíram com o processo.

AGRADECIMENTOS

Primeiramente, agradeço a Deus pela vida. Agradeço a minha família pelo apoio durante todo este Mestrado e pelo exemplo de vida proporcionado. Agradeço aos professores do Programa de Mestrado em Engenharia Elétrica da UEL, em especial ao meu orientador Taufik Abrão por toda sua orientação, dedicação, apoio e incentivo durante toda a pesquisa desenvolvida no Laboratório de Telecom & DSP-UEL. É inegável que seu apoio foi de extrema importância para a conclusão deste Mestrado.

Agradeço aos meus colegas de laboratório pelos momentos de descontração, pelo apoio na realização desta Dissertação e pelas discussões técnicas e sugestões enriquecedoras proporcionadas por eles. Agradeço o apoio financeiro proporcionado pela CAPES, concedido via bolsa de estudos DS[1], a qual possibilitou o desenvolvimento desta pesquisa. Agradeço também aos Professores Dr. Richard Demo de Souza e Dr. Cristiano Magalhães Panázio pela disponibildiade de participação das bancas de Qualificação e Defesa desta Dissertação de Mestrado e pelas valiosas sugestões e orientações concedidas durante todo o processo.

[1] Processo #88887.808193/2023-00

"Entrega o teu caminho ao Senhor; confia nele, e ele o fará." – Salmos 37:5

POLVANI, G. D.. **Vazão, Eficiência Energética e Espectral e Equidade para Protocolos de Acesso Aleatórios Auxiliados por RIS para Redes B5G de Comunicação sem Fio**. 2025. 108f. Dissertação (Mestrado em Engenharia Elétrica) – Universidade Estadual de Londrina, Londrina, 2025.

RESUMO

Nos últimos anos, a tecnologia conhecida como Massive Multiple-Input-Multiple-Output (M-MIMO) foi implantada globalmente, inaugurando a era da quinta geração de redes de comunicação sem fio (5G). Inúmeros benefícios oferecidos pelo 5G, como maior conectividade, maior eficiência espectral e energética, estão agora sendo aproveitados por aplicações sem precedentes. No entanto, empresas e pesquisadores já estão vislumbrando as redes 6G, antecipando novas aplicações como Indústria 4.0, turismo em águas profundas e espacial, realidade estendida (XR) e controle ambiental inteligente. Essas aplicações poderiam ser facilitadas por técnicas de inteligência artificial (IA) ou dispositivos inovadores como Superfícies Inteligentes Reconfiguráveis (RIS). Além disso, essas novas aplicações devem ser projetadas de forma eficiente para estender os benefícios do 5G, utilizando inteligentemente os recursos escassos e promovendo cenários de comunicação sem fio que aderem aos ideais de comunicações verdes. No entanto, o crescente número de dispositivos conectados, a verticalização urbana, a mobilidade dos usuários e os efeitos de propagação física, especialmente em frequências mais altas, impõem desafios para a modelagem precisa do sistema. Portanto, há uma necessidade urgente de desenvolver modelos de canal precisos e algoritmos inteligentes capazes de enfrentar esses cenários complexos. Isso permitirá uma investigação precisa do desempenho do 6G e da viabilidade de novas tecnologias como as RIS. Alinhada com esses objetivos, esta dissertação de mestrado foca em três objetivos principais: 1) apresentar um modelo de canal flexível para redes 6G auxiliadas por RIS, enfatizando aplicações em Comunicações Massivas de Tipo Máquina (mMTC); 2) estudar o design de protocolos de acesso aleatório de baixa complexidade auxiliados por RIS para aplicações em cenários onde as condições de canal dos usuários são bastante discrepantes; e 3) explorar estratégias de alocação de potência para cenários de mMTC a fim de melhorar a eficiência energética geral do sistema, crucial para dispositivos com capacidade de bateria limitada. Este trabalho fornece insights valiosos para o design de protocolos de acesso aleatório eficientes e sustentáveis para redes sem fio futuras de mMTC. Especificamente, desenvolvemos e validamos modelos de canal realistas que incorporam links diretos e refletidos auxiliados por RIS. Dois novos protocolos de acesso aleatório foram estudados: SAP-RARAP (política de acesso único) e DAP-RARAP (política de acesso duplo). O DAP-RARAP seleciona dinamicamente uma política de acesso e a potência de transmissão para cada MTD com base nas informações do estado do canal (CSI) e na localização dentro da célula. Extensivas simulações Monte-Carlo avaliaram o throughput (vazão), a eficiência espectral (SE), a eficiência energética (EE) e a equidade, revelando vantagens significativas de desempenho do DAP-RARAP em diversos cenários. O impacto de parâmetros-chave, como o número de elementos RIS, slots de tempo, potência de transmissão dos MTDs e atenuação por bloqueio, foi investigado sistematicamente.

Palavras-chave: Superfícies inteligentes reconfiguráveis. Eficiência espectral. Eficiência energética. Protocolos de acesso aleatório.

POLVANI, G. D.. **Throughput, Energy and Spectral Efficiency and Fairness for RIS-Aided Random Access Protocols for B5G Wireless Communications Networks.**. 2025. 108p. Master's Thesis (Master in Electrical Engineering) – State University of Londrina, Londrina, 2025.

ABSTRACT

In recent years, the so-called Massive Multiple-Input-Multiple-Output (M-MIMO) technology has been deployed globally, ushering in the fifth generation of wireless communication networks (5G). Numerous benefits offered by 5G, such as increased connectivity and higher spectral and energy efficiency, are now being leveraged by unprecedented applications. However, companies and researchers are already envisioning 6G networks, anticipating new applications such as Industry 4.0, deep-sea and space tourism, extended reality (XR), and smart environmental control. These applications could be facilitated by artificial intelligence (AI) techniques or innovative devices like Reconfigurable Intelligent Surfaces (RIS). Moreover, these new applications must be efficiently designed to extend the benefits of 5G, intelligently utilizing scarce resources and promoting wireless scenarios that adhere to green communications ideals. Nevertheless, the growing number of connected devices, urban verticalization, user mobility, and physical propagation effects, particularly at higher frequencies, pose challenges for precise system modeling. Therefore, there is an urgent need to develop accurate channel models and intelligent algorithms capable of addressing these complex scenarios. This will enable precise investigation of 6G performance and the feasibility of new technologies such as RIS. In line with these goals, this master's thesis focuses on three main attainable objectives: 1) present a flexible channel model for RIS-aided 6G networks, emphasizing applications in Massive Machine-Type Communications (mMTC); 2) studying the design of low-complexity RIS-aided random access protocols for scenarios where users' channel conditions are discrepant; and 3) exploring power allocation strategies for mMTC scenarios to enhance overall system energy efficiency, crucial for devices with limited battery capacity. This work provides valuable insights into designing efficient and sustainable mMTC random access protocols for future wireless networks. Specifically, we developed and validated realistic channel models incorporating RIS-aided direct and reflected links. Two novel random access protocols were studied: SAP-RARAP (single access policy) and DAP-RARAP (double access policy). DAP-RARAP dynamically selects an access policy and transmission power for each MTD based on channel state information (CSI) and location within the cell. Extensive Monte Carlo simulations evaluated throughput, spectral efficiency (SE), energy efficiency (EE), and fairness, revealing DAP-RARAP's significant performance advantages in various scenarios. The impact of key parameters, such as the number of RIS elements, time slots, MTD transmit power, and blockage attenuation, was systematically investigated.

Keywords: Reconfigurable intelligent surfaces. Spectral efficiency. Energy efficiency. Random access protocols.

LIST OF FIGURES

LIST OF TABLES

LIST OF ABBREVIATIONS AND ACRONYMS

ACBPC	Access class barring with power control
AI	Artificial Intelligence
AP	Access Point
B5G	Beyond the Fifth Generation
BS	Base Station
CARP	Configuration-Aware Random Access Policy
CRDSAP	Contention Resolution Diversity Slotted ALOHA Policy
CSI	Channel State Information
DL	Downlink
DAP-RARAP	Double Access Policy RIS-Aided Random Access Protocol
EE	Energy Efficiency
eMBB	Enhanced Mobile Broadband
GB	Grant-Based
GF	Grant-Free
hRLLC	Hyper Reliable and Low Latency Communication
IoT	Internet of Things
IRS	Intelligent Reflective Surface
IRSAP	Irregular Repetition Slotted ALOHA Policy
ITU	International Telecommunication Union
LoS	Line-of-Sight
MCS	Monte Carlo Simulation
ML	Machine Learning
M-MIMO	Massive Multiple-Input Multiple-Output
MTD	Machine-Type Device

mMTC	Massive Machine-Type Communications
NOVR-XL	Non-Overlapping VR XL-MIMO
nLoS	Non-Line-of-Sight
QoS	Quality of Service
RA	Random Access
RIS	Reconfigurable Intelligent Surface
SAP-RARAP	Single Access Policy RIS-Aided Random Access Protocol
SCP	Strongest Configuration Policy
SE	Spectral Efficiency
SIC	Successive Interference Cancellation
SNR	Signal to Noise Ratio
s-SCP	s-Strongest Configurations Policy
SUCRe	Strongest User Collision Resolution
TDMA	Time Division Multiple Access
UL	Uplink
URLLC	Ultra-Reliable and Low Latency Communication
VR	Visibility Regions
XL-MIMO	Extra-Large Scale Multiple-Input-Multiple-Output
XR	Extended Reality

LIST OF SYMBOLS

K	Number of Contending MTDs
d_{BS}	BS distance from the origin
θ_{BS}	BS angle
d_k	k-th MTD distance from the origin
θ_k	k-th MTD angle
d_k^d	Distance from the BS and the k-th MTD
N	Number of RIS elements
N_x	Number of RIS elements along the x-axis
N_z	Number of RIS elements along the z-axis
$\boldsymbol{\Theta}$	Set of predefined RIS configurations
C	Number of RIS predefined configurations
θ_c	c-th RIS configuration
S	Number of training time slots
J	Number of access time slots
$h_k[s, \theta_k]$	Channel coefficient of MTD k
$h_k^d[s, \theta_k]$	Direct link channel coefficient of MTD k
$h_k^r[s]$	Reflected link channel coefficient of MTD k
β_k^d	Path loss of the direct link of MTD k
κ	Direct link Rice factor
$\overline{h}_k^d$	LoS component of the direct link of MTD k
$\tilde{h}_k^d[s]$	nLoS component of the direct link of MTD k
j	The imaginary unit, $j = \sqrt{-1}$
ψ_k^d	Direct link total phase shift
ω	Angular frequency or wavenumber

λ	Carrier wavelength
$\mathcal{CN}(0,1)$	Circular symmetric random variable of zero mean and unit variance
ξ	Blockage attenuation
α_{BS}	BS andtenna gain
α_k	k-th MTD antenna gain
$u(\cdot)$	Unit step function
β_k^r	Path loss of the reflected link of MTD k
δ	Reflected link Rice factor
$\overline{h}_k^r[s]$	LoS component of the reflected link of MTD k
$\tilde{h}_k^r[s]$	nLoS component of the reflected link of MTD k
ψ_k^r	Reflected link total phase shift
$\Omega_k[s]$	RIS' array factor for MTD k at time slots s
d_x	Size of a RIS element along the x-axis
d_z	Size of a RIS element along the z-axis
T_{ts}	Duration of each training slot
T_{as}	Duration of each access slot
T_σ	Duration of sigma slot
T_t	Duration of the downlink training phase of the TDMA frame
T_a	Duration of the uplink access phase of the TDMA frame
T_f	Total duration of the TDMA frame
$(\Delta T)_c$	Channel coherence time
n_k	Number of packet replicas sent by MTD k
ρ_{BS}	BS transmit power
ρ_{MTD}	MTD transmit power
τ	Pilot length
$\boldsymbol{\phi}$	Pilot signal

$\mathbf{n}_k[s]$	k-th AWGN noise at the MTD's receiver
σ^2_{MTD}	MTDs' noise variance
$\mathbf{I}$	Identity matrix
$\mathbb{E}\{\cdot\}$	Expectation operator
$\mathbf{y}^{tr}_k[s]$	Training signal received by MTD k at training slot s
$\hat{h}_k[s]$	Estimated channel coefficient of MTD k
$q_k[s]$	Channel quality of MTD k at training slot s
$\mathbf{y}[s]$	Uplink signal received by the BS at access slot s
τ_d	Length of uplink data symbols
$\mathbf{x}_k$	Transmitted symbols by MTD k
$\mathbf{n}[s]$	k-th AWGN noise at the BS' receiver
σ^2_{BS}	BS noise variance
$\mathcal{A}$	Set of available access policies for DAP-RARAP
$A_1 \in \mathcal{A}$	DAP-RARAP CSI-aided policy
$A_2 \in \mathcal{A}$	DAP-RARAP non-CSI-aided policy
$\mathcal{P}$	Set of available uplink power levels for DAP-RARAP
$\rho_{\text{L}} \in \mathcal{P}$	DAP-RARAP's low uplink power sub-level
$\rho_{\text{H}} \in \mathcal{P}$	DAP-RARAP's high uplink power sub-level
σ^2_{TH}	DAP-RARAP's localization threshold
σ^2_k	DAP-RARAP's localization coefficient estimated by MTD k
$z_k[s]$	Normalized channel quality of MTD k at slot s
$p_k[s]$	Probability of MTD k sending a replica in slot s when CARP is adopted
$E^{\text{DL}}_{\text{BS}}$	BS transmit energy
$E^{\text{DL}}_{\text{MTD},k}$	k-th MTD transmit energy
$\dot{P}_{\text{BS}}$	BS power consumption rate
$\dot{P}_{\text{MTD}}$	MTD's power consumption rate

$\dot{P}_n$	Power consumption rate of a single RIS element
μ_{BS}	BS power amplifier inefficiency
P_{BS}	BS total power consumption
μ_{MTD}	MTD's power amplifier inefficiency
$P_{\text{MTD},k}$	k-th MTD total consumed power
P_{RIS}	RIS total power consumption
P_{T}	System total power consumption
G	System throughput, given in packets/s.
A	Number of MTD's packets successfully decoded by the BS in a TDMA frame
η_{T}	System total EE, given in packets/J
η_{MTD}	MTD's EE, given in packets/J
$J(\mathbf{x})$	Jain's fairness index
G_k	Indicator of MTD's k packet's successful detection
γ_k	SNR of MTD k
x_k	SE of MTD k, given in bps/Hz.

CONTENTS

1 INTRODUCTION AND MOTIVATION

Back in 2017, Report ITU-R M.2410-0 published by the International Telecommunication Union (ITU) established the minimum requirements for IMT-2020 radio interfaces [1]. These usage scenarios were defined almost a decade ago by Report ITU-R M.2083-0 [2], and include *ultra reliable and low latency communications* (URLLC), *enhanced mobile broadband* (eMBB) and *massive machine type communications* (mMTC) as the three main vertices of 5G networks. Nowadays, with the commercial development of multi-antenna base stations (BS) and its implementation in many countries, 5G has become a reality, especially due to the *massive multiple-input multiple-output* (M-MIMO) technology [3].

However, despite all the benefits achieved with 5G networks, the increasing number of wireless devices, mobility, and data traffic, combined with the scarcity of resources, indicates that M-MIMO technology alone cannot fulfill the expected requirements beyond 5G (B5G) networks. Because of that, future wireless communications networks must be carefully designed, enhancing current 5G usage scenarios and allowing the viability of new ones. For instance, the evolution of mMTC must handle a connection density of up to 100 million devices/km^2. Report ITU-R M.2160-0 defines this evolution as *hyper-reliable and low-latency communications* (hRLLC), and envisages applications such as smart cities, transportation, logistics, health, energy, environmental monitoring and agriculture [4]. To allow hRLLC, this usage scenario would require support to distinct data rates, extremely low power consumption, extended coverage and high connection density, which poses several challenges in developing new random access protocols and suitable power allocation schemes. In this regard, B5G expects the implementation of new BS topologies, revolutionary devices, and artificial intelligence (AI) integration, which can provide remarkable performance gains for many users while smartly managing available resources, such as power, time, and/or spectrum.

Among the novel candidates for BS topologies are the so-called cell-free M-MIMO [5] and the extra-large scale MIMO (XL-MIMO). Cell-free M-MIMO replaces the M-MIMO BS with many access points (APs) within the communication cell, aiming for better coverage and a higher energy efficiency [6]. On the other hand, XL-MIMO consists of incorporating a massive number of antennas in buildings structures, such as building facades, shopping malls and airport walls, football stadium grandstands, and factory ceilings, expanding the benefits of M-MIMO to an even higher number of users. However, in the last few years, *reconfigurable intelligent surfaces* (RIS) emerged as a promising technology for B5G.

In short, an RIS is a planar array made of many reflective elements that can be

externally configured to reflect the impinging electromagnetic wave in specific directions. The main advantage of these devices is that they can improve the spectral efficiency (SE) without consuming a high amount of power, as long as it was initially designed only to *reflect* the received signal, not performing any signal processing operation, such as channel estimation or power amplification. Further discussions about those devices are provided in Chapter 3.

This master's Thesis focuses on developing solutions for mMTC scenarios. These scenarios are critical in future wireless systems due to the proliferation of IoT devices and the need for efficient communication protocols. The proposed solutions in this Dissertation intend to explore novel random access (RA) protocols, integrate them with efficient power allocation strategies, and leverage the functionalities of RIS. This approach aims to optimize B5G communication performance in mMTC environments, aligning with the evolving requirements of future wireless networks.

1.1 Motivation

The motivations for developing (or extending) new *random access protocols* are related to meeting the communication demands in mMTC scenarios, where a significant increase in device density is expected. New protocols must efficiently manage scarce resources such as power, time, and spectrum while ensuring reliable communication with low latency. Additionally, integrating artificial intelligence (AI) techniques and adapting to varying channel conditions are essential for enhancing energy and spectral efficiency.

The motivations for adopting the *transmission topology of Massive MIMO Systems aided by RIS* include the ability to improve spectral efficiency (SE) without consuming a high amount of energy, as RISs are designed to reflect signals without performing signal processing. This approach allows for the creation of a "virtual line-of-sight" between users and the base station, enhancing channel quality and extending transmission distances. Furthermore, using RIS is a promising solution to meet the technical expectations of B5G applications, promoting green and sustainable communications.

Finally, the general motivation for developing new channel models stems from the need to address new system and channel scenarios, new configurations in terms of the increasing number of connected devices, urban verticalization, user mobility, and physical propagation effects, particularly at higher carrier frequencies, e.g., new 15GHz-based spectrum and mmWave spectrum. These factors pose challenges for accurate system modeling, creating an urgent need for precise channel models and intelligent algorithms capable of tackling complex scenarios. This will enable accurate investigations of 6G performance and the feasibility of new technologies such as RIS-aided mMIMO systems.

1.2 Master Thesis Objectives

This master's thesis aims to provide crucial contributions to the development of new solutions to mMTC scenarios, specially those envisioned for B5G networks. These objectives are mainly related to physical aspects of the communication channel and are specifically listed in the following:

1) **General:** develop channel models for B5G mMTC networks and new random access protocols. The channel modeling and protocol design do not neglect fundamental physical principles and leverage new promising 6G technologies, enabling numerical simulations capable of precisely representing the achievable limits of 6G networks.

2) **Specific:**

   a) Reproduce recently developed channel models and random access protocols to establish benchmarks for this thesis's proposed schemes.

   b) Develop or extend new channel models and random access protocols aided by RISs, envisioning a comprehensive and consistent analysis of B5G scenario's performance. The main performance metrics exploited are spectral and energy efficiencies.

1.3 Methodology

The channel models and RA protocols proposed in this thesis have been studied and compared by numerical simulations developed in *Python*. Those simulations were carefully designed to represent the main physical aspects of a wireless communication system, including small and large-scale fading, additive white Gaussian noise (AWGN) at the receiver, RIS modeling, and randomnesses regarding the MTDs positions at the communication cell. The Monte-Carlo simulations (MCS) approach has been applied to evaluate the SE and EE performance metrics.

1.3.1 Monte Carlo simulations (MCS)

Numerical results for the wireless channel and the analyzed random access protocols were rigorously validated through MCS. These simulations were designed to accurately represent the main physical aspects of a wireless communication system, including considerations of small and large-scale fading, additive white Gaussian noise (AWGN) at the receiver, RIS modeling, and the randomness regarding Machine-Type Devices (MTDs) positions within the communication cell. The MCS approach ensures a comprehensive evaluation of the performance metrics, thereby guaranteeing that the simulations accurately reflect the achievable limits of the proposed protocols and channel models.

1.3.2 Performance metrics

These metrics collectively provide a comprehensive view of the performance and effectiveness of the proposed channel models and random access protocols in the context of B5G wireless communications. The **performance metrics** used in the analysis include:

Throughput indicates the actual rate of successful message delivery over a communication channel, measured in packets per second. It provides insight into the performance of the random access protocols under varying conditions. Notice that this metric is an "alternative" way to compute the system SE.

Energy Efficiency (EE) evaluates the amount of data transmitted per unit of energy consumed, usually expressed in bits per Joule (bps/J). It is crucial for assessing the sustainability of communication protocols, especially for devices with limited battery capacity.

Fairness assesses the equity of access among different users in the network, typically measured by the difference in probabilities of successful access attempts between different groups of MTDs. It helps to evaluate how well the protocols ensure fair resource allocation among users.

1.4 Thesis Outline

This thesis is divided into chapters that present the main fundamentals of the concepts adopted throughout this Master's Dissertation. Specifically, Chapters 2 and 3 present a summary of RA protocols and introduce RIS technology, respectively. The scenario setup is presented in Chapter 4, which embraces the channel model, the RIS and RA protocols functionality and integration with the TDMA frame and also the adopted access policies performed by MTDs. Finally, Chapter 5 presents the contributions of this work with a comprehensive discussion regarding the obtained simulation results. The discussion includes the definition of feasible simulation parameters in order to truly represent a real scenario and the simulation results obtained via MCS. Several system parameters vary in order to investigate the RA protocol's behavior in vast application scenarios. The conclusions and research directions of this Master's Dissertation are summarized in Chapter 6.

2 RANDOM ACCESS PROTOCOLS FOR B5G NETWORKS

In this Chapter, we present a brief review of RA protocols proposed for M-MIMO and XL-MIMO networks and a discussion of some protocols being developed for B5G networks, leveraging RIS technology. Because this last topic is the main focus of this Dissertation, we present details of the studied B5G RA protocols, specifically w.r.t. access rules that can be used during the access phase by MTDs, how the RIS functionality can be integrated with the protocols, and channel models adopted. Literature gaps regarding B5G RA protocols are highlighted, and new solutions are proposed throughout this work.

2.1 Random Access Protocols for 5G: A Review

The increasing number of wireless devices imposes several challenges for B5G wireless networks. Next-generation systems must increase system reliability while handling many users with extremely low latency, allowing the implementation of promised B5G applications, such as industry 5.0 [7]. It is expected that B5G networks must be able to serve up to 10^8 users per km^2 [4], with many of those users being wireless sensors, which are essential for Internet of Things (IoT) scenarios.

MTC scenarios are composed of a high number of sensors and IoT devices that must operate with minimal or without any human interference [8]. Those scenarios are becoming rapidly denser with the development and implementation of 5G cellular generation. Due to this, when an MTC scenario serves a massive number of devices, we have a dense MTC-like scenario, called mMTC scenario. Resource allocation is a particularly relevant problem for this scenario because it is impossible to assign orthogonal pilot sequences for all of them due to the higher number of users. Furthermore, power allocation must be efficiently made to avoid unnecessary energy consumption by sensors with a limited battery budget. Finally, the available spectrum must be used adequately to maximize spectral efficiency and support higher data traffic.

For 5G and B5G networks, several RA protocols have been developed recently, considering not only M-MIMO scenarios but also the novel XL-MIMO arrangements. RA protocols can be divided into two classes: grant-based and grant-free. A grant-based (GB) protocol requires BS feedback, allowing users to transmit its data. On the other hand, such a concession is unnecessary in grant-free (GF) protocols. Therefore, one can say that the development of GF protocols is paramount for 5G networks because, as long as the BS feedback is not required, the data transmission occurs with lower latency. In [9], an RA protocol that can take advantage of the M-MIMO properties is proposed. On one hand, the protocol was able to resolve up to 90% of the collisions in a decentralized way;

on the other hand, the decision rule adopted to accept or deny new devices in the network privileges users near the BS, due to its higher received power when compared to cell-edge devices. Hence, due to the lack of fairness, it can be mentioned that the proposed protocol, called *strongest user collision resolution* (SUCRe) protocol, is not optimal for B5G.

Despite the unfair cell coverage of the SUCRe protocol, one can say that it was a success due to its effectiveness in resolving collisions in a decentralized way and also because many variants were developed later [10, 11, 12, 13], aiming to attain even better performance and solve the fairness problem. In [10], the idle pilot access (IPA) technique was combined with SUCRe. In the proposed SUCR-IPA, the BS can identify unused pilots and provide feedback to the users on the indices of these sequences with an access class barring (ACB) factor, allowing the weakest users to try a new connection attempt using one of those unused pilots. Simulation results show that SUCR-IPA can achieve a better performance than SUCRe. Despite that, an extra control overhead is inevitable when assigning unused pilots to new users, causing a latency increase regarding the baseline protocol.

The BS broadcast the indices of non-used pilots is also explored in [11]. Users not allowed to transmit data after the first attempt can choose a random pilot from those sent by the BS. Differently from [10], in [11], the ACB factor is not sent to users. The channel estimation of each user channel is performed by a successive interference cancellation (SIC) algorithm based on a bipartite graph, which is made by considering active UEs as variable nodes and selected pilots as factor nodes. This SUCRe variant is named SUCRe combined graph-based pilot access (SUCR-GBPA). This approach presents a higher overhead due to the retransmission of idle pilots and needs more complex signal processing at BS. Despite that, SUCR-GBPA achieved a higher throughput than SUCR-IPA and SUCRe. New retransmission rules, usually performed before step 3 of the original SUCRe protocol, have already been developed. In [12], a soft probabilistic retransmission rule is proposed by considering the probability of a given user being the strongest user. The decision, as in the original protocol, is made decentralized, and simulation results show that the performance of soft SUCRe is better than the original protocol, especially in overcrowded scenarios.

An access class barring with power control (ACBPC) protocol was developed in [13]. The proposed approach reveals remarkable improvements when compared with SUCRe [9], such as higher EE and a higher probability of resolving pilot collisions with many contenders. More importantly, the ACBPC protocol achieved fairness for all cell users, independent of their distances to the BS, which was impossible to attain with the original SUCRe protocol. This was achieved by a power allocation scheme that assigns, for each user, a power inversely proportional to the channel gain between the respective user and the BS.

The previous protocols were developed for typical M-MIMO scenarios. Hence, none of the cited works adopted sub-array signal processing and non-stationary effects. More recently, in [14], the protocol proposed in [9] was redesigned for an XL-MIMO scenario. By exploiting the spatial non-stationarities of XL-MIMO channels, this adapted protocol could reduce latency and handle a higher number of connected devices simultaneously. Although this higher connectivity, the main drawback of SUCRe was also noted in this new protocol: the quality of service (QoS) was not the same for all users. The same authors of [14] further studied the fairness problem in crowded XL-MIMO systems in [15], where the ACBPC protocol was also adapted for XL-MIMO scenarios. Simulation results have demonstrated a connectivity improvement in more than 70%.

Spatial non-stationarities, which is a physical effect detailed in [16] that affects extremely large antenna arrays, can also be used for pilot reusing, as done in [17]. In this paper, the authors proposed an RA protocol for XL-MIMO systems where only two steps are necessary, drastically reducing the data overhead. Furthermore, due to the huge BS array aperture, different users can use the same pilot, as long as their visibility regions (VR) do not overlap, without suffering any interference. The proposed protocol is called Non-Overlapping VR XL-MIMO protocol (NOVR-XL), and was compared with the previously developed SUCRe-XL protocol via numerical simulations, and was able to attain lower latency, a higher number of simultaneously connected users and, consequently, a higher sum-rate.

Hybrid scenarios, used simultaneously by machine-type devices (*e.g.*: sensors and other IoT devices) and human-type devices (such as smartphones) have been studied in [18]. Two types of receiver schemes for this specific scenario were proposed, both of them relying on grant-free RA. Simulation results reveal that the proposed methods presented a good performance, being able to perform channel estimation, signal detection, and identification of machine-type device activation. Furthermore, RA protocols can be developed aiming to simultaneously serve devices with different requirements. In [19], it was shown that the system throughput could be increased while allowing the coexistence of devices that perform applications from different usage scenarios - mMTC and URLLC. The proposed solution lies in applying a neural network (NN) traffic predictor combined with an ACB-based procedure, slightly increasing the overhead but considerably augmenting the number of packets decoded in a single RA frame.

Considering GF protocols, one can say that most of them are variants from the well-know ALOHA RA protocol [20]. In this original protocol, transmitting units selects a random time slot within a frame to send its data packet. If its packet is successfully decoded, BS responds with an ACK. If a transmitting unit do not receives an ACK, it tries to retransmit its data in the next coherence blocks until a time-out is exceeded. When it happens, the transmission failed. A problem with the original ALOHA RA protocols

is its lack of synchronization: devices are allowed to initiate a transmission anytime, which augments the collision probability. To solve that problem, slotted ALOHA [21] was developed. In slotted-ALOHA, the TDMA frame is divided in smaller sub-slots, and transmitting units are allowed to initiate a transmission only ate the beginning of each slot. By doing that, one can reduce the number of collisions observed, which enhances the overall system throughput.

Combining ALOHA-like protocols with successive interference cancellation (SIC) techniques, the system throughput can be enhanced even more. To address that, in [22], authors investigates the case where users are a allowed to transmit two copies of their packet, also refereed to as 'twin replicas'. The replicas are sent with pointers to their copies, such that when one of them is successfully decoded by the BS, SIC can subtract it from the slot where its replica was sent, allowing recursive decoding. This RA protocol is denoted contention resolution diversity slotted ALOHA (CRDSA) protocol. Further improvements in this RA technique are studied in [22], where a variable number of replicas selected from an specific random distribution by each device are sent. Due to the additional diversity, this technique was able to achieve a system throughput of almost 1 packet/slot, and was denoted irregular repetition slotted ALOHA (IRSAP). IRSA performance bounds and a trade-off study regarding its attainable EE and SE for Gaussian channels were provided in [23]. Works have already studied IRSA performance under the assumption that when a collision occurs in a slot, it can be resolved if the received power levels among the colliding signals is sufficiently different [24]. This approach allows to attain higher throughput performance in detriment of higher decoder complexity.

More recently, in [25], a low latency GF RA protocol was proposed. The presented method achieved exemplary performance and abdicates the need to use orthogonal pilot sequences, reducing the overhead needed for resource allocation in common RA grant-based protocols using Tanner graphs. This is only possible because the users access the network according to predefined scheduling, avoiding collisions, which is a suitable approach for traffic light control in smart city scenarios and industrial IoT environments, where many wireless sensors and devices must perform their tasks periodically. Despite its advantages, this new approach cannot be applied in scenarios where users need to request network access unpredictably due to the need for a predefined schedule to work correctly.

2.2 Random Access Protocols for B5G Networks

For B5G, some surveys stated crucial aspects for the development of novel RA protocols and solutions for mMTC scenarios. In [26] it is discussed that in the transition to 5G to 6G networks, it is crucial to establish new paradigms in the the deployment of B5G IoT networks. Sustainable solutions must be prioritized, leveraging green energy sources and efficient power management without neglecting security. In addition, mMTC

in B5G networks must be able to unlock a high amount of possibilities regarding new applications, such as in shipping environments, smart homes and smart cities, smart power systems, and agricultural monitoring [27]. However, to allow that, frequent updates to the cloud with low end-to-end costs are required, reinforcing the need to develop novel RA approaches.

Regarding RA protocols for B5G scenarios, more specifically those aided by RIS, the authors in [28] developed a power consumption model and an expression for the overall system EE for RIS-aided random access with a two time-scale GF RA protocol to handle the uplink transmissions. During each time slot of the RA protocol, the RIS covers a specific area of interest in the communication cell with a predefined set of phase-shift configurations, changing the channel qualities of the contending MTDs. Numerical results reveal that access policies that exploit information of the channel qualities are suitable for green IoT networks, simultaneously attaining competitive EE and throughput combined with low power consumption at the machine-type devices (MTDs) side.

3 RECONFIGURABLE INTELLIGENT SURFACES

A primordial assumption in the development of the first five wireless communications generations was that the channel where the signal propagates is established by nature and cannot be modified. However, 6G aims to break this paradigm thankfully to the development of technologies that can reshape electromagnetic waves, changing their phase shift and polarization and by absorbing, refracting, or reflecting them by adjusting their reflective elements through an external stimulus [29]. Those devices are mainly referred to as *reconfigurable intelligent surfaces* (RISs), although several other denominations for similar devices are already spread in the literature, such as intelligent reflective surfaces (IRS), large intelligent surfaces (LIS), and software controllable surfaces (SCS) [30]. These surfaces can be stacked in layers, potentially enhancing the system performance performance but also augmenting the modeling and its passive beamforming design complexity [31]. An example of an urban scenario equipped with an RIS is depicted in Figure 1. Several sensors are deployed around the city to monitor the environment, enhancing security, aiding traffic light control, and measuring air quality, temperature, and humidity, which is a typical smart city scenario. However, due to buildings and other environmental obstacles, the direct link between the sensors and the BS is completely blocked, severely harming the data transmission among them. To solve this problem, an RIS is installed on a building, allowing MTDs to communicate with the BS through a reflected link. Hence, RIS can create a 'virtual line-of-sight' between users and the BS, allowing partial control over the environment.

Specifically, RIS' are constructed using sheets of *metamaterials*, which have the unnatural ability to change their refraction coefficient when stimulated by different voltage levels. By adjusting patches of these metamaterials in a surface and integrating them with an external controller through a communication channel, one can modify the refraction coefficients of each surface element independently, allowing a partial environment control, which was impossible in previous wireless generations. Because of that, electromagnetic waves that interact with these surfaces can be specially designed to mitigate interference and increase cell coverage, SE, and security. Modeling these devices is challenging, and some simplifications were commonly adopted because of that. However, recently, a comprehensive and realistic RIS model has been published [32], highlighting the real challenges imposed by these surfaces, specially related to the optimization of its phase shifts design. Furthermore, RIS's primary functionalities do not involve signal processing or amplification, resulting in extremely low power consumption. Hence, one can say that RIS is a crucial technology to enable B5G applications, possibly fulfilling most technical expectations and adhering to green communications principles simultaneously. Several as-

pects regarding RIS modeling, its applications, and challenges for B5G are addressed in [33, 34]. Furthermore, a survey on RIS applications and its potential for future wireless communications systems are detailed in [35, 36], and fundamental concepts for terahertz communications, channel model and system designs for sensing applications, which might be tremendously enhanced with RIS technology, can be consulted in [37].

Several works have been published in the last few years aiming to explore the achievable performance of RIS-aided systems. Novel schemes, methods, and algorithms are being developed by researchers and companies, and some works have already presented remarkable results. For instance, [30] investigates the problem of EE and SE tradeoff in a multi-user RIS-aided scenario by optimizing the precoder and the RIS phase shifts using alternating optimization (AO) method. The proposed solution involves leveraging statistical and instantaneous channel state information (CSI) to achieve an optimal solution through an iterative minimal mean squared error minimization algorithm, resulting in remarkable SE and EE gains. An example of how RIS can be deployed in B5G networks envisioning performance gains in mMTC scenarios is presented in [38]. By synchronizing predefined RIS configurations within a time division multiple access (TDMA) frame, the proposed scheme presented an increase in the overall throughput for higher channel loading at the cost of a high training overhead. The same protocol was studied in [28], where a novel power consumption model was designed, and the protocol EE has been analyzed, in addition to new access policies and rules. Low power consumption could be achieved on the side of the machine-type device, making the protocol suitable for sustainable IoT networks.

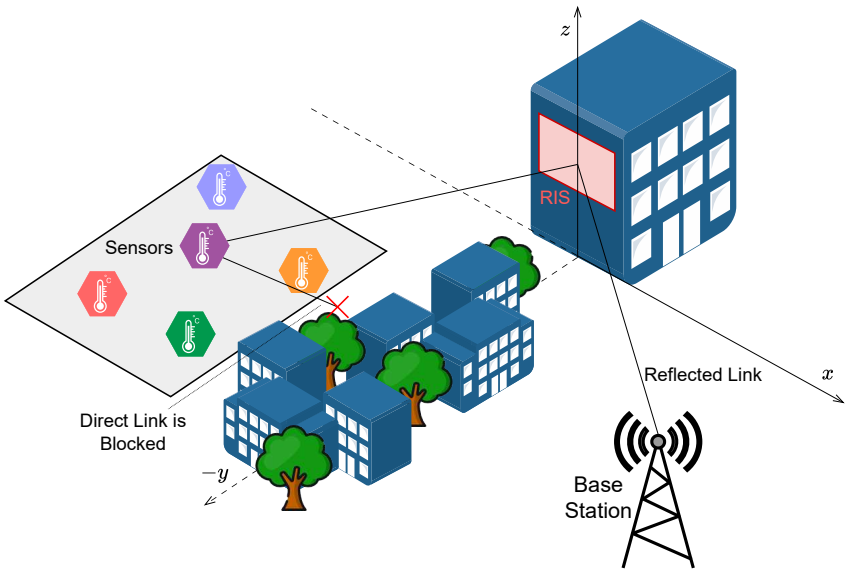

Figure 1 – Urban scenario equipped with a RIS. The direct links between sensors (MTDs) and the BS are blocked by building, trees and other obstacles. To deal with this problem, a RIS is deployed at the top of a building, allowing the communication through a reflected link.

However, RIS can also be applied in multi-application scenarios, where devices with distinct use cases coexist. In [39], RIS technology is applied to enable the coexistence of two types of UEs in the same network: a URLLC UE and an eMBB UE. After a training step, the RIS sets two predefined configurations, one for each UE. Then, it applies the URLLC-oriented one and monitors a request from the eMBB UE. When this request is identified, the RIS switches to the eMBB-oriented configuration until its transmission is made, then returns to the URLLC-oriented pattern. Hence, in that case, the RIS is not only used to increase the system coverage and mitigate interference among UEs but also allows the coexistence of URLLC and eMBB devices.

It is also worth noticing that a key challenge involving RIS-aided scenarios is its practical implementation, especially in panels with a high amount of reflective elements. Proposed solutions must be effective not only w.r.t. its achievable EE, SE, and supported number of users; but the *feasibility* of these algorithms also have to be carefully addressed: proposed methods must reach a solution *as fast as possible* to fit the whole optimization process within a channel coherence block to convince that RIS is indeed a candidate solution for B5G. Therefore, methods such as those explored in [40] and [28], which do not require unique RIS phase-shift design within each coherence block, arise as promising alternatives for B5G mMTC scenarios, although more realistic scenarios, that explore different MTDs deployments and includes more channel effects in the adopted channel model still have to be addressed. This Dissertation extends the discussion regarding this RIS-aided RA protocol, analyzing its performance under novel channel models and adapting it to support MTDs with different channel conditions, considering the EE and throughput of these novel approaches.

3.1 Far-Field *vs.* Near-Field

Across this investigation, we have formulated the problem and searched for new random access protocols; the system, channel, and reception model assumed a planar wavefront, *i.e.*, far-field propagation scenarios. In the situation where the received signals were under the condition of spherical wavefront propagation (near-field), implications for the problem formulation and possible solutions are briefly discussed in the sequel.

The transition from a planar wavefront (far-field) to a spherical wavefront (near-field) would necessitate significant changes in the modeling, design, and implementation of random access protocols, requiring a comprehensive understanding of the new propagation dynamics and their implications for wireless communication systems.

If the received signals were under the condition of spherical wavefront propagation (near-field), several implications would arise for the problem formulation and possible solutions:

1. *Channel Modeling Complexity*: The channel models would need to account for the effects of near-field propagation, which includes variations in signal strength and phase across each antenna from the antenna array due to the spherical wavefront. This would require more complex mathematical formulations to accurately represent the channel characteristics, including the distance-dependent path loss and the phase shifts that occur as the wavefront propagates.

2. *Antenna Array Design*: The design of the antenna arrays would need to consider the spatial distribution of the antennas with the near-field region. This could involve optimizing the placement and configuration of antennas to ensure adequate signal reception and transmission, as the array's performance could be significantly affected by the proximity of the devices.

3. *Signal Processing Techniques*: Signal processing algorithms would need to be adapted to handle the characteristics of near-field signals. This may include the development of new algorithms for channel estimation, beamforming, and interference cancellation that consider the spherical wavefront effects, which can differ from those used in far-field scenarios.

4. *Increased Interference Management*: In near-field scenarios, the likelihood of interference from other devices may increase due to the proximity of multiple users. Random access protocols must incorporate mechanisms for managing interference more effectively, possibly through advanced scheduling or resource allocation strategies considering device spatial distribution.

5. *Localization and Tracking*: The ability to localize and track devices may be enhanced in near-field conditions, as the spherical wavefront can provide more detailed information about the position of devices. This could lead to developing protocols that leverage precise localization information to optimize access and resource allocation.

6. *Protocol Adaptation*: Existing random access protocols must be re-evaluated and adapted to work effectively in near-field conditions. This could involve modifying access policies to account for the different propagation characteristics and interference patterns, ensuring the protocols remain efficient and reliable.

7. *Performance Metrics Reevaluation*: The performance metrics used to evaluate the protocols may also need to be adjusted to reflect the unique challenges and characteristics of near-field propagation. Metrics that account for the spatial diversity and the impact of near-field effects on signal quality and reliability would be essential.

4 SYSTEM MODEL

The adopted scenario, shown in Fig. 2, consists of a single antenna BS located in the fourth quadrant and K mobile terminal devices (MTDs) uniformly distributed in the shaded area of the first and fourth quadrants. Specifically, the BS is placed at the distance d_{BS} from the origin and angle $\theta_{\text{BS}} \in [0, \pi/2]$. The k-th MTD is positioned at the distance $d_k \in [d_{\min}, d_{\max}]$ from the origin and angle $\theta_k \in [-\pi/2, \pi/2]$. Moreover, let d_k^d denote the distance from the BS to the k-th MTD. Between the first and fourth quadrants, *i.e.,* along the positive y-axis, the propagation of wireless signals is partially harmed due to a blockage. Because of that, in terms of received power, one can say that MTDs located in the fourth quadrant present better signal quality when compared to users positioned in the first one. In Fig. 2, we distinguish these two specific cell areas using green and red colors.

An RIS with N elements is installed along the xz-axis, centered at the origin, to combat the signal attenuation due to the blockage. We assume that N_x and N_z are the number of elements along the x and z-axes, respectively, resulting in $N = N_x N_z$. Precisely, each element of the RIS reflects the impinging electromagnetic waves, impressing an independent controllable phase shift to them. Hence, the RIS establishes a virtual line-of-sight (LoS) path between the MTDs in the red area and the BS, enhancing their channel quality. As in [28], we assume that the RIS has a set $\Theta \in \{\theta_1, \ldots, \theta_C\}$ of predefined configurations, such that the cardinality is $|\Theta| = C$. By choosing the c-th configuration accordingly, all the RIS elements impress a phase shift equal to θ_c. Similarly to [28], we define the elements of Θ by

$$\theta_c = \frac{\pi(c-1)}{2(C-1)}, \ \forall c = 1, \ldots, C. \tag{4.1}$$

Therefore, the potential phase shift values are C uniformly-spaced angles within the interval $[0, \pi/2]$. The RIS switches its phase configurations during the S time slots of the adopted TDMA frame, *e.g.,* using one configuration per time slot. Because of that, one can say that the channel state during the frame depends on the current time slot, s.

The channel of the k-th MTD during the time slot s is modeled as

$$h_k[s, \theta_k] = h_k^d[s, \theta_k] + h_k^r[s], \tag{4.2}$$

where $h_k^d[s, \theta_k]$ and $h_k^r[s]$ are the channel coefficients of the direct and reflected links between user k and the BS, respectively, and "$[s]$" is used to explicitly show the dependency of the channel coefficients and the time slot s. In this work, different from [28], we model the propagation environment as a Rice channel. The direct link channel coefficient,

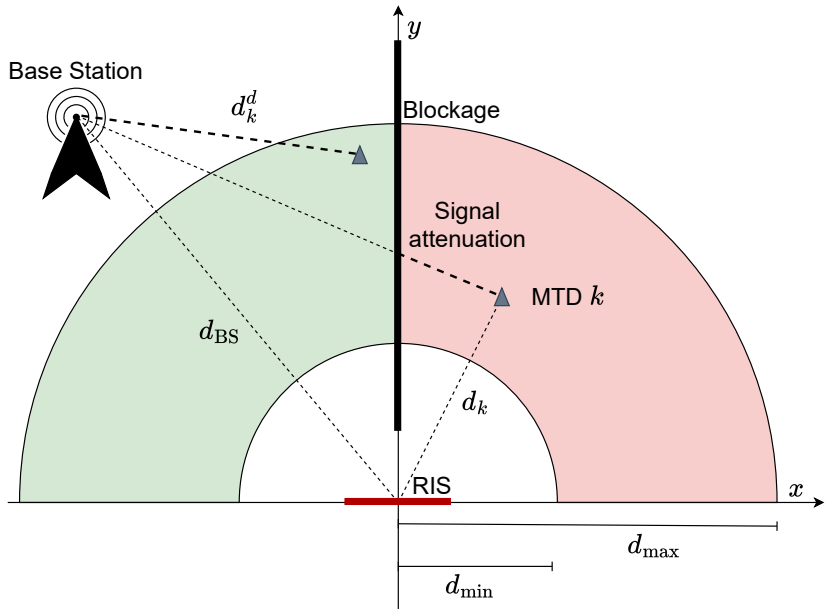

Figure 2 – Adopted scenario: MTDs in the red area (first quadrant) have their direct radio links to the BS blocked. On the other hand; for the MTDs in the green area (fourth quadrant), the direct radio links are present due to the absence of obstacles between them and the BS. The proposed protocol can handle both kinds of MTDs.

$h_k^d[s, \theta_k]$, can be calculated by:

$$h_k^d[s, \theta_k] = \sqrt{\beta_k^d(\theta_k)} \left(\sqrt{\frac{\kappa(\theta_k)}{1+\kappa(\theta_k)}} \overline{h}_k^d + \sqrt{\frac{1}{1+\kappa(\theta_k)}} \tilde{h}_k^d[s] \right) \tag{4.3}$$

where $\overline{h}_k^d$ is the line-of-sight (LoS) component of the channel, which can be modeled as

$$\overline{h}_k^d = e^{j\psi_k^d}, \tag{4.4}$$

with $\psi_k^d = \omega d_k^d$ being the total phase shift, $\omega = 2\pi/\lambda$, where λ is the carrier wavelength, and $\tilde{h}_k^d[s]$ is the non-line-of-sight (nLoS) component, that models the multipath propagation effects. We model $\tilde{h}_k^d[s]$ as a circular symmetric random variable, *i.e.,* $\tilde{h}_k^d[s] \sim \mathcal{CN}(0, 1)$.

Furthermore, $\beta_k^d(\theta_k)$ and $\kappa(\theta_k)$ are step-like functions that establishes the path loss coefficient and the Rice factor of the k-th MTD direct link, respectively. Notice that $\beta_k^d(\theta_k)$ and $\kappa(\theta_k)$ can be viewed as functions of θ_k due to the presence of the blockage in the adopted environment, which affects differently MTDs located in the red or green areas of the cell. For instance, suppose an MTD positioned at the green area, which results in $\theta_k \in \left[-\frac{\pi}{2}, 0\right]$. The direct link between this MTD and the BS does not suffer any attenuation due to the blockage, then resulting in a higher $\beta_k^d(\theta_k)$ and, due to the absence of obstacles, one can admit that this MTD's channel is predominantly a line-of-sight (LoS)

channel, which can be modeled by considering high Rice factors values in equation (4.3). On the other hand, if an MTD is located at the red side, the blockage severely affects the direct link between this MTD and the BS, attenuating it and also contributing with an enhance in multipath propagation effects, resulting in a channel coefficient with small gain and predominantly non-Line-of-Sight (nLoS). Then, it is convenient to model this channels considering lower values for their path losses and Rice factors. Denoting (ξ_1, κ_1) and (ξ_2, κ_2) as tuples representing the blockage attenuation and Rice factors to be adopted for the h_k^d modeling for users at the green and red areas of the communication cell, respectively, one can define $\beta_k^d(\theta_k)$ and $\kappa(\theta_k)$ as:

$$\beta_k^d(\theta_k) = \left[(\xi_1 - \xi_2)\, u(-\theta_k) + \xi_2\right] \cdot \alpha_{\text{BS}} \alpha_k \left(\frac{\lambda}{4\pi d_k^d}\right)^2; \tag{4.5}$$

$$\kappa(\theta_k) = (\kappa_1 - \kappa_2)\, u(-\theta_k) + \kappa_2, \quad \forall\ \theta_k \in \left[-\frac{\pi}{2}, \frac{\pi}{2}\right], \tag{4.6}$$

where $u(\cdot)$ is the unit step function. Furthermore, notice in equation (4.3) that $\overline{h}_k^d$ does not depend on s, and stays constant during the whole TDMA frame. However, we assume that the small scale fading component changes at every time slot due to small changes in the environment, specially the RIS phase shifts. Hence, we write the nLoS component of the direct link as $\tilde{h}_k^d[s]$.

Similarly, we model the reflected link of MTD k at time slot s as

$$h_k^r[s] = \sqrt{\beta_k^r}\left(\sqrt{\frac{\delta}{1+\delta}}\overline{h}_k^r[s] + \sqrt{\frac{1}{1+\delta}}\tilde{h}_k^r[r]\right), \tag{4.7}$$

where δ and β_k^r are the reflected link Rice factor and path loss term, respectively; $\overline{h}_k^r[s]$ and $\tilde{h}_k^r[s]$ are the LoS and nLoS coefficient of the reflected link at the s-th RIS configuration, respectively. The nLoS coefficients can also be obtained statistically, $\tilde{h}_k^r[s] \sim \mathcal{CN}(0,1)$, and the LoS are calculated according to equation (4.8):

$$h_k^r[s] = e^{j\psi_k^r}\Omega_k[s], \tag{4.8}$$

with ψ_k^r being the total phase shift of the reflected link and $\Omega_k[s]$ the array factor of the RIS during the time slot s for the MTD k, which can be obtained respectively as follows:

$$\psi_k^r = \omega\left[d_{\text{BS}} + d_k - (\sin\theta_{\text{BS}} - \sin\theta_k)\,\frac{N_x+1}{2}d_x\right], \tag{4.9}$$

$$\Omega_k[s] = N_z \sum_{n=1}^{N_x} e^{j\omega(\sin\theta_k - \sin\theta_s)nd_x}. \tag{4.10}$$

Finally, the path loss coefficient calculation of the reflected link is made according to equation (4.11):

$$\beta_k^r = \alpha_{\text{BS}}\alpha_k \left(\frac{d_x d_z}{4\pi d_{\text{BS}} d_k}\right)^2 \cos^2\theta_k. \tag{4.11}$$

The proof of equation (4.11) can be viewed in [38, 41]

The definition of parameters ξ_1, ξ_2, κ_1 κ_2 and δ provides flexibility to the channel model. For instance, parameters ξ_1 and ξ_2 allow control of the default channel gains at both cell sides. Clearly, it is suitable to consider $\xi_1 > \xi_2$ because the blockage's presence severely attenuates the channel gains of MTDs that are behind it, whose default channel gain is defined by ξ_2. In addition, depending on the electromagnetic properties of the material that the blockage is made, the signal attenuation can change. Hence, ξ_1 and ξ_2 can be carefully established after a real scenario study. Furthermore, parameters κ_1, κ_2 and δ are essential to define the LoS/nLoS percentages of each channel link: a purely nLoS channel can be considered by adopting $\kappa_1 = \kappa_2 = \delta = 0$; while the pure LoS channel adopted in [42] can be reproduced by making $\kappa_1 = \kappa_2 = \delta \to \infty$. Intermediate values result in Rician fading channels where each link can be individually adjusted according to the physical properties of the environment, such as the presence of scatterers. In the adopted configuration, it is suitable to consider $\kappa_1 > \delta > \kappa_2$.

4.1 Studied Random Access Protocols

In this subsection, we present in detail both RIS-aided RA protocols studied in this Master's Dissertation. Before introducing them, we need to explain the RIS operation, why it is deployed in the environment and how it can help the studied protocols. Then, we show the four access rules, denoted *access policies* that are available to MTDs to perform the data uplink. Finally, we highlight the details of each RA protocol.

4.1.1 RIS Integration With the TDMA Frame

The proposed protocol requires a two-stage time-division multiple access (TDMA) frame, as represented in Fig. 3[1]. The training and access phases are depicted in green and orange, respectively. Notice that the training phase has S effective *training slots*, each with duration T_{ts}, and an additional slot shown in purple, denoted σ-slot, which has duration T_σ and is not always required. The σ-slot is designed because some access policies and/or RA protocols obligate MTDs to perform some operations before performing the uplink of data packets. Then, we consider that these operations are all made during the σ-slot, when needed. Besides, the second stage is reserved for UL access and has a total duration of T_a, with J time slots of duration T_{as} each. While designing the TDMA frame, it must be guaranteed that the whole frame fits inside a channel coherence time, *i.e.*, $T_f \leq (\Delta T)_c$, to guarantee that the RA protocols perform correctly.

[1] In some specific cases, the combination of the adopted access policy with an RA protocol makes the training stage unnecessary. We will return to this discussion soon, when the access policies and the RA protocols have been presented.

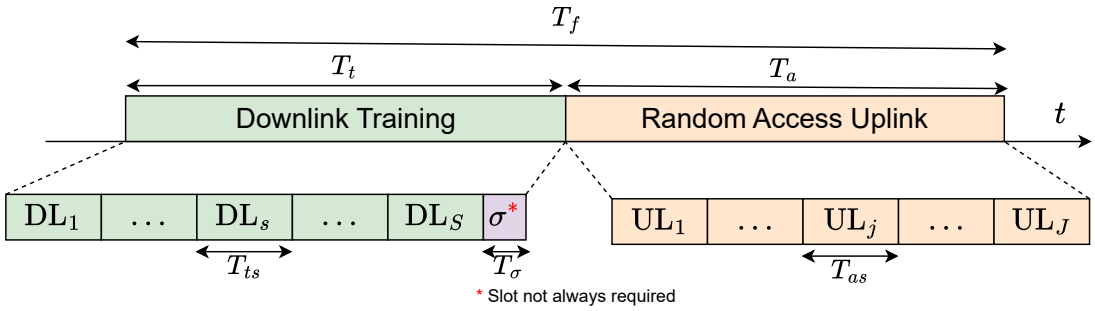

Figure 3 – TDMA frame adopted by the RA protocols, composed by a downlink training phase (shown in green) and a random access uplink phase, shown in orange. The training phase has S training slots of duration T_{ts} and an extra purple slot, denoted σ-slot, which is not always required and has duration T_σ. On the other hand, the access phase includes J access slots (depicted in orange), that lasts T_{as} seconds each.

Throughout this Dissertation, for simplicity, we assume that the numbers of effective training slots and access slots are equal to the number of predefined RIS configurations, *i.e.*, $S = J = C$.[2] Hence, in the remainder of the paper, we interchangeably denote these three parameters by S. During the S training time slots, the RIS uses all of the C predefined configurations from $\boldsymbol{\Theta}$ sequentially, one per slot, allowing users to estimate a collection of S SNRs, also referred to as *channel qualities*. Notice that each obtained value is associated with a unique RIS phase-shift configuration. Then, in the UL phase, the same RIS pattern used during training is repeated in the S time slots of the access phase, allowing users to explore the diversity of the observed channel to perform the UL. Combined with suitable access policies, this procedure has demonstrated good performance in recent studies [28, 40]. Four access policies, classified as single access and double access policies, are studied with the adopted RA protocols, and each has its own working rules, performance, and complexity, which are summarized in subsection 4.1.4.

4.1.2 Single Access Policy RIS-Aided Random Access Protocol (SAP-RARAP)

In SAP-RARAP, all MTDs use the same access policy to perform data uplink in all possible scenario context of Fig. 2, which can be IRSAP, CRDSAP, s-SCP or CARP. In this RA setup, if the access policy adopted do not uses CSI, the training phase is unnecessary, as long as all data uplink will be performed randomly by MTDs. Hence, for IRSAP and CRDSAP, the whole TDMA frame has only S access slots with duration T_{as}. In that cases, the RIS shifts throughout all C predefined configurations once during

[2] The access phase does not necessarily need to have the same number of time slots as the training phase. A generic protocol could consider an access phase with $m \cdot C$ time slots, where m is a positive integer. Accordingly, the RIS could repeat each configuration m times during the access phase, allowing the MTDs to exploit the channel condition induced by a single RIS beam configuration in multiple time slots rather than a single one. However, repeating the RIS pattern several times during the access phase can make the duration of TDMA frame longer than the channel coherence time, which would make the RA unfeasible.

the TDMA frame, changing the channel conditions at each access slot. On the other hand, when s-SCP or CARP is used, the training step must be performed in order to allow MTDs to estimate theirs SNRs and properly perform the data uplink. In these conditions, the RIS uses the phase-shifts configurations from $\boldsymbol{\Theta}$ twice during the TDMA frame, one during the training phase and one during the access phase. Furthermore, due to the training step, the duration of the TDMA frame is increased by $ST_{tr} + T_\sigma$ seconds, resulting in a total frame duration of $S(T_{ts} + T_{as}) + T_\sigma$. A summary of the main SAP-RARAP implementations (four variants of SAP access policy) parameters is presented in Table 1. Both phases of the TDMA frame are described in the following subsections.

Parameter	**Adopted Access Policy**			
	IRSAP	**CRDSAP**	**s-SCP**	**CARP**
Training/CSI	No	No	Yes	Yes
σ-Slot	No	No	Yes	Yes
n_k	$n_k \in [2, S]$	$n_k = 2$	$n_k = s$	$n_k \in [1, S]$
T_f	ST_{as}	ST_{as}	$S(T_{as} + T_{ts}) + T_\sigma$	$S(T_{as} + T_{ts}) + T_\sigma$

Table 1 – Main specifications of the four SAP-RARAP implementations (variants) parameters with every access policy. A visual representation of the frame duration is depicted in Figure 3.

4.1.2.1 SAP-RARAP Phase I: Downlink Training

Denote the BS transmit power as $\rho_{\text{BS}} > 0$ and the total pilot length in one time slot as τ. Furthermore, the zero-mean pilot signal is $\boldsymbol{\phi} \in \mathbb{C}^\tau$, and the receiver noise is called $\mathbf{n}_k[s] \sim \mathcal{CN}(0, \sigma^2_{\text{MTD}}\mathbf{I})$. It is assumed that $\mathbb{E}\{\|\boldsymbol{\phi}\|^2\} = \tau$. Hence, the signal received by the MTD k during the time slot s of the DL training phase, Figure 3, is

$$\mathbf{y}^{\text{tr}}_k[s] = \sqrt{\rho_{\text{BS}}} h_k[s]\boldsymbol{\phi} + \mathbf{n}_k[s]. \tag{4.12}$$

From this signal, the MTD estimates its channel coefficient adopting the minimum-variance unbiased estimator [40]

$$\hat{h}_k[s] = \frac{1}{\tau\sqrt{\rho_{\text{BS}}}} \boldsymbol{\phi}^{\text{T}} \mathbf{y}^{\text{tr}}_k[s]. \tag{4.13}$$

Notice that, after estimating the channel coefficient in each time slot, the MTD will have a collection of S estimates. In SAP-RARAP protocol, such an information is exploited by access policies that requires CSI to aid the selection of the time slots used to transmit the packet replicas. This slot selection is based on the channel qualities $q_k[s],\ \forall s = 1, \ldots, S$, which can be obtained as follows:

$$q_k[s] = \|\hat{h}_k[s]\|^2. \tag{4.14}$$

Furthermore, in Figure 3 we notice that the DL training phase contains a special time slot, named σ-slot. During this slot, MTDs decide at which RA access slot it will send the packet replicas. Besides, notice that the computation of equations (4.12), (4.13) and (4.14) are not required when an access policy that perform the data uplink randomly is adopted. In that cases, as already discussed, the TDMA frame can be even reduced, neglecting the whole downlink training phase. Hence, one can say that only the Phase II is performed.

4.1.2.2 SAP-RARAP Phase II: Random Access Uplink

In the UL access phase, each MTD transmits replicas of τ_{d} data symbols during the selected time slots. Specifically in the time slot s, the UL received signal $\mathbf{y}[s] \in \mathbb{C}^{\tau_{\mathrm{d}}}$ at the BS is defined as:

$$\mathbf{y}[s] = \sum_{k \in \mathcal{K}_s} \sqrt{\rho_{\mathrm{MTD}}} h_k[s] \mathbf{x}_k + \mathbf{n}[s], \tag{4.15}$$

where $\mathcal{K}_s$ is the set containing the indices of the MTDs that decided to transmit during the time slot s, $\mathbf{x}_k \in \mathbb{C}^{\tau_{\mathrm{d}}}$ are the data symbols, and $\mathbf{n}[s] \sim \mathcal{CN}(\mathbf{0}, \sigma^2_{\mathrm{BS}}\mathbf{I})$ is the AWGN noise at the BS receiver. According to the selected RA policy, an MTD can send single or multiple replicas of its data throughout the S time slots.

After reception, the BS applies a *Successive Interference Cancellation* (SIC) algorithm in $\mathbf{y}$ to decode the received packets. The algorithm first searches for time slots where a *singleton*, which is characterized by an interference-free time slot, where a single MTD has transmitted, occurred, and then decodes its packet. Next, the acquired information is used to reconstruct and subtract the decoded signal from time slots where it was re-transmitted, eventually creating new singletons. This process is usually handled in practical scenarios by sending pointers to all packet replicas with every packet. Then, interference can be canceled from these time slots. The process continues recursively until no more packets can be successfully decoded. This can happen when a collision cannot be resolved or when a singleton occurs with a received SNR under the SIC decoder threshold.

4.1.3 The Double Access Policy RIS-Aided Random Access Protocol (DAP-RARAP)

Differently from SAP-RARAP, in DAP-RARAP MTDs must decide which access policy to use during uplink. In short, this can be performed in a completely decentralized fashion, leveraging the training time of the TDMA frame to perform not only the estimation of the channel qualities, but also to estimate at which cell region each MTD is located. The details about this protocol are presented in the following.

The DAP-RARAP is completely designed for the scenario depicted in Figure 2, and aims to induce MTDs with different channel conditions to select proper access policies

to perform the data uplink. This method obligates the training phase to be performed, regardless of the adopted access policies, resulting in a total frame time T_f equals to

$$T_f = S\left[T_{ts} + T_{as}\right] + T_{\sigma}. \tag{4.16}$$

In order to perform DAP-RARAP, one must establish a *set of available policies*, denoted by $\mathcal{A}$, a *set of MTDs uplink power levels*, $\mathcal{P}$, and a *localization threshold* parameter, denoted by σ^2_{TH}.

We assume $\mathcal{A} = \{A_1, A_2\}$, where each element of set $\mathcal{A}$ refers to an access policy. It is required that, if A_1 uses CSI, A_2 must not be aided by any CSI and vice-versa. From now on, we will consider that policy A_1 uses CSI, which implies that A_2 does not. The goal of DAP-RARAP is to let each MTD decides which policy to use after performing the DL training phase. In short, this can be made by letting MTDs compute a *localization coefficient*, denoted by σ^2_k, and comparing it with the pre-established localization threshold σ^2_{TH}. Based on the selected policy, MTDs can also adjust their uplink power, selecting one of two available sub levels from $\mathcal{P}$. We explain this process in detail in the following subsections. Specifically, equation (4.18) in subsection 4.1.3.1 explains the computation process of the localization coefficient σ^2_k by MTDs, and the optimal definition of the localization threshold parameter σ^2_{TH} is explained in subsection 5.5.1.1. In addition, we have to emphasize that the computation of σ^2_{TH} is sensitive to several system parameters, *i.e.,* σ^2_{TH} must be adapted according to the scenario configuration, such as the number of RIS elements, number of available time slots and the blockage attenuation. In Section 5.5 we present a discussion regarding the variation of σ^2_{TH} with these system parameters.

4.1.3.1 DAP-RARAP Phase I: Downlink Training

The DL training of the DAP-RARAP protocol is essentially the same of the SAP-RARAP, described in subsection 4.1.2.1. Regardless of the adopted combination of access policies $\mathcal{A}$, the BS perform the broadcast of data pilots as described by equation (4.12), and MTDs estimates their channel coefficients and channel qualities at each slot the same way as described in equations (4.13) and (4.14). With the estimated channel qualities, in DAP-RARAP, during the σ-slot, MTDs also computes the *normalized channel qualities*, $z_k[s]$:

$$z_k[s] = \frac{q_k[s]}{S^{-1}\sum_{s'=1}^{S} q_k[s']}. \tag{4.17}$$

Then, it obtains the sample variance of the normalized estimates $z_k[s]$, *i.e.*,

$$\sigma^2_k = (S-1)^{-1}\sum_{s=1}^{S}\left(z_k[s] - S^{-1}\sum_{s'=1}^{S} z_k[s']\right)^2. \tag{4.18}$$

Notice that for MTDs located at the red area of the communication cell, Figure 2, the RIS phase shifts panel exerts a crucial impact throughout the S training slots. More

precisely, the measured channel quality of these MTDs tends to be higher at specific time slots, which corresponds to slots where the predefined RIS configuration covers the angular positions where these MTD are positioned. Hence, when MTDs at the red area computed equation (4.18) using its collection of S measured channel qualities, higher values of σ_k^2 should be obtained. On the other hand, for MTDs positioned at the green side of the cell experiences a much more constant channel quality among the S training slots. This happens because the direct link of these MTDs is not attenuated by the blockage, resulting in a LoS link between them and the BS. Hence, the RIS link becomes negligible when compared to the direct one, resulting in *almost constant* values of channel qualities during the S training slots, implying in lower values of σ_k^2.

By establishing an optimal σ_{TH}^2, MTDs can compare σ_k^2 with σ_{TH}^2, and them select a policy from $\mathcal{A}$ to perform the uplink of its data packets. If the calculated σ_k^2 is large, it means that the RIS configuration exerts a substantial impact on the MTD channel coefficient. Therefore, such an MTD is a good candidate for RIS assistance. In contrast, RIS does not significantly affect the communication performance and reliability of MTDs whose σ_k^2 is lower than σ_{TH}^2, so they do not need RIS assistance. Hence, an MTD decides whether it benefits from RIS assistance by comparing σ_k^2 with a pre-established threshold $\tilde{\sigma}_{\text{TH}}^2 \geq 0$. This threshold must be optimized according to the channel/cell configuration, the MTD's spatial density, the number of RIS elements and the number of available time slots S. Hence, after comparing σ_k^2 with σ_{TH}^2, if $\sigma_k^2 \geq \sigma_{\text{TH}}^2$ the k-th MTD decides to use policy $A_1 \in \mathcal{A}$; otherwise, $A_2 \in \mathcal{A}$ if it obtains $\sigma_k^2 < \sigma_{\text{TH}}^2$. Notice that in DAP-RARAP, even if an MTD decides to use policy A_2 to perform uplink, which is the policy that do not require CSI, this MTD needs to perform the estimation of its channel qualities anyway, as long as those estimates are used in the computation of σ_{TH}^2, which allows the policy selection.

In addition, it is worth noticing that as long as MTDs are able to estimate at which cell region they are located, we can also allow them to adjust their transmission power, letting MTDs from the green area reduce the adopted transmit energy, saving their batteries. However, MTDs from the red area can transmit at a higher power level due to its higher distance to the BS and the signal attenuation suffered by their direct links caused by blockage. Because of that, we define the set of available uplink powers as $\mathcal{P} = \{\rho_{\text{L}}, \rho_{\text{H}}\}$ which contains two available uplink powers, a low and a high power levels. Ideally, MTDs from the green area have to use the lower power level, ρ_{L}, while MTDs from the red area are induced to use the higher power level, denoted by ρ_{H}. This approach can significantly reduce the average power consumption of MTDs, hence extending the useful life of their batteries, which is essential in mMTC scenarios.

The selection of the power level is made the same way as the selection of the access policy. With the estimated σ_k^2, a comparison is made with σ_{TH}^2, and if an MTD obtains

$\sigma_k^2 \geq \sigma_{\text{TH}}^2$ it infers its localization in the red area, and then selects ρ_{H} as its uplink power. The lower power level ρ_{L} is picked by this MTD if $\sigma_k^2 < \sigma_{\text{TH}}^2$. In summary, the decision rules taken by MTDs leads to two transmission 'schemes':

i) MTD k transmit its packets with power $\rho_{\text{H}} \in \mathcal{P}$ following policy $A_1 \in \mathcal{A}$ rules; or

ii) MTD k perform the uplink with power $\rho_{\text{L}} \in \mathcal{P}$ following policy $A_2 \in \mathcal{A}$ rules.

A summary of the main DAP-RARAP implementations (four variants of DAP access policies) parameters can be viewed in Table 2. We recall that, for DAP-RARAP, the total frame time T_f is always obtained by equation (4.16), with $T_{as} > T_{ts} \geq T_\sigma \neq 0$, regardless of the combination of access policies adopted, and the amount of sent replicas, n_k, is showed for both available policies, A_1 and A_2 respectively.

Parameter	**Adopted Access Policies**				
	A_1	**CARP**	**CARP**	s-**SCP**	s-**SCP**
	A_2	**IRSAP**	**CRDSAP**	**IRSAP**	**CRDSAP**
Training/CSI		Yes	Yes	Yes	Yes
σ-Slot		Yes	Yes	Yes	Yes
n_k		$n_k \in [1, S]$ or $n_k \in [2, S]$	$n_k \in [1, S]$ or $n_k = 2$	$n_k = s$ or $n_k \in [2, S]$	$n_k = s$ or $n_k = 2$

Table 2 – Main specifications of the four DAP-RARAP implementations (variants) with every combination of access policies studied. A visual representation of the frame duration is depicted in Figure 3.

4.1.4 Available Uplink Rules - The Access Policies

To thoroughly develop the analysis of this Dissertation, the access policies presented in [28] can be applied. Two of them can be performed without any channel knowledge, *i.e.*, the access time slots selected for uplink are randomly picked, and the use of CSI information does not affect the MTDs decision of sending a packet in a given slot. Hence, CSI information is not needed, which makes the downlink training phase unnecessary. On the other hand, the remaining two policies require CSI to work properly.

The access policies adopted throughout this work are:

i) Irregular Repetition Slotted ALOHA Policy (IRSAP);

ii) Contention Resolution Diversity Slotted ALOHA Policy (CRDSAP);

iii) s-Strongest Configurations Policy (s-SCP); and

iv) Configuration-Aware Random Access Policy (CARP),

which are explained in detail in the following. A representation of how each one of these policies performs its respective RA UL is depicted in Figure 4.

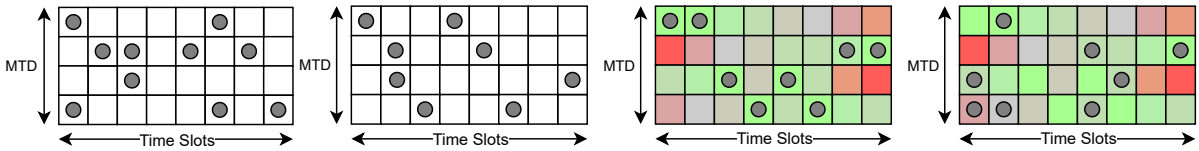

(a) IRSAP (b) CRDSAP (c) s-SCP (d) CARP

Figure 4 – Graphical representation of the RA UL phases in each access policy studied. Greyscale slots in Figures (4a and 4b) indicate such a policies do not require CSI, while colored ones (4c and 4d) do. The redder the time slot, the lower measured SNR, while greener slots represent higher SNRs values.

IRSAP: This access policy is depicted in Figure 4a, and is the first policy that does not require CSI to perform. The number of replicas that each MTD will send is picked up randomly following the probability density function (PDF) [43]:

$$\Lambda(x) = \left(1 + \frac{1}{S-1}\right) \sum_{s=2}^{S} \frac{x^s}{(s-1)\cdot s}. \tag{4.19}$$

Hence, MTD k can transmit $s_k \in [2, S]$ replicas. The slots where each replica will be sent are uniformly selected.

CRDSAP: Figure 4b shows the UL phase performed by this policy, which also does not need CSI. This policy is an adaptation of the CRDSA protocol proposed in [44]. Differently from IRSAP, CRDSAP fixes the number of transmitted replicas, resulting in only 2 data packets sent by each MTD along the entire frame composed by S time slots, *i.e.*, $s_k = 2\ \forall k$, and the slots where these replicas are sent are also randomly selected, following a uniform distribution.

s-SCP: This access policy is represented in Figure 4c, and is the first policy that takes CSI into account, aiding the selection of time slots to perform the data UL. Therefore, the training step must be performed when s-SCP is adopted, allowing each MTD to transmit its replicas in the s slots where the measured channel qualities are higher, which are depicted in Figure 4 by greener shades. Notice that the selection of the s best slots is only possible because the same RIS phase shift configuration pattern used in the training phase is repeated during the access phase, allowing MTDs be to re-exposed to a channel quality measured during the training phase. Throughout this work, we adopt $s = 2$.

CARP: The last access policy also takes CSI into account and is depicted in Figure 4d. In this access policy, the probability $p_k[s]$ of an MTD transmit a replica of its data packed during slot s is directly proportional to the channel quality in this slot, $q_k[s]$:

$$p_k[s] = \frac{q_k[s]}{\sum_{s'=1}^{S} q_k[s']}. \tag{4.20}$$

Hence, the number of replicas transmitted by each MTD is not fixed, resulting in a number of replicas $s_k \in [1, S]$. Notice that, in CARP, the time-slot selection rule can result in cases where MTDs stay silent in all slots, and to avoid this, we guarantee that if any time slot is selected by an MTD, it sends a single replica in the slot with higher channel quality.

4.2 Power Consumption Model

In this section, the power consumption models are described for both RA protocols approaches. We start with DAP-RARAP because its power consumption model can be easily associated with the TDMA frame shown in Figure 3. Then, we discuss the SAP-RARAP power consumption model, which is basically a simplification of DAP-RARAP's power consumption model.

4.2.1 DAP-RARAP Power Consumption Model

We define the transmission powers of BS and MTDs as a function of its consumed *energies* and duration of each TDMA frame. Let ρ_{BS} and $\rho_{\text{MTD},k} \in \mathcal{P}$ be the downlink transmission power of the BS and the uplink transmission power of MTD k, respectively. As long as the BS performs the downlink of the data pilots during the training slots, which is of duration T_{ts}, and the MTDs uplink each data packet during an access slot of duration T_{as}, the transmit energies of the BS and the MTDs can be written, respectively, as:

$$E_{\text{BS}}^{\text{DL}} = \rho_{\text{BS}} T_{ts} \qquad \text{and} \qquad E_{\text{MTD},k}^{\text{UL}} = \rho_{\text{MTD},k} T_{as}, \tag{4.21}$$

Furthermore, the BS, RIS and MTDs expend some power with other functions rather than downlink and uplink transmissions. For that case, we define the powers consumed based on its respective *power consumption rates*, which are defined in [W/s]. We assume that the BS consumes $\dot{P}_{\text{BS}}$ watts per second to perform crucial backhaul operations, signal processing, and cooling per unit of time. Similarly, each MTD consumes $\dot{P}_{\text{MTD}}$ watts per second to perform synchronization, signal processing, estimation of channel qualities, and to apply the decision rule of the adopted access policy. Finally, each RIS element requires $\dot{P}_n$ watts per second to execute the phase shifts during the TDMA frame. Stated that one can calculate the total power consumption of the DAP-RARAP protocol during a TDMA frame, as follows.

BS power consumption: We denote the average power consumed per frame transmitted

by the BS during a TDMA frame by P_{BS}, and is calculated as:[3]

$$\begin{aligned} P_{\text{BS}} &= S\mu_{\text{BS}}\frac{E^{\text{DL}}_{\text{BS}}}{T_{ts}} + \dot{P}_{\text{BS}}T_f \qquad [\text{W}] \\ &= S\mu_{\text{BS}}\frac{E^{\text{DL}}_{\text{BS}}}{T_{ts}} + \dot{P}_{\text{BS}} \cdot [S(T_{ts}+T_{as})+T_\sigma] \qquad [\text{W}]; \\ &= S\mu_{\text{BS}}\rho_{\text{BS}} + \dot{P}_{\text{BS}} \cdot [S(T_{ts}+T_{as})+T_\sigma] \qquad [\text{W}] \end{aligned} \tag{4.22}$$

where the first term of the sum computes the power used for the pilots downlink during training; last term refers to backhaul operations, and T_f is the total frame time.

RIS power consumption: Similarly, power consumption of the RIS can be obtained by multiplying the power consumed by a single reflective element by N. Hence, we have

$$P_{\text{RIS}} = N\dot{P}_n T_f \ [\text{W}] = N\dot{P}_n \cdot [S(T_{ts}+T_{as})+T_\sigma] \ [\text{W}]. \tag{4.23}$$

MTD's power consumption: Finally, for the MTDs, we have that the amount of average power consumed by each device is calculated according to equation (4.24). The number of replicas sent by MTD k is denoted by n_k and the RF amplifier inefficiency of MTDs is μ_{MTD}.

$$\begin{aligned} P_{\text{MTD},k} &= n_k\mu_{\text{MTD}}\frac{E^{\text{UL}}_{\text{MTD},k}}{T_{as}} + \dot{P}_{\text{MTD}}T_f \\ &= n_k\mu_{\text{MTD}}\frac{E^{\text{UL}}_{\text{MTD},k}}{T_{as}} + \dot{P}_{\text{MTD}} \cdot [S(T_{ts}+T_{as})+T_\sigma] \qquad [\text{W}]. \end{aligned} \tag{4.24}$$

4.2.2 SAP-RARAP Power Consumption Model

For SAP-RARAP, when the access policy adopted requires CSI, the modeling of its power consumption model is essentially the same as the model presented in subsection 4.2.1, as long as the training step must be performed in order to allow the estimation of channel qualities by MTDs. The only difference is the fact that all MTDs perform data uplink using equal uplink power, *i.e.*, $\rho_{\text{MTD},k} = \rho_{\text{MTD}}\ \forall k \in \{1,\ldots,K\}$, resulting in a unique MTD uplink energy for all devices, $E^{\text{UL}}_{\text{MTD}}$. Hence, when s-SCP or CARP policies are adopted in SAP-RARAP scenarios, equation (4.24) can be rewrited as

$$P_{\text{MTD},k} = n_k\mu_{\text{MTD}}\frac{E^{\text{UL}}_{\text{MTD}}}{T_{as}} + \dot{P}_{\text{MTD}}T_f \qquad [\text{W}], \tag{4.25}$$

while the BS and RIS powers computations can be obtained by equations (4.22) and (4.23), respectively, and T_f is the same as in equation (4.16).

Notice that, when an access policy that blindly performs the data uplink,*i.e.*, without CSI, is adopted, the training phase of the TDMA frame can be discarded by

[3] Notice that equation (4.22) can be rewritten in terms of $\overline{P}_{\text{BS}}$ and ρ_{BS} as $P_{\text{BS}} = S\mu_{\text{BS}}\rho_{\text{BS}} + \overline{P}_{\text{BS}}$, where $\overline{P_{\text{BS}}}$ is the fixed power consumed in each TDMA frame; however, as will be discussed in subsection 4.2.2, in SAP-RARAP the duration of the TDMA frame can be reduced, hence it is more adequate to express the total power as a function of the energies and slots duration.

setting $T_t = 0$, which implies that $T_{ts} = T_\sigma = 0$, resulting in a reduced frame time equal to

$$T_f = ST_{as}. \tag{4.26}$$

As a result, the expressions derived for DAP-RARAP can be simplified considering the new frame duration. Hence, for IRSAP or CRDSAP RA protocols aided by RIS, the power consumed by the BS is

$$P_{\text{BS}} = \dot{P}_{\text{BS}} T_f = \dot{P}_{\text{BS}} S T_{as} \qquad [\text{W}], \tag{4.27}$$

where the term associated with the BS pilots broadcasts of equation (4.22) is discarded because the BS does not need to transmit data pilots during training. Similarly, the RIS consumed power is obtained as

$$P_{\text{RIS}} = N\dot{P}_n T_f = N\dot{P}_n S T_{as} \qquad [\text{W}], \tag{4.28}$$

while P_{MTD} is calculated as

$$P_{\text{MTD},k} = n_k \mu_{\text{MTD}} \frac{E^{\text{UL}}_{\text{MTD}}}{T_{as}} + \dot{P}_{\text{MTD}} T_f = n_k \mu_{\text{MTD}} \frac{E^{\text{UL}}_{\text{MTD}}}{T_{as}} + \dot{P}_{\text{MTD}} S T_{as} \qquad [\text{W}]. \tag{4.29}$$

For both protocols, the total power consumed by the K MTDs can be obtained by

$$P_{\text{MTDS}} = \sum_{k=1}^{K} P_{\text{MTD},k} \quad [\text{W}]. \tag{4.30}$$

Finally, the total power consumption is determined by the summation of the powers consumed by the BS, RIS, and all K MTDs:

$$P_{\text{T}} = P_{\text{BS}} + P_{\text{RIS}} + P_{\text{MTDS}} \qquad [\text{W}]. \tag{4.31}$$

4.3 Throughput, Energy Efficiency and Fairness Metrics

To evaluate the performance of proposed RA schemes, we analyze four main performance metrics: total system throughput, the total system energy efficiency (EE), the EE of the MTDs and the system fairness. In an arbitrary TDMA frame, the *system throughput* G can be obtained as:

$$G = \frac{A}{T_f} \qquad \left[\frac{\text{packets}}{\text{s}}\right], \tag{4.32}$$

where A is the number of successfully decoded packets and T_f is the total TDMA frame duration for the adopted RA protocol and access policy[4].

[4] While computing equation (4.32), the frame duration T_f must be adapted according to the adopted RA protocol and RA policy. If the considered method requires the training phase, T_f must be obtained as in (4.16). If training is not required, equation (4.26) must be considered.

To evaluate the energy efficiency (EE), we deploy two metrics: *i*) the total energy efficiency η_{T}; and *ii*) the MTD's energy efficiency η_{MTD}, which are calculated as follow:

$$\eta_{\text{T}} = \frac{G}{P_{\text{T}}} \quad \left[\frac{\text{packets}}{\text{joule}}\right]; \tag{4.33}$$

$$\eta_{\text{MTD}} = \frac{G}{P_{\text{MTDS}}} \quad \left[\frac{\text{packets}}{\text{joule}}\right]. \tag{4.34}$$

Notice that the total EE metric is directly affected by the system throughput, and due to the most amount of power is consumed by the BS, the total EE is not severely affected by RIS' number of elements or the power level adopted by MTDs to uplink its data packets. Furthermore, in practical implementations, it is much easier to provide large amounts of power for the BS and the RIS, as long as they can be directly connected to an electrical power grid. Hence, BS and RIS have 'unlimited' power available. On the other hand, on the MTDs' side, one must highlight that IoT devices are usually positioned in places that are difficult to physically access; as a result, the electrical power grid is difficult or limited, while their battery budget is also restricted. Hence, investigating η_{MTD} (instead total EE) is much more interesting because it can shed light on the viability of the DAP-RARAP protocol in crowded MTC scenarios: the higher the η_{MTD}, the longer the batteries of the MTDs will last, avoiding human intervention to replace the batteries of the MTDs.

Finally, the system fairness is evaluated according to equation (4.35), also known as *Jain's fairness index* [45]:

$$J(x_1, x_2, \ldots, x_n) = \frac{\left(\sum_{k=1}^{n} x_k\right)^2}{n \cdot \sum_{k=1}^{n} x_k^2}, \tag{4.35}$$

where x_k is the attainable spectral efficiency of MTD k, which is computed according to equation (4.36):

$$x_k = \text{SE}_k = \left(\frac{G_k T_{as}}{T_f}\right) \log_2\left(1 + \gamma_k\right), \quad \left[\frac{\text{bits/s}}{\text{Hz}}\right] \tag{4.36}$$

where G_k is a binary variable that indicates if the packet sent by MTD k was successfully decoded. Notice that the Jain's fairness indexes do not measure the quality of the system, just its fairness. Hence, in equation (4.35), an fairness index equals to 1 can happen if and only if all MTDs, homogeneously, presented a same good SE, a same medium SE or a same bad SE in a single TDMA frame. On the other hand, if some MTDs have a good SE while others have achieved poorer ones, Jain's index will be smaller.

5 CONTRIBUTIONS AND SIMULATION RESULTS

In this chapter we discuss the main contributions and simulation results of this Master's Dissertation. All simulation scripts have been implemented in *Python* and, to allow reproducibility of the presented results, We make these scripts available in a Github repository. This repository can be accessed here. We begin by providing a Table of default simulation parameters. Next, we present several simulation results that aims to clarify how the TDMA frame is integrated with the RIS functionality and how the reflective surface impacts the studied communication cell within each access slot of the adopted TDMA frame. Then, we discuss the definition of some simulation parameters, looking for feasible and practical values and justifying the selection of each one, following 5G standard and minimal requirements for future wireless networks. The selection of these parameters is supported by simulation results, which are shown in Section 5.4. Finally, we conclude the Chapter by analyzing the performance of SAP-RARAP and DAP-RARAP. Specifically, we extend the main findings of accepted works investigating the achievable throughput, total EE, and MTDs' EE as a function of the system variables, presenting a detailed discussion of the four RA protocols variants studied. Also, we analyze the behavior of the throughput, total system's EE and MTDs' EE metrics as a function of many system parameters, including the number of contending MTDs (K), MTDs' transmission power ($\rho_{\text{MTD},k}$), number of RIS elements (N), number of available time slots (S) and blockage attenuation (ξ). Discussions on the adopted wireless channel configurations (Rice fading channel model parameters) and the BS and MTD transmit *energies* and how such parameters can be associated with the duration of each training and access slot time periods are also discussed.

5.1 Default System and Channel Simulation Parameters Values

The default simulation parameters adopted in this Master's Dissertation work are summarized in Table 3. Many of those parameters were taken from previous work, which is cited in Table 3. Furthermore, some of these parameters were redefined following the 5G perspective standards. and minimum requirements and are justified by physical principles and limitations. We discuss in more detail in Section 5.4.

Table 3 – Adopted Simulation Parameters Values (Default)

Parameter	**Value**	**Reference**
Carrier frequency	$f = 3$ GHz	
# Training slots	$S = 20$	
# Access slots	$J = S = 20$	
Noise power	$\sigma_n^2 = -86$ dBm	
SIC SNR threshold*	$\gamma_{\text{TH}} = 5$ dB	
Training pilot length	$\tau = 1$	
Reflected Link Rice Factor	$\delta = 1.5$	
Direct Link Rice Factor (Green Area)	$\kappa_1 = 9$	
Direct Link Rice Factor (Red Area)	$\kappa_2 = 3/7$	
Default Attenuation (Green Area)	$\xi_1 = 0$ dB	
Default Attenuation (Red Area)	$\xi_2 = -40$ dB	
Localization threshold (DAP)	$\sigma_{\text{TH}}^2 = 1 \times 10^{-3}$	
Total frame time (with training)	$T_f = 800$ μs	
Access slot time	T_{as}	
Training slot time	$T_{ts} = 0.2T_{as}$	
σ-slot time	$T_\sigma = 0.1T_{as}$	
Total Training Time	$T_t = ST_{ts} + T_\sigma$	
Total Access Time	$T_a = ST_{as}$	
MTD angle range	$\theta_k \in [0, \pi]$	
MTD distances range	$d_k^r \in [20, 100]$ m	
MTD antenna gain	$\alpha_k = 5$ dB	
MTD power consumption rate*	$\dot{P}_{\text{MTD}} = 7.75$ W/s	Subsection 5.4.3
MTD transmit power*	$\rho_{\text{MTD},k} = 10$ mW (SAP) $\rho_{\text{MTD},k} \in (1, 10)$ mW (DAP)	[28]
MTD transmit energy	$E_{\text{MTD}}^{\text{UL}} = T_{as}\rho_{\text{MTD}}$	
MTD power amplifier inefficiency	$\mu_{\text{MTD}} = 2.0$	[46]
BS angle	$\theta_{\text{BS}} = \pi/4$	
BS distance	$d_{\text{BS}} = 20$ m	
BS power consumption rate*	$\dot{P}_{\text{BS}} = 1715$ W/s	Subsection 5.4.3
BS transmit power	$\rho_{\text{BS}} = 100$ mW	[28]
BS transmit energy	$E_{\text{BS}}^{\text{UL}} = T_{ts}\rho_{\text{BS}}$	
BS power amplifier inefficiency	$\mu_{\text{BS}} = 1.6$	[46]
# RIS elements at each axis	$N_x = N_z = 10$	
# RIS elements	$N = N_xN_z = 100$	
RIS element size	$d_x = d_z = 0.1$ m	
RIS processing power density	$\dot{P}_n = 3$ W/s	Subsection 5.4.3

*Parameters defined according to simulations provided in Section 5.4.

5.2 RIS Integration with the TDMA-based Framework System

Before presenting and discussing the performance of the studied RA protocols, it is paramount to explain and exemplify how the RIS impacts the MTDs SNRs during a TDMA frame. In this subsection, we shed light to that by showing the SNRs heatmaps of the uplink powers within the communication cell during a TDMA frame with $S = 10$

access slots. Simulation results for the SAP-RARAP are shown in Figure 5 and for DAP-RARAP in Figure 6. Recall that, in SAP-RARAP, all MTDs transmit with the same power, while in DAP-RARAP MTDs that need RIS assistance transmits with a higher power level.

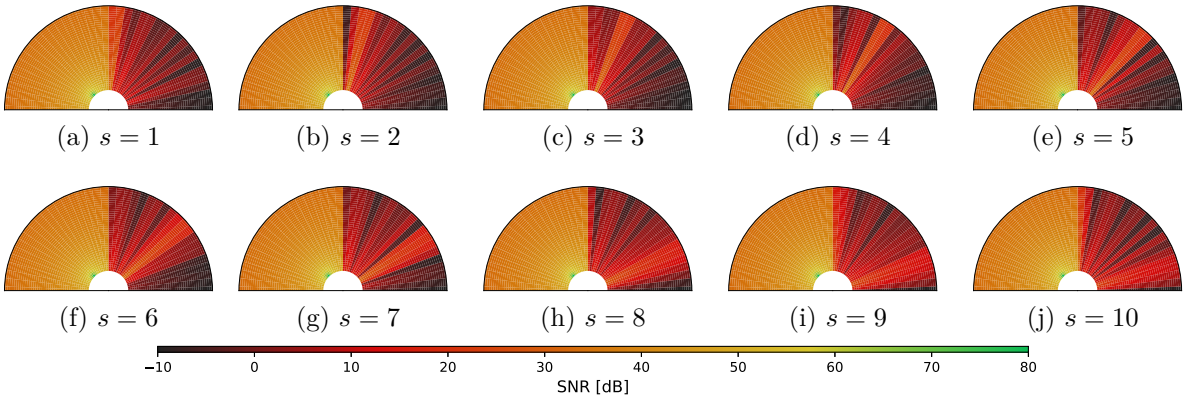

Figure 5 – Heatmap of the BS received power in the adopted communication cell for SAP-RARAP protocol ($\rho_{\text{MTD}} = 10$ mW). It is considered a TDMA frame with $S = 10$ slots. BS and RIS positioning is the same as in Fig. 2.

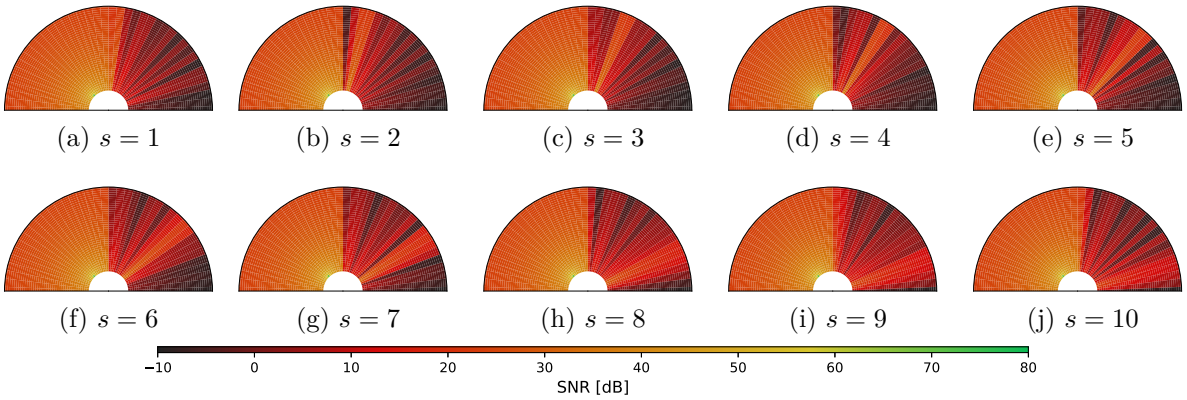

Figure 6 – Heatmap of the BS received power in the adopted communication cell for DAP-RARAP protocol ($\rho_{\text{L}} = 1$ mW and $\rho_{\text{H}} = 10$ mW). It is considered a TDMA frame with $S = 10$ slots. BS and RIS positioning is the same as in Fig. 2.

We notice that regardless of the adopted protocol, both sides of the communication cell are subject to very unique characteristics. Specifically, the left side of the cell showed substantially higher SNR levels than the right side, which is expected due to the predominantly LoS channel to which these MTDs are submitted and the fact that their signals do not suffer any attenuation from blockage. The BS is located near the green region, which explains the remarkable average SNR obtained in such green area (the left upper quadrant in Fig. 2). On the other hand, the SNR patterns observed on the right upper quadrant clearly vary at each time interval due to the RIS operation: at each time

interval, it is possible to see an orange beam pointing to a specific direction of the communication cell, increasing the SNRs of the MTDs located at this specific angular range at each time slot in the right upper quadrant.

In addition, it should be noted that the RIS can effectively cover the regions of the cell positioned in front of it because the beams can be clearly identified for $s \leq 6$. As we increase θ_k, we notice that the RIS beam becomes wider and darker, indicating that reflective surfaces lose their efficiency in reflecting the signal precisely when the aimed position to cover tends to a region parallel to the arrangement of elements. For example, we noticed that the MTDs at the cell edge with $\theta_k > 85^{\text{o}}$ presented an average SNR of less than 0 dB, which prevents the packets sent by these MTDs from being successfully decoded by the BS, harming overall system performance.

Compared with Figures 5 and 6, it can be seen that the right side of the communication cell is subject to the same power during all slots, regardless of the adopted protocol. This behavior is expected because $\rho_{\text{MTD}} = \rho_{\text{H}}$. However, when using DAP-RARAP, the SNRs observed in the left region of the cell are much lower than those obtained with SAP-RARAP because these MTDs transmit with the lower power level, ρ_{L}. Nevertheless, achieving a lower SNR in mMTC scenarios may not be a drawback because MTDs usually do not require high data transmission, then they do not need to fulfill high capacity requirements. For these scenarios, techniques that increase the battery lifetimes of devices are much more appealing because IoT sensors are usually positioned in places where human handling is challenging. Hence, these devices must be carefully designed.

Later, we will compare the achievable MTDs' EE when both RA protocols are adopted. We show that it is possible to obtain an optimal EE operation point, where all MTDs can satisfy the SIC SNR threshold and still achieve a sufficient SE to fulfill B5G minimum requirements.

5.3 Access Policies Functionality - A Practical Example

In this section, we show how the RIS diversity can induce MTDs to select the best time slots for data uplink. To do that, we fixed the position of 20 MTDs inside the communication cell at different angular positions. Half of them are close to the inside region of the cell, while the remaining ones are near the cell edge. The positions of these MTDs are shown in Figure 7a. Furthermore, in Figure 7b unveils the average uplink SNRs that MTDs indexed in Figure 7a are submitted during the access phase of a TDMA frame with $S = 20$ slots. The results are shown for the SAP-RARAP protocol, *i.e.*, all MTDs use $\rho_{\text{MTD}} = 10$ mW.

The heatmap shown in Figure 7b clarifies how important the training phase is for MTDs positioned at the right side of the communication cell (MTDs 1–5 and 11–15). For

those MTDs, we note that their SNRs are related to the angular position that they are located, being higher when the RIS beam covers their respective angular position. Hence, inducing MTDs from this half of the cell to uplink their data packets in these slots, we can not only increase the chance to fulfill the minimum SIC requirement at BS but also avoid several collisions among them, as long as MTDs from distinct angular positions will rarely send a packet in the same slot. On the other hand, MTDs 6–10 and 16–20 have an almost constant SNRs throughout the whole TDMA frame, which indicates that they do not need preference to uplink their data packets in specific time slots.

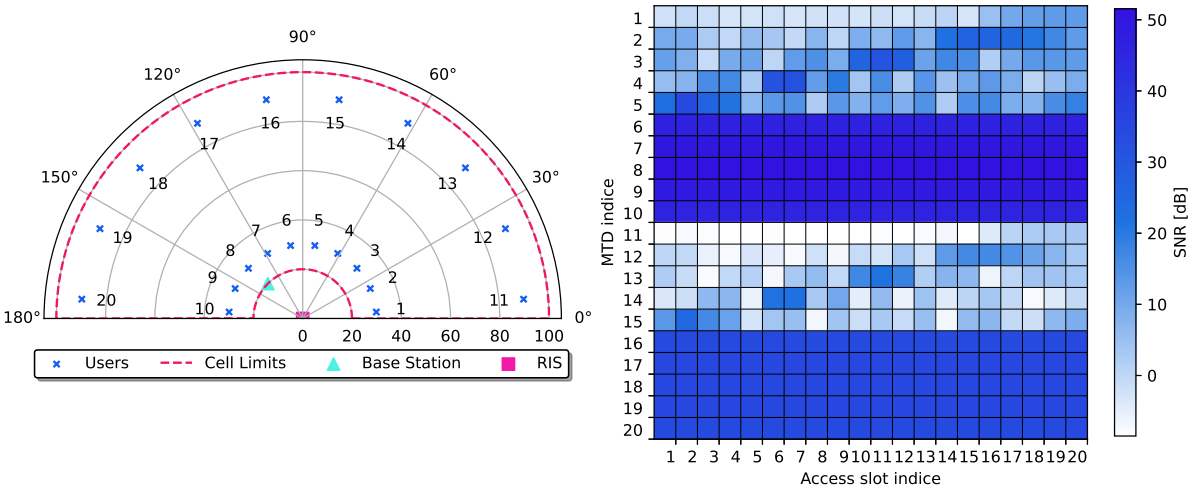

(a) Simulation scenario

(b) Average SNRs

Figure 7 – (a) Location of MTDs at the communication cell; (b) average SNRs that MTDs experience during a TDMA frame with $S = 20$ time slots.

After examining the average SNR experienced by MTDs in a TDMA frame, a key question arises: *How do these SNR values influence the probability of an MTD selecting each time slot for uplink transmission under the adopted access policy?* To address this, we analyze the probabilities presented in Figure 8 for all studied access policies. It is evident that IRSAP and CRDSAP (illustrated in Figures 8a and 8b, respectively) do not introduce any bias in slot selections among MTDs. In this scenario, the probability of an MTD transmitting a packet in any given time slot is uniform and equals $1/S = 1/20 = 0.05$. Conversely, when access policies that require channel state information (CSI) are employed, we observe an intriguing behavior. As shown in Figures 8c and 8d, MTDs located on the right side of the communication cell prefer to transmit packets during slots where their SNR values are higher, resulting in a discernible pattern throughout the TDMA frame. In contrast, MTDs on the left side of the cell continue to distribute their transmissions uniformly across all S slots. This phenomenon can be attributed to the left-side MTDs being less affected by RIS diversity effects, as they experience a relatively stable channel characterized by a strong line-of-sight (LoS) link to the base station, along with variability introduced by small-scale fading. Therefore, even when utilizing a policy

like s-SCP, which opts for slots with superior channel quality, the distribution of packet transmission remains, on average, unbiased for these MTDs.

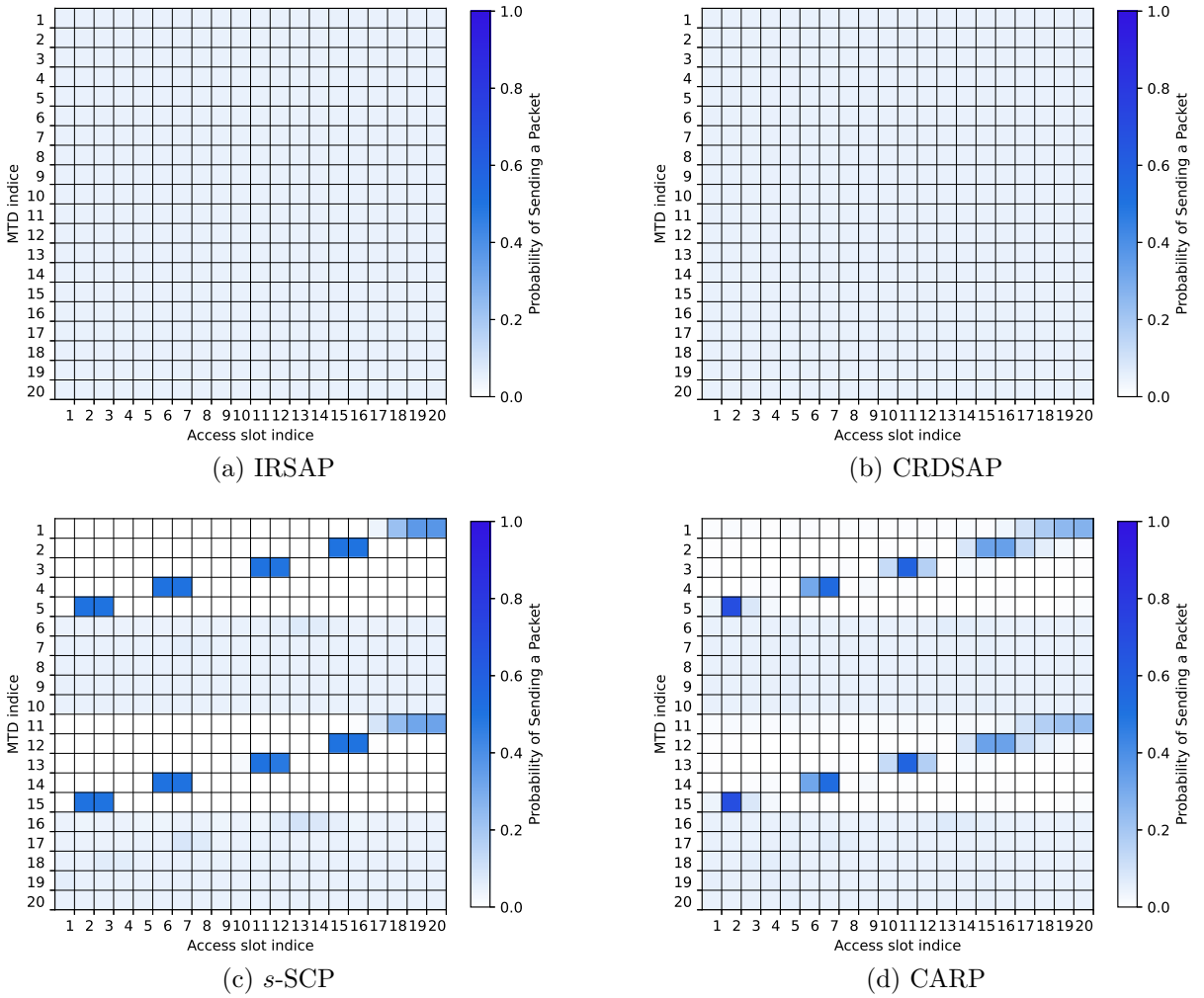

(a) IRSAP (b) CRDSAP

(c) s-SCP (d) CARP

Figure 8 – Probability of MTDs shown in Figure 7a sending a packet at each time slot, considering all four studied random access policies.

5.4 Selecting Feasible Simulation Parameter Values

This section presents in detail a discussion regarding the selection of proper simulation parameter values. This is paramount component of this Master's dissertation, as it will search for values that aim to faithfully represent a real IoT system. As long as this work is theoretical and all the results presented here were obtained numerically via Monte Carlo simulation (MCS), the adopted system and channel parameter values must be carefully assigned in order to provide a good correlation with future implementation of the studied RA protocols. Furthermore, the discussion is provided step-by-step, allowing the reproducibility of the work and an eventual parameter adaptation, if needed.

We start by defining the system noise power σ_n^2 in Subsection 5.4.1. Subsec-

tion 5.4.2 presents a discussion regarding the selection of proper SIC minimum threshold γ_{TH} for the signal detection at BS. The processing power density terms for BS and MTDs ($\dot{P}_{\text{BS}}$ and $\dot{P}_{\text{MTD}}$, respectively) are defined in Subsection 5.4.3.

5.4.1 Noise Power Definition

In a communication system, thermal noise can severely affect the system performance. The *noise power density*, denoted by N_0, can be calculated as:

$$N_0 = kT \qquad \left[\frac{\text{W}}{\text{Hz}}\right], \tag{5.1}$$

where $k = 1.38 \times 10^{-23}$ J/K is the Boltzmann constant and T is the temperature, expressed in kelvins. In an ideal system at room temperature, *i.e.*, $T \approx 300$ K, we have

$$N_0 \approx 4.14 \times 10^{-21} \text{ W/Hz} \quad \text{or} \quad N_0 \approx -174 \text{ dBm/Hz}.$$

Typical radio receivers usually enhance N_0 due to the noise figure (NF) of the first stage of RF pre-amplifier (namely low-noise amplifier, LNA), resulting in higher N_0 values:

$$N_0 = kT \cdot 10^{\frac{\text{NF}}{10}}. \tag{5.2}$$

Considering a receiver with a noise figure of NF = 5 dB, we have $N_0 \approx -169$ dBm/Hz.

The noise power σ_n^2 can be obtained by multiplying N_0 by the total system bandwidth, denoted by B:

$$\sigma_n^2 = N_0 B. \tag{5.3}$$

ITU report M.2410-0 [1] defines the minimal bandwidth expected for 5G networks as $B_{\text{MIN}} = 100$ MHz. As long as mMTC scenarios do not require high data traffic, we will assume that the studied system requires a bandwidth $B = 200$ MHz to operate. Hence, let us obtain the total noise power by using equation (5.3):

$$\sigma_n^2 = N_0 B = -169 \ \frac{\text{dBm}}{\text{Hz}} \times 200 \text{ MHz} \approx -86 \text{ dBm}.$$

5.4.2 SIC Threshold Considerations

The purpose of this subsection is to investigate how the throughput metric is affected by the SIC threshold value γ_{TH}. More important, we search for suitable γ_{TH} values that can be adopted in real scenarios to truly represent the system performance. Establishing a low γ_{TH} value would result in a performance above the expectations because low SNR packets would be able to be decoded, enhancing the throughput metric. However, in practical scenarios, detectors are not able to perfectly decode signals under very-low and low SNR regime, which justifies the need to select suitable (higher) γ_{TH} values to obtain a performance that truly represents a real application of the protocols studied. In addition, selecting higher γ_{TH} values would severely affect the wireless communication system

performance, which would complicate the packet detection by the BS receiver. Usually, detectors do not require an extremely high signal SNR to perform the detection with remarkable reliability. Hence, establishing an extremely high γ_{TH} value is also unpractical in real scenarios.

Considering the four implementations for both SAP and DAP random access protocols, presented respectively in Subsection 4.1.2 (Table 1) and Subsection 4.1.3 (Table 2), the performance of the throughput G as a function of γ_{TH} is shown in Figure 9. Simulation parameters adapted from Table 3 for this simulation are summarized in Table 4.

Parameter	**Value**
Number of MTDs	$K = 10$
SIC Threshold	$\gamma_{\text{TH}} \in [0, 30]$ dB

Table 4 – Adopted simulation parameter values that overrides those from Table 3 in the simulation shown in Figure 9.

First of all, recall that SAP-RARAP obligates all MTDs to use the same uplink power, while two power levels are available for MTDs in DAP-RARAP, with one of these levels being lower than the power level adopted by SAP-RARAP. Stated that we can see in Figure 9a that under low γ_{TH} scenarios, the 2-SCP policy achieved the best performance, which indicates that this policy can efficiently leverage CSI to avoid collisions among MTDs, also surpassing the CARP performance through all γ_{TH} values studied. Moreover, when we analyze the performance obtained by access policies that do not use CSI we note that the higher the average number of packets sent, the worse the throughput. This behavior is due to the fact that with more replicas being sent, the higher the probability of a packet being transmitted in a slot with poor channel quality, avoiding its decodification and interference cancellation from other slots, especially from MTDs located at the red area.

The performance of DAP-RARAP, Figure 9b, shows that the double-policy approach can achieve performance near the peak performance obtained with SAP-RARAP variants for lower γ_{TH} values. Hence, one can say that inducing MTDs at the red region to not transmit their data packets with an access policy that does not leverage CSI enhances the robustness of the RA protocol, even resulting in a performance gain with respect to the single-policy method, as we can observe in Figure 9c for $\gamma_{\text{TH}} < 15$ dB. A curious behavior can be noted when a comparison is made between SAP-RARAP and DAP-RARAP: when SAP-RARAP is adopted, the IRSAP policy presented the worse throughput performance; however, for DAP-RARAP, policy combinations that use IRSAP presented the best results, being able to outperform the SAP-RARAP for lower γ_{TH} values. This clarifies that letting MTDs from the red area uplink their packets using IRSAP induces a performance degradation as long as more packets are received with an SNR under the

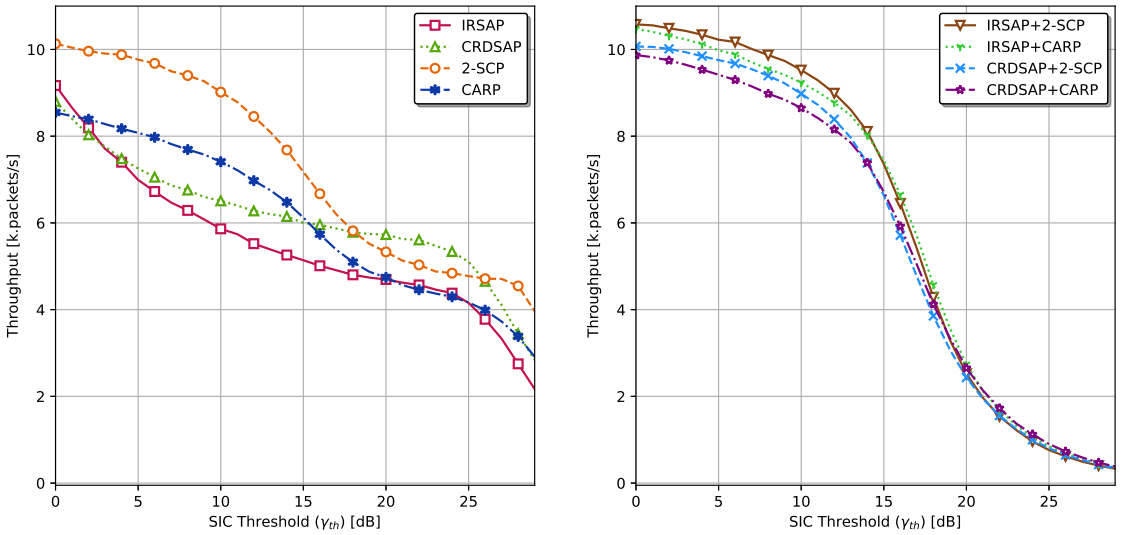

(a) SAP-RARAP

(b) DAP-RARAP

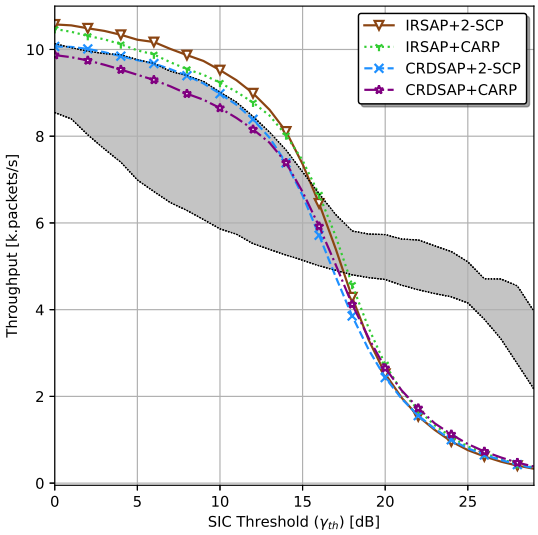

(c) Comparison

Figure 9 – System throughput G as a function of the SIC threshold γ_{TH} for main implementations of (a) SAP-RARAP and (b) DAP-RARAP protocols. A performance comparison between both protocols is provided in (c).

pre-established SIC threshold. This explanation can also be extended for CRDSAP, but as long as the average number of packets sent by MTDs that use this policy is lower than the average number of packets obtained with IRSAP, the performance degradation is not that notorious.

In this work, for simulation purposes, we adopt $\gamma_{\text{TH}} = 5$ dB as the SIC receiver threshold, which results in a much more realistic performance than one obtained in previous works, such as [28, 42].

5.4.3 Processing Power Density Terms

We start this subsection by discussing how the constant terms in our EE model can be calibrated. The terms that we are trying to calibrate are $\dot{P}_{\text{BS}}$ and $\dot{P}_{\text{MTD}}$, which models the fixed average powers consumed in terms of watts per second [W/s], at the BS and at each MTD, respectively. With respect to the BS, this power is used for synchronization, signal processing, operating the SIC algorithm, backhaul operations, and cooling. Similarly, at the MTDs side, $\dot{P}_{\text{MTD}}$ is the amount of power consumed during signal processing, estimation of channel qualities, decisions that involve the access policies rules, and synchronization.

First, consider equation (4.22). The total power expended by the BS in a TDMA frame is the summation of the power expended with pilot downlink[1] and the power expend with processing. Let us denote the ratio between the RF component and the total BS power as $RF_{\text{BS}}\%$, *i.e.*, RF transmission power percentage:

$$RF_{\text{BS}}\% = 100\times\frac{S\mu_{\text{BS}}\rho_{\text{BS}}}{S\mu_{\text{BS}}\rho_{\text{BS}} + \dot{P}_{\text{BS}}\cdot[S(T_{ts}+T_{as})+T_{\sigma}]}. \tag{5.4}$$

Repeating this analysis at the MTD side, we obtain

$$RF_{\text{MTD}}\% = 100\times\frac{\overline{n}_k\mu_{\text{MTD}}\rho_{\text{MTD}}}{\overline{n}_k\mu_{\text{MTD}}\rho_{\text{MTD}} + \dot{P}_{\text{MTD}}\cdot[S(T_{ts}+T_{as})+T_{\sigma}]}, \tag{5.5}$$

where $\overline{n}_k = \mathbb{E}\{n_k\}$ it the average number of packets send by a MTD, which depends on the adopted access policy.

We are looking for feasible $\dot{P}_{\text{BS}}$ and $\dot{P}_{\text{MTD}}$ values. At the BS side, following the discussions presented in [47, 48] with respect to BS power consumption models in recent cellular networks, one must consider that 70% of the power used at the BS is expended in RF chains and its respective power amplifiers. In the studied scenario, this can be interpreted as the power required to transmit the pilot sequences through the S training slots. Due to the fact that BS power amplifiers are imperfect (which is modeled by parameter μ_{BS}), a high percentage of the energy needed to fulfill the downlink power requirements

[1] Notice that if we consider the case when SAP-RARAP is adopted with an access policy that do not use CSI, the amount of power expended at the BS with pilot downlink is null.

is undesirably dissipated as heat, significantly augmenting the power expenditure needed to achieve the effective RF power.

On the MTD side, a similar analysis can be made; however, one can consider that a higher percentage of power is expended with RF circuits instead. This assumption can be justified by the fact that MTDs usually use much less power than the BS, hence reducing the amount of energy that is converted in heat at its PAs. Moreover, in the development of IoT devices, several EE-friendly approaches can be adopted to increase battery lifetime, such as the so-called *sleep mode* and *deep sleep mode* [49]. Adopting these techniques, IoT devices can shut down electronic circuits that are not being used, keeping only some crucial operations running in the background, such as timers. When these devices are requested, they return to the operational mode, activating their circuitry and executing the required tasks, *e.g.*, actuating in the environment, collecting data, or sending data measurements. When it is done, they can return to the *sleep mode* and wait for another request. Due to the existence of such "saving power" techniques, in this work, we assume that the relative power consumption with RF circuits in the MTD devices is as high as $RF_{\text{MTD}}\% = 88\%$. Established that, we can search for a suitable range of $\dot{P}_{\text{MTD}}$ values, which is investigated in Figure 10.

The black curve in Figure 10 depicts $RF_{\text{BS}}\%$ as a function of $\dot{P}_{\text{BS}}$, as defined in equation (5.4), while the other are referred to the $RF_{\text{MTD}}\%$ obtained by varying $\dot{P}_{\text{MTD}}$, according to equation (5.5) with an specific access policy. In this last case, we obtained the average $\overline{n}_k$ that is achieved with each access policy previously by MCS, and applied in (5.5), resulting in the average RF percentage for all studied access policies. The average number of packets sent by MTDs for all adopted policies are summarized in Table 5 for $S = 20$ time slots[2]. The BS power processing density, $\dot{P}_{\text{BS}}$, is obtained directly from the black curve and $\dot{P}_{\text{MTD}}$ is defined as the average value obtained by all policies individually. This average value is taken aiming to establish a fair result to compare all policies, as long as due to the variable value of $\overline{n}_k$, it is not possible to obtain a common $RF_{\text{MTD}}\%$ value that fulfills $RF_{\text{MTD}}\% = 88\%$ for all access policies simultaneously.

Parameter	**Access Policy**			
	IRSAP	**CRDSAP**	**2-SCP**	**CARP**
$\overline{n}_k$	3.78	2.00	2.00	1.33

Table 5 – Average number of packets $\overline{n}_k$ send by MTDs when a specific access policy is adopted ($S = 20$ slots).

Observing the black curve, we can notice that the point in the x-axis that results in $RF_{\text{BS}}\% = 70\%$ is approximately $\dot{P}_{\text{BS}} \approx 1715$ [W/s]. This is the value that will be adopted

[2] Notice that s-SCP and CRDSAP send always the same amount of replicas regardless of the number of time slots S. However, for CARP and IRSAP, the number of packets tend to vary according to S.

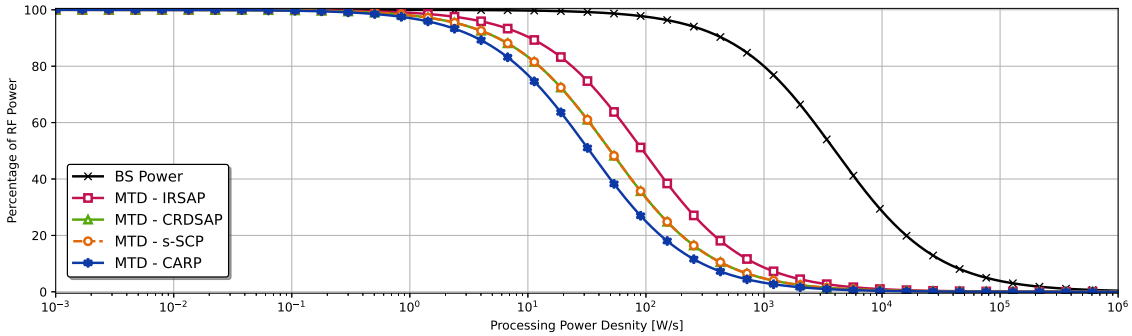

Figure 10 – Percentage of total expend power at the BS and at MTDs (with all studied access policies) as a function of the processing power density.

as the BS processing power density. Similarly, with respect to the MTDs processing power densities, simulation results show that for 2-SCP and CRDSAP, the $\dot{P}_{\text{MTD}}$ is approximately 6.81 W/s. When CARP is adopted, $\dot{P}_{\text{MTD}} \approx 4.53$ W/s, and for IRSAP we got $\dot{P}_{\text{MTD}} \approx 12.88$ W/s. Hence, taking the average of these values, we have $\dot{P}_{\text{MTD}} = 7.75$ W/s, which has been adopted as an average power density consumption at each MTD device[3].

5.4.4 Definition of MTDs Uplink Power

The main objective of this section is to find the maximum achievable throughput for all RA protocols and access policies. We investigate the throughput metric as a function of MTDs uplink power, and results are shown in Figure 11. In Figure 11a, the throughput metric for the SAP-RARAP is shown as a function of MTDs uplink power, ρ_{MTD}, which is common for all MTDs. While Figures 11b and 11c depicts the performance of the DAP-RARAP as a function of the uplink power of MTDs at both sides of the communication cell individually: ρ_{L} and ρ_{H}, respectively. In these cases, the power level that is not varied is keep fixed at $\rho_{\text{MTD}} = 10$ mW. Simulation parameters are detailed in Table 6.

Subfigures	**Simulation Parameters**		
	MTDs Power - ρ_{MTD}	MTDs Power - ρ_{L}	MTDs Power - ρ_{H}
11a and 12a	$\rho_{\text{MTD}} \in (0.1\text{ nW}, 0.1\text{ kW})$	-	-
11b and 12b	-	$\rho_{\text{L}} \in (0.1\text{ nW}, 0.1\text{ kW})$	$\rho_{\text{H}} = 10$ mW
11c and 12c	-	$\rho_{\text{L}} = 10$ mW	$\rho_{\text{H}} \in (0.1\text{ nW}, 0.1\text{ kW})$

Table 6 – Simulation parameters that overrides those from Table 3 in the simulations shown in Figures 11 and 12.

Observing Figure 11a, we note that access policies that leverage CSI can achieve their maximum throughput at a lower ρ_{MTD} value when compared with access policies that

[3] Notice that it is impossible to determine a $\dot{P}_{\text{MTD}}$ value which results in $RF_{\text{MTD}}\% = 88\%$ for all access policies adopted in this Dissertation simultaneously. This happens because $\overline{n_k}$ varies according to Table 5. Because of that, we adopt $\dot{P}_{\text{MTD}}$ as the average value observed with all studied policies, aiming a fair EE comparison among different policies. The average value obtained was $\dot{P}_{\text{MTD}} = 7.75$ W/s.

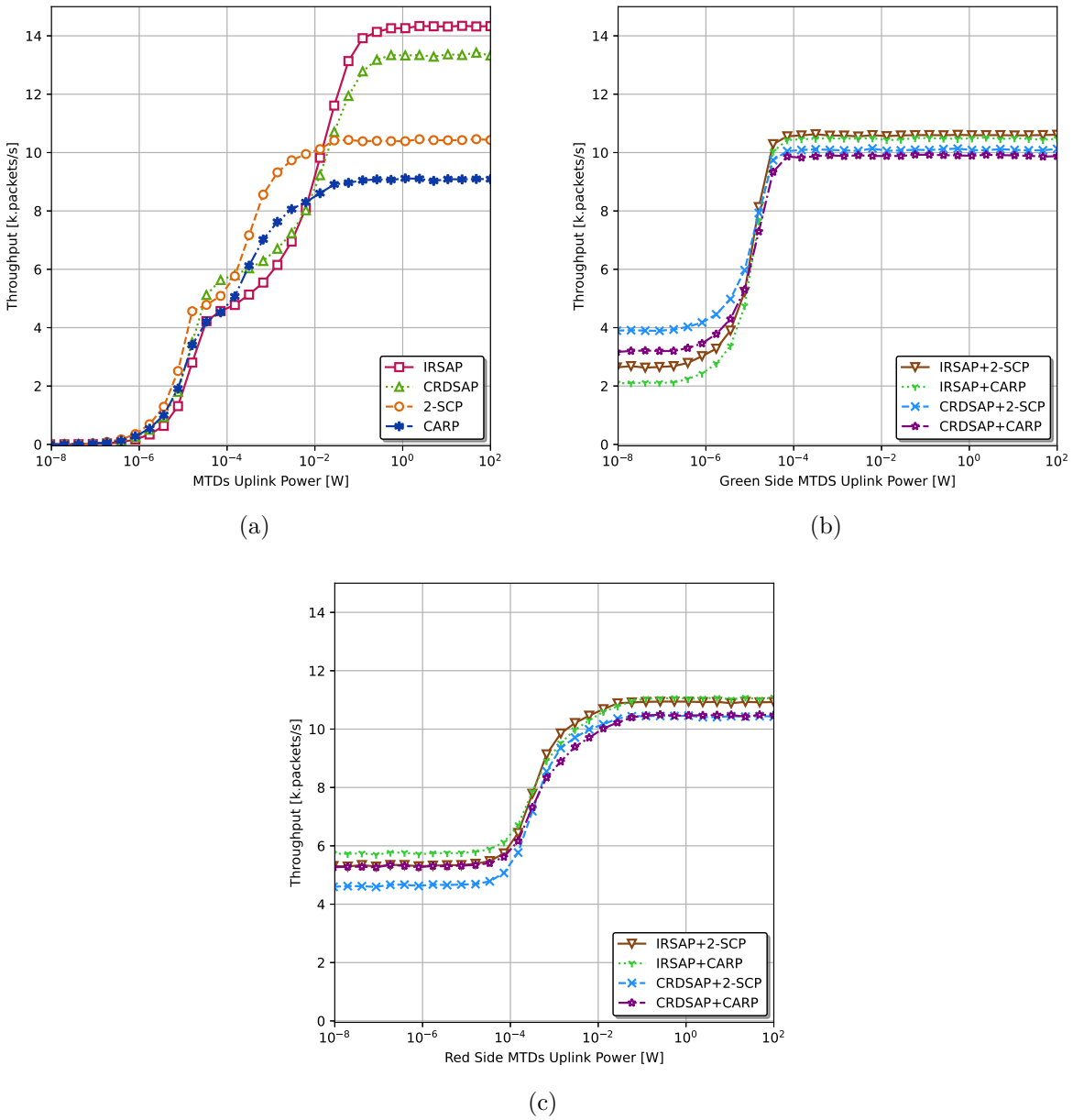

Figure 11 – Achievable throughput G of the studied protocols: (a) SAP-RARAP as a function of MTDs uplink power; (b) DAP-RARAP as a function of green area MTDs uplink power and (c) DAP-RARAP as a function of red area MTDs uplink power.

do not require CSI. However, the plateau achieved is higher for IRSAP and CRDSAP when compared with CARP and 2-SCP, indicating the optimality of these access policies under high SNR conditions. However, this higher peak can only be achieved at extremely high uplink power values (above 200 or even 500 mW), which is unfeasible for mMTC scenarios. We also notice the blockage effect at the curves around $\rho_{\text{MTD}} = 100$ μW, indicating that this power level is able to fulfill the SIC requirement for half of the cell users – specifically, those located in the green area.

When adopting DAP-RARAP, by varying ρ_{L} (Figure 11b), one can say that MTDs at the green area achieved its maximum throughput at $\rho_{\text{L}} \approx 100$ μW. Conversely, when

ρ_{H} is analyzed in Figure 12c, we notice that MTDs from the red area can reach the throughput plateau only at $\rho_{\text{H}} \approx 100$ mW due to the blockage attenuation and double path loss effect in the reflected link. However, *regardless of being able to achieve the peak throughput in packets per second, how many bits per second the studied protocols are able to transmit?*

5.4.4.1 System Spectral Efficiency

Considering the adopted TDMA frame, during the training phase, MTDs are not allowed to transmit any data, which causes overhead. If all slots of the access phase were leveraged to transmit a data packet by a different MTD (which would be an optimal scenario), we could define the system sum SE as follows:

$$\Sigma\text{SE} = \left(\frac{T_f - T_t}{T_f}\right) \sum_{k=1}^{K} \log_2\left(1 + \gamma_k\right) \qquad \left[\frac{\text{bits/s}}{\text{Hz}}\right]. \tag{5.6}$$

However, due to collisions and the possibility of any MTD sending a packet in a given access slot, the previous equation cannot represent the real system ΣSE. A more realistic approach would consider just the access slot time in which a packet was successfully decoded instead. Hence, one can adapt the previous equation and obtain:

$$\Sigma\text{SE} = \sum_{k=1}^{K} \left(\frac{G_k T_{as}}{T_f}\right) \log_2\left(1 + \gamma_k\right) \qquad \left[\frac{\text{bits/s}}{\text{Hz}}\right]. \tag{5.7}$$

Notice that the throughput in packets/frame, denoted by G_f, has to fulfill the relation

$$G_f = \sum_{k=1}^{K} G_k, \qquad \text{with} \qquad G_k = \begin{cases} 1, & \text{packet of the } k\text{-th MTD is decoded} \\ 0, & \text{otherwise} \end{cases} \tag{5.8}$$

with G_f being the amount of successfully decoded packets in a single TDMA frame and $G_k \in (0, 1)$ a binary indicator for MTD k, which is 1 if the packet sent by MTD k was decoded and 0 otherwise. Figure 12 indicates the average ΣSE as a function of MTDs uplink power for SAP-RARAP and DAP-RARAP. Precisely, Figure 12a shows the results for SAP-RARAP, while Figures 12b and 12c brings the results for DAP-RARAP as a function of ρ_{L} and ρ_{H}, respectively. For the DAP-RARAP cases, MTDs located at the side of the communication cell which are not being varied is kept constant at $\rho_{\text{H}} = 10$mW and $\rho_{\text{L}} = 10$mW, respectively, according to Table 6.

For the SAP-RARAP, Figure 12a, we notice that for feasible values of MTDs uplink power, $\rho_{\text{MTD},k} \approx 10$ mW, it is possible to achieve a ΣSE of ≈ 3 bps/Hz, which is a low sum SE considering that $K = 10$ MTDs are being served. This happens because each MTD transmits just a single useful data packet as long as the replicas, when sent, are uplinked to create a temporal diversity, which causes redundancy. Due to the fact that each access slot consumes just a small fraction of the whole TDMA frame, the ΣSE is

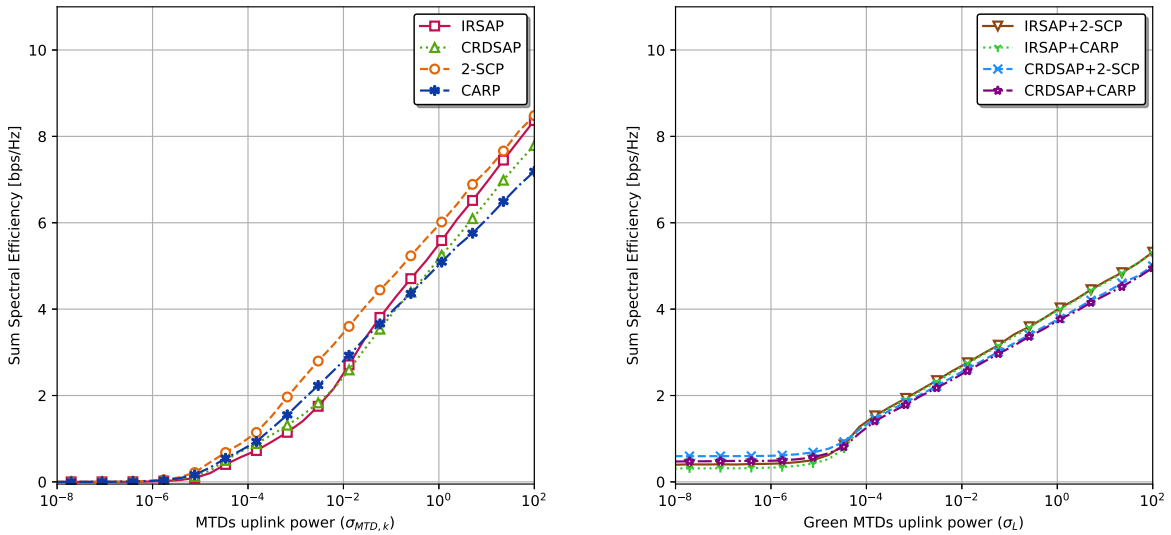

(a) SAP-RARAP

(b) DAP-RARAP (Green)

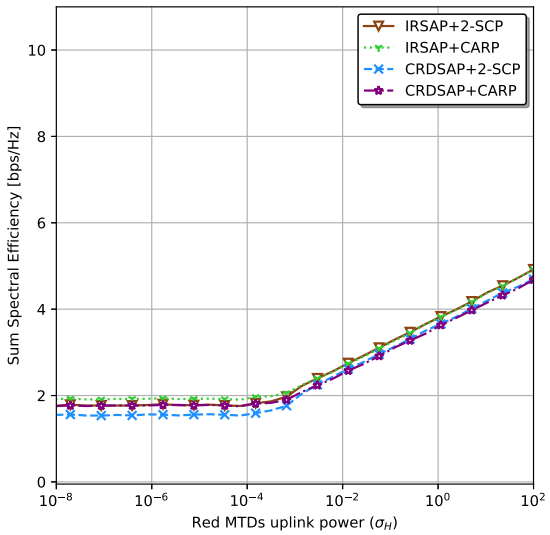

(c) DAP-RARAP (Red)

Figure 12 – Achievable sum spectral efficiency ΣSE of the studied protocols: (a) SAP-RARAP as a function of MTDs uplink power; (b) DAP-RARAP as a function of green area MTDs uplink power and (c) DAP-RARAP as a function of red area MTDs uplink power.

quite low. For the DAP-RARAP protocol, the same behavior is noted, with the addition that reducing the green-side MTDs' power can severely reduce the system ΣSE.

However, without increasing MTDs uplink power and the duration of the TDMA frame, it is still possible to increase ΣSE. The possible approaches are listed below:

- **Reduce Training Slots Duration:** By keeping the frame time T_f fixed, if the time spent with training is reduced, one can say that we would be able to increase the duration of the access time slots, T_{as}, augmenting the pre-log factor of equation (5.7), which would inevitably increase the ΣSE. However, one must be aware that in practical scenarios, the reduction of training access slots can cause some problems, especially with RIS synchronization, as long as the duration of each training slot, T_{ts}, must comprise the time required for the RIS adjust its predefined configurations within.

- **Reduce the Number of Slots S**: If we decrease the amount of the time slots, it would be possible to increase the duration of the remaining slots proportionally. However, the overall system throughput G *can be harmed* (and consequently the Σ**SE**), because the number of MTDs that can connect in a single TDMA frame can be reduced due to the lower number of RIS beams available through the TDMA frame (remember that the number of RIS beams configurations matches S). In summary, this approach is only suitable if $S \gg K$, because many slots might stays vacant during the access phase due to the lower number of MTDs contending for resources. Hence, this must be done carefully and seems to be a more delicate tradeoff than that proposed in the latest topic.

- **Integrate the SIC Receiver with NOMA**: This could increase the overall system throughput as the detection of two packets transmitted in the same slot was allowed. If a collision happened, if the received power of these packets are sufficiently different, *e.g., 3 dB*, the BS could separate these MTDs in the power domain, successfully decoding two packets from distinct MTDs. Considering the blockage presence and the variability of channel condition due to RIS phase shifts, is can be suitable to apply this approach.

5.5 Performance-Complexity of SAP-RARAP and DAP-RARAP Protocols

This section presents a comprehensive analysis on the numerical simulation results involving the main performance and complexity metrics, considering representative scenarios and parameter values. Hence, comparisons among DAP-RARAP and SAP-RARAP

are made and intermediate results are presented that are essential to a deeper understanding of the operation of the DAP-RARAP protocol.

Remark 1: *In order to make a fair comparison between both protocols, the SAP-RARAP must be adapted concerning the area where MTDs are positioned and the channel model used. Hence, although the term "SAP-RARAP" is used here, the reader must be warned that MTDs angular position are distributed in the range* $[0, \pi]$ *instead* $[0, \frac{\pi}{2}]$ *and the considered channel model was not the one presented in references [38, 28], but the channel model with the addition of the direct link between MTDs and AP, as presented in equations* (4.2) *to* (4.10)*. The other variables remained the same.*

Remark 2: *The values achieved for the presented performance metrics are averaged within each TDMA frame. However, recall that the TDMA frame of the SAP-RARAP protocol with policies IRSAP and CRDSAP are smaller due to the obsolescence of the DL training step, as already explained.*

5.5.1 Channel Achievable SNRs Under Different Channel Conditions

Before analyze the performance of both protocols, we present in this subsection the PDFs and CDFs of the achievable SNRs under different channel conditions. The channel behavior is essential for the studied RA protocols for two reasons. The first one is the fact that some policies and protocols leverage CSI to decide the time slots in whose data packets will be sent. Hence, for those protocols/policies that depend on CSI, it is expected a smaller performance degradation when worse channel conditions are experienced. The second reason is the SIC SNR threshold, γ_{TH}. For channel conditions where lower SNR values occur more frequently, the probability of packets received with an SNR under γ_{TH} increases. Hence, even if this packet is received in a singleton slot, it cannot be successfully decoded, harming the interference cancellation and degrading the performance.

Figures 13a and 13b shows the PDF and CDF of the received packets' SNRs, respectively. The CDF of the localization coefficients, computed by MTDs is also presented. Three channel conditions are adopted:

i) **nLoS**, with $\kappa_1 = \kappa_2 = \delta = 0$;

ii) **LoS**, with $\kappa_1 = \kappa_2 = \delta = 1 \times 10^{10}$;

iii) **Rician**, with $\kappa_1 = 9$; $\kappa_2 = 3/7$; and $\delta = 6/4$.

To compute the histograms presented here, we evaluate the SNRs of $K = 10^4$ MTDs uniformly distributed within the communication cell, considering a TDMA frame with $S = 20$ slots. Hence, in Figures 13a and 13b we have 20×10^4 SNR samples, and in Figure 13c the histograms are made with 10^4 samples. By observing Figure 13b, one can

note that the LoS curve is always equal or smaller than the Rician one, which is always equal or smaller than the nLoS scenario. Hence, the probability of the received SNR being equal to or smaller than any SNR value is always higher for nLoS, and always smaller for LoS scenarios. Rician fading channels are always between both cases, as expected.

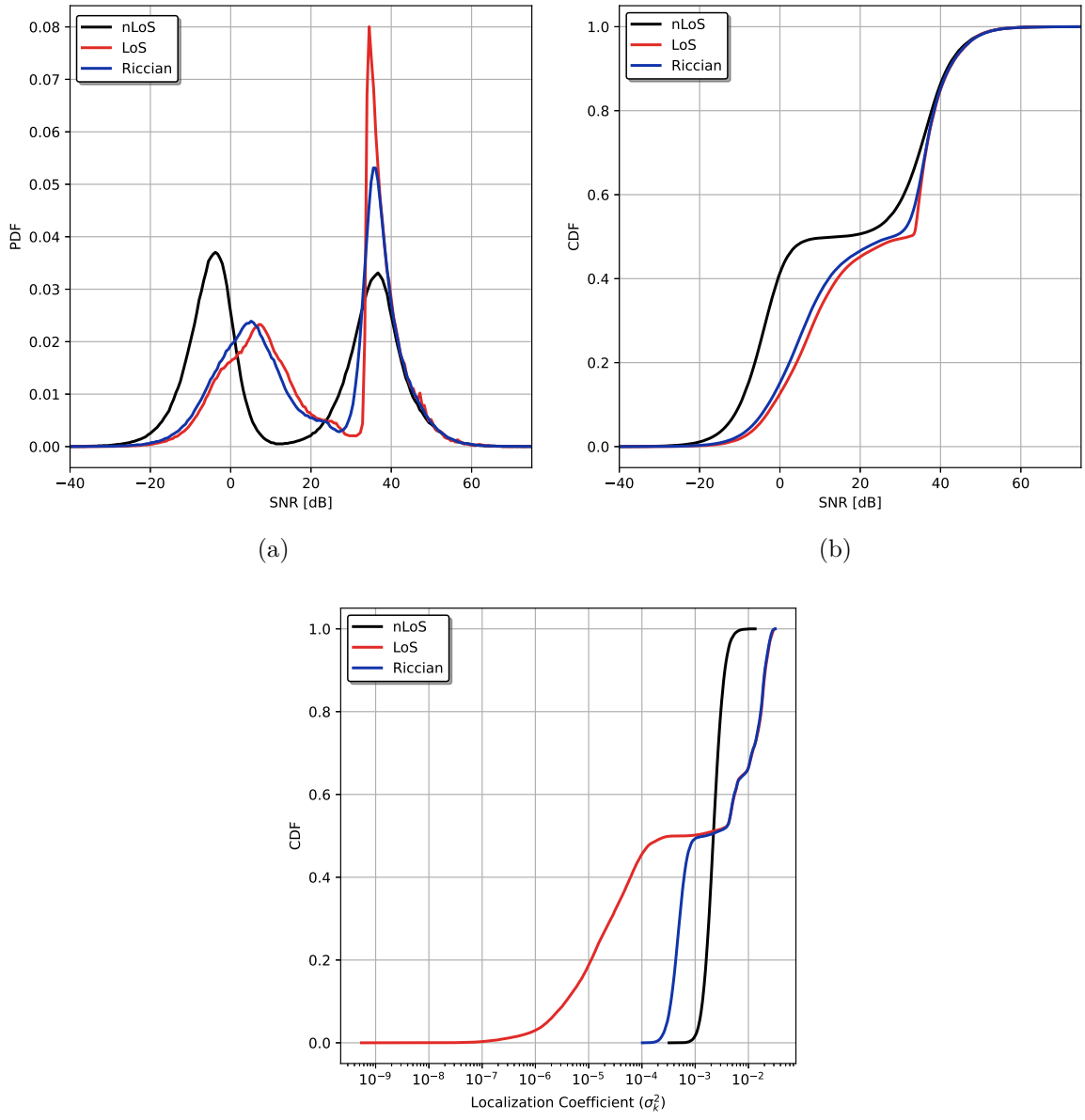

Figure 13 – (a) SNR's PDFs; (b) SNR's CDFs, (c) CDF of the localization coefficients σ_k^2 for three different channel conditions.

Mathematically, denoting the CDFs of the studied scenarios as $\mathrm{F}_{\mathrm{LOS}}(\gamma)$, $\mathrm{F}_{\mathrm{RICIAN}}(\gamma)$ and $\mathrm{F}_{\mathrm{NLOS}}(\gamma)$, we have:

$$\mathrm{F}_{\mathrm{LOS}}(\gamma_x) \leq \mathrm{F}_{\mathrm{RICIAN}}(\gamma_x) \leq \mathrm{F}_{\mathrm{NLOS}}(\gamma_x), \quad \forall\ \gamma_x \in \mathbb{R}. \tag{5.9}$$

When a higher amount of data packets are received under an arbitrary value of SNR, *e.g.* $\gamma_x = \gamma_{\mathrm{TH}}$, the probability of unsuccessful detection increases. This happens because if

some of these packets occur in singleton time slots, the transmitted information cannot be recovered by the SIC algorithm due to *unresolved collisions*, harming not only the decoding of this MTD's data packets but eventually other MTD's data packets that could be successfully decoded after some SIC iterations.

5.5.1.1 Optimal Localization Threshold

The definition of the optimal localization threshold σ^2_{TH} aims to maximize the number of MTDs that correctly infer the cell region they are. In other words, according to the studied scenario depicted in Figure 2, an MTD positioned in the green area must identify that he does not need RIS assistance, while an MTD located in the red area must; this is made by comparing the estimated localization coefficient σ^2_k with the pre-established threshold. Hence, in the optimal case, one can establish σ^2_{TH} as the value of σ^2_x that results in $F(\sigma^2_x) = 0.5$[4]. By observing Figure 13c, we notice that when LoS links are included in the channel model, *i.e.,* for Rician and LoS channels, the σ^2_k CDF results in a salient point when $F(\sigma^2_x) \approx 0.5$, which indicates that half of MTDs presented a estimated localization threshold lower than σ^2_x and the other half have their coefficients higher than σ^2_x. The first group of MTDs, which estimated $\sigma^2_k < \sigma^2_x$, is the group that does not present high power variations among S slots; and the second group is the one that experiences the RIS-induced diversity among the S training slots, which results in higher values of σ^2_k. We see in Figure 13c that, in practice, when the channel is LoS, there is a vast range of values that can be adopted for σ^2_{TH}. This range is also noted for Rician channels but is much stricter than observed in the pure LoS case. Under purely nLoS channel, due to the absence of the LoS reflected link, an optimized σ^2_{TH} is unpractical.

To exemplify that, we present in Figure 14 the percentage of miss classified MTDs as a function of the localization threshold for different scenarios. A miss classified MTD is defined as an MTD that is physically located in the green area but obtained $\sigma^2_k > \sigma^2_{\text{TH}}$ or an MTD that is located in the red area that estimated $\sigma^2_k \leq \sigma^2_{\text{TH}}$. It is possible to see that, for each scenario presented in Figure 14, we have a specific value of σ^2_k that minimizes the probability of miss classifying MTDs. By varying some system parameters, the value of σ^2_{TH} that minimizes this probability changes, highlighting the fact that this parameter must be carefully designed in order to effectively minimize the number of miss classified MTDs for each case. In real scenarios, before starting the system operation, one must reserve some TDMA frames to identify the optimal localization threshold.

This step consists in positioning MTDs at know cell locations and letting them repeatedly estimate their σ^2_k for a given value of σ^2_{TH}, *e.g.,* $\sigma^2_{\text{TH}} = 1 \times 10^{-4}$. At each TDMA frame, during the uplink phase, MTDs sends the estimated σ^2_k values instead of

[4] If the MTDs distribution within the communication cell and/or the blockage was positioned in a region that does not divide the communication cell into symmetric areas, the optimal localization threshold would not be obtained at $F(\sigma^2_x) = 0.5$.

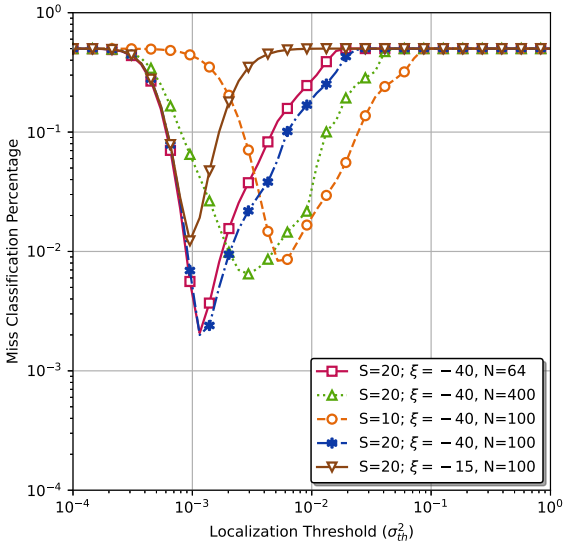

Figure 14 – Percentage of miss classified MTDs as a function of the localization threshold σ^2_{TH}.

its information data within each data packet and the BS performs the SIC algorithm normally in order to receive its measurements and store them in a memory. The ID of each MTD is also send, and it is assumed that the BS knows the position of each MTD. Given the received values of σ^2_k and knowing where each MTD is positioned, the BS can count how many MTDs have been miss classified for that given σ^2_{TH} value. The process is repeated until a vast number of σ^2_{TH} values were tested, resulting in curves like those presented in Figure 14. Finally, the BS defines the *optimal localization threshold* as the σ^2_{TH} that *minimizes* the miss classification percentage of the evaluated scenario, send this optimal value for MTDs and the protocol operation begins.

Figure 15 shows the variation in the optimal localization threshold σ^2_{TH} as a function of three system parameters. Specifically, the number of RIS elements N is varied in Figure 15a, while Figure 15b unveils how this variation occurs as a function of the number of time slots S. Finally, the optimal localization threshold as a function of the blockage attenuation ξ is analyzed in Figure 15c. When DAP-RARAP performance is evaluated in the next subsections, we discuss how the proper selection of σ^2_{TH} impacts the system performance. These variations revealed in Figure 15 occur because by varying specific parameters, the CDFs shown in Figure 13c changes, which requires further adjustments in the localization thresholds.

5.5.2 SAP-RARAP and DAP-RARAP Performances as a Function of the Number of Contending MTDs

Figures of merit for the SAP-RARAP and DAP-RARAP RA protocols, as a function of the number of contending MTDs, are indicated in Figure 16. The performance of the SAP-RARAP is arranged in the plots in the first column, the DAP-RARAP in the

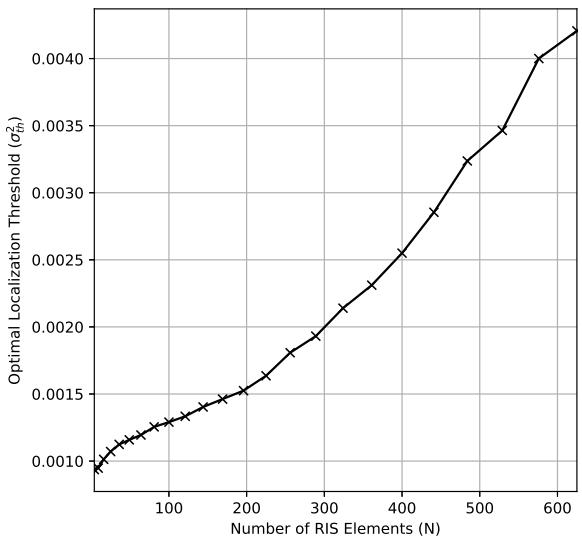

(a) # RIS Elements ($S = 20, \xi = -40$ dB)

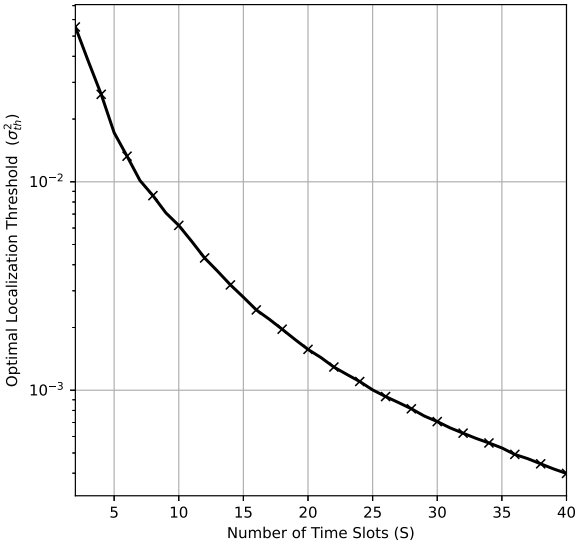

(b) # Time Slots ($N = 100, \xi = -40$ dB)

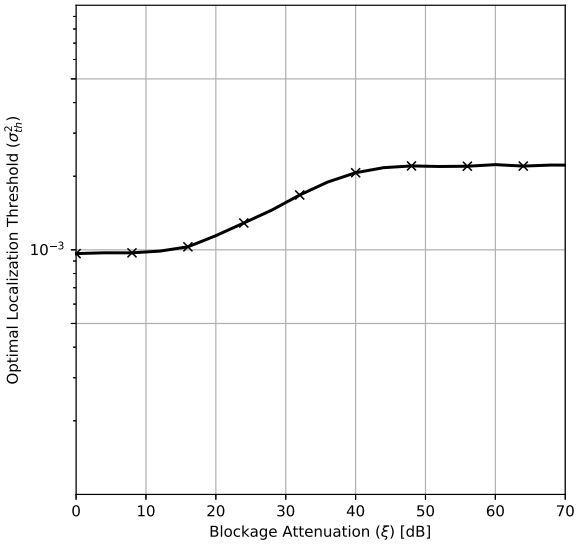

(c) Blockage Attenuation ($S = 20, N = 100$)

Figure 15 – Optimal localization thresholds as a function of (a) number of RIS elements (N); (b) number of time slots (S); and (c) blockage attenuation (ξ).

middle, and the last column shows a comparison between both approaches. The rows of the set of plots show the throughput, total EE, and MTDs' EE performance, respectively. The adopted simulation parameters are listed in Table 3.

By observing the results achieved with SAP-RARAP, Figure 16a, one can see that CSI-based access policies were able to attain the best performance. In addition, we notice that the maximum G value for 2-SCP was achieved with $K = 14$ and CARP with $K = 16$, while IRSAP peak was noted at $K = 10$ and CRDSAP at $K = 12$. This shows that access policies that use CSI[5] are able not only to achieve a higher throughput but also handle

[5] See Table 1.

a higher number of MTDs simultaneously. The suboptimal performance of IRSAP and CRDSAP shows that performing the uplink data detection blindly causes problems in the interference cancellation process: as long as MTDs at the red side of the communication cell experience SNRs lower than $\gamma_{\text{TH}} = 5$ dB in many time slots – see Figure 8 – such MTDs, eventually, use these slots to perform uplink detection/decoding. As a result, many packets sent by these do not fulfill the γ_{TH} requirement, impeding the recursive interference cancellation process. On the other hand, when DAP-RARAP is adopted, as shown in Figure 16b, the maximum throughput of IRSAP+2-SCP, CRDSAP+2-SCP and CRDSAP+CARP happens at $K = 14$, while IRSAP+CARP throughput achieved its peak at $K = 15$. Furthermore, the peak throughput of DAP-RARAP was approximately 1 k packets/s higher than the peak of SAP-RARAP, which highlights the efficiency of the double-policy method. Curiously, in DAP-RARAP, the access policies with IRSAP achieved the best peak performance, while in SAP-RARAP the IRSAP was the worst choice for all K values analyzed.

This behavior observed with IRSAP reinforces that MTDs from the red area of the cell cannot perform the uplink of data packets blindly. Conversely, when we evaluate the overall system EE of SAP-RARAP, the IRSAP and CRDSAP policies reveal a remarkable performance compared to access policies leveraged by CSI. This behavior can be explained by the fact that IRSAP and CRDSAP do not require training, which allows the RF power spent by the BS to be set to zero for this task, significantly reducing the total system power. Then, the EE of SAP-RARAP with this access policies is very enhanced. By observing Figures 16e and 16f, we conclude that DAP-RARAP is not able to outperform SAP-RARAP at any K value observed because the training phase of DAP-RARAP cannot be discarded, augmenting the power spent by the BS to send training pilots during the training phase.

However, removing the BS and RIS power from the EE metric, *i.e.*, considering just the power spent by MTDs, one can notice a remarkable EE gain when DAP-RARAP is used. Figure 16g shows the MTDs' EE when SAP-RARAP is adopted, while Figure 16h shows the EE results for DAP-RARAP. Clearly, in Figure 16i, one can see that the MTDs' EE can be significantly increased by adopting the double-policy approach because MTDs are able to adjust its uplink power according to the estimated cell region they are. As a result, MTDs from the green area can reduce the amount of power used during data transmission. This is paramount for mMTC scenarios, as long as it extends the battery lifetime of IoT devices – especially those from the green area –, avoiding the need for frequent human maintenance of these devices. Also, comparing the performance of both random access methods w.r.t. the MTDs' EE metric, as discussed in Figure 16i, one can observe that at $K = 14$ MTDs DAP-RARAP presented a performance almost as twice as good as the single-policy approach.

5.5.3 SAP-RARAP and DAP-RARAP Performances as a Function of MTDs Uplink Power

In this subsection, we present simulation results regarding the performance of the SAP and DAP random access protocols as a function of MTDs UL power. Because in DAP-RARAP we have two available power levels, ρ_{H} and ρ_{L}, we will begin our analysis by presenting the throughput, EE and MTDs EE surface plots of DAP-RARAP as a function

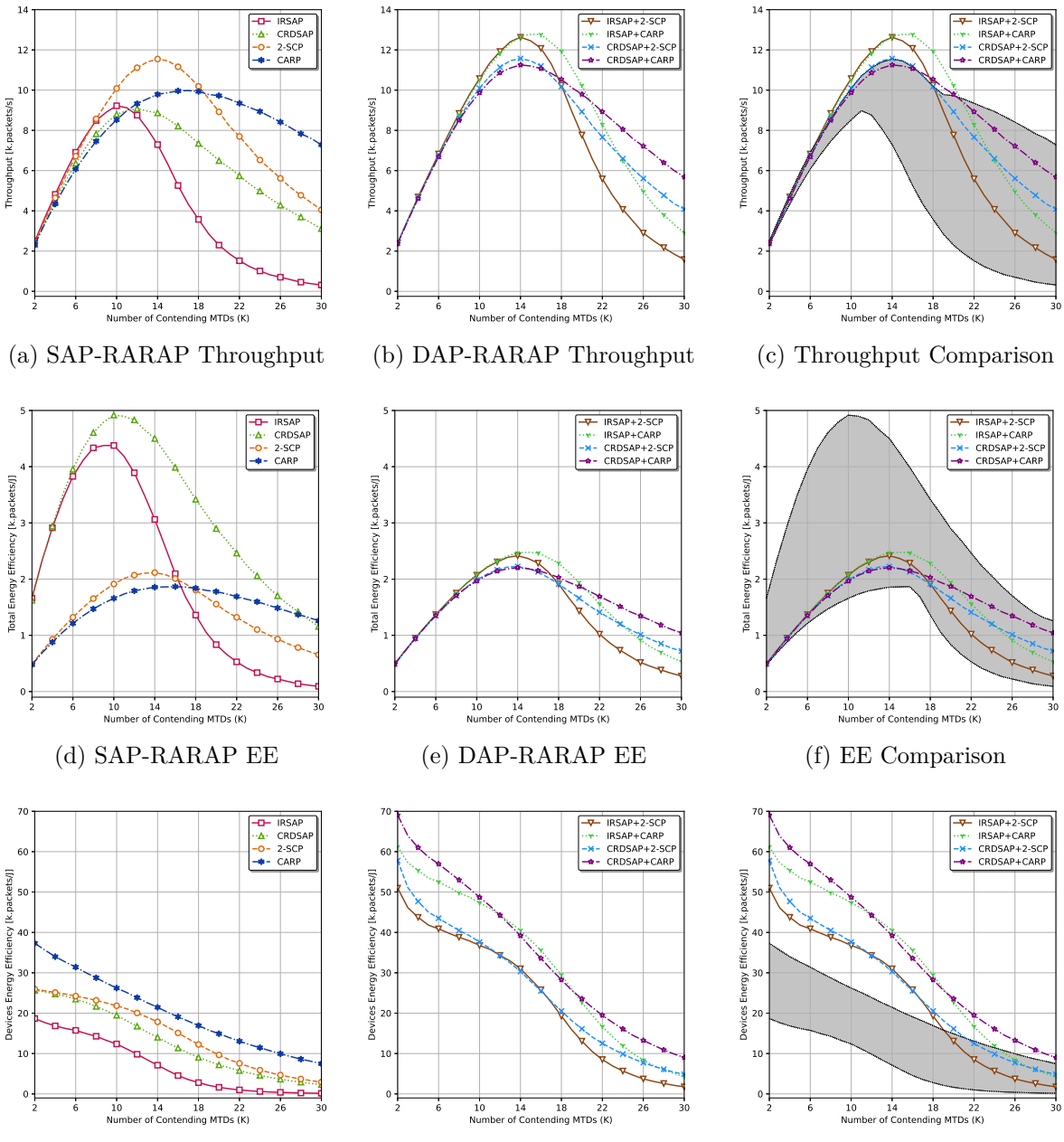

(a) SAP-RARAP Throughput (b) DAP-RARAP Throughput (c) Throughput Comparison

(d) SAP-RARAP EE (e) DAP-RARAP EE (f) EE Comparison

(g) SAP-RARAP MTDs EE (h) DAP-RARAP MTDs EE (i) MTDs EE Comparison

Figure 16 – SAP-RARAP and DAP-RARAP performances as a function of the number of contending MTDs. The third column contains the DAP-RARAP lines plotted, and the shaded area represents the range between maximum and minimum values that can be achieved with SAP-RARAP.

of ρ_{H} and ρ_{L}. For those cases, we summarize the optimal points of each performance metric and policy combinations in Table 7. Next, we present the simulation results regarding SAP-RARAP, and a discussion comparing both approaches is provided.

DAP-RARAP Throughput Performance: In Figure 17, we show the throughput surface plots of DAP-RARAP as a function of ρ_{H} and ρ_{L} for all possible combinations of access policies. For this metric, the MTDs powers summarized in Table 7 is the minimum uplink power required to attain *at least* 95 % of the maximum throughput. As expected, for all cases, we notice that when MTDs increase their uplink power, G also increases until reaching its plateau. Specifically, the throughput starts to increase significantly along the ρ_{L} axis at $\rho_{\text{L}} \approx -28$ dBm, while along the ρ_{H} axis these variations began to be noted at $\rho_{\text{L}} \approx -15$ dBm. Recall that MTDs from the red area are harmed by the blockage attenuation; then, they must select the higher power level to perform the uplink of its data packets. Hence, at low power levels, their signals are not able to overcome the blockage attenuation, harming G, which explains why the throughput variations occurs at higher power values in the ρ_{H} axis. Furthermore, by observing the surface plots, we notice that the combinations of access policies that is able to provide the maximum G is IRSAP+CARP, which result is provided in Figure 17b. A similar throughput can be achieved with IRSAP+2-SCP, which is shown in Figure 17a. On the other hand, combinations of access policies that uses CRDSAP presented a smaller throughput when compared to combinations that uses IRSAP, as can be viewed in Figures 17c and 17d. Because of that, one can say that IRSAP can better overcome the scenario challenges with respect to CRDSAP, providing better throughput. In addition, it is important to say that despite the fact that the throughput increases with ρ_{L} and ρ_{H}, selecting higher power levels severely harm the system and the MTDs energy efficiency, respectively, η_{T} and η_{MTD} performances, as will be shown in the following.

DAP-RARAP Total EE Performance: Figure 18 highlights that we shall not adopt extremely high power levels just to increase the overall throughput G. Indeed, allowing MTDs to uplink at higher power allows the decodification of more packets, increasing the system throughput; however, IoT devices shall not adopt extremely high power levels to transmit its data, because it is unpractical and would rapidly consumes its battery budget. Hence, at extremely high throughput values the system EE is unpracticable because as we can see, at high throughput regions observed in Figure 17, the total system EE tends to zero due to the extremely high amount of power expended by MTDs, reducing not only η_{T} but also the lifetime of their batteries. For all access policies, the peak EE performance is projected in all three axis by in order to facilitate the identification of these points. These projections are depicted by black dotted lines. We first notice that IRSAP+2-SCP (Figure 18a) and IRSAP+CARP (Figure 18b) are able to achieve similar values of optimal EE, around $\eta_{\text{T}} \approx 2.50$ k.packets/J. However, for IRSAP+2-SCP this peak can be achieved at $\rho_{\text{H}} \approx 8.6$ dBm, while for IRSAP+CARP it is necessary $\rho_{\text{H}} \approx$ 11.2 dBm to

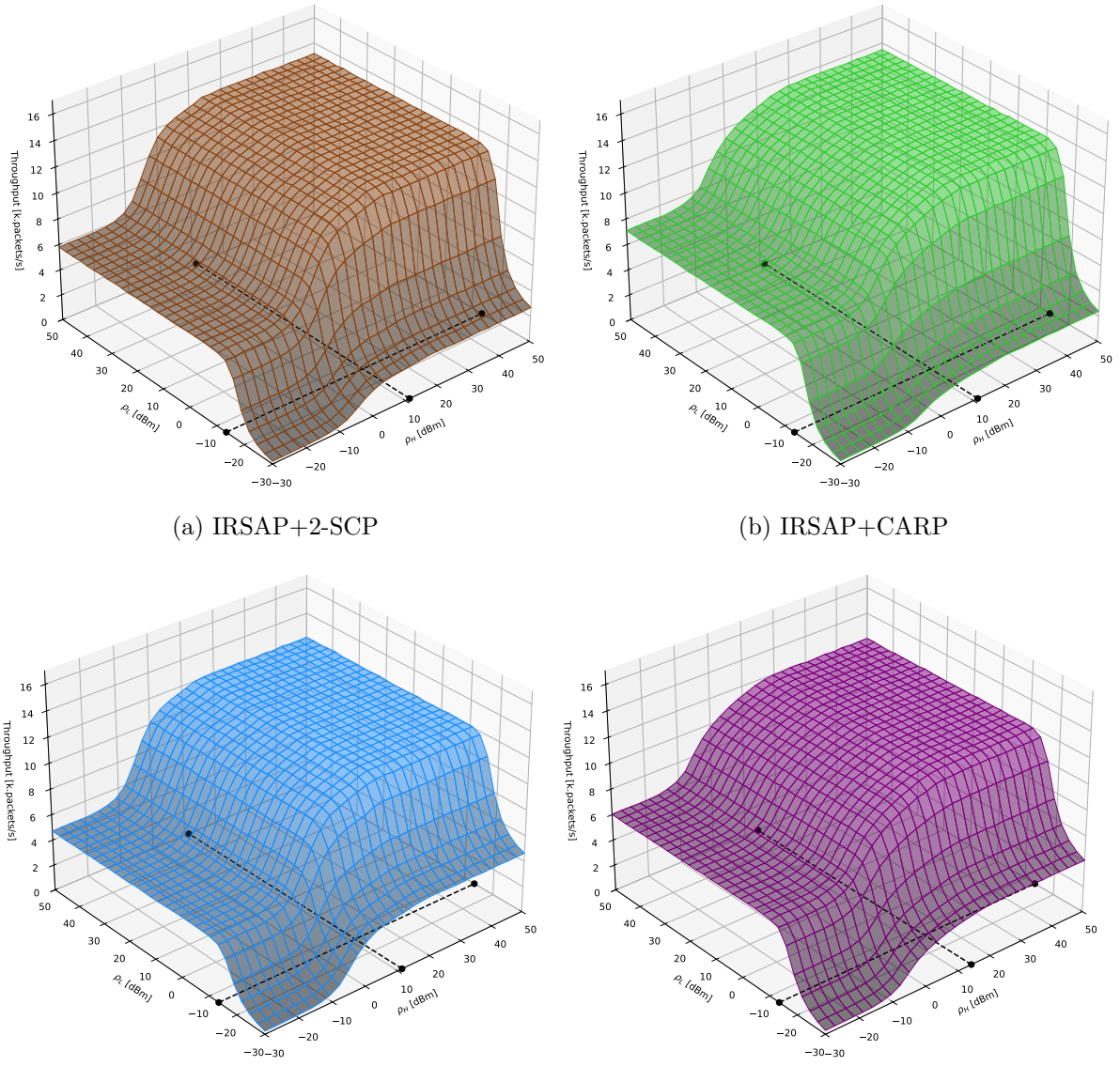

(a) IRSAP+2-SCP

(b) IRSAP+CARP

(c) CRDSAP+2-SCP

(d) CRDSAP+CARP

Figure 17 – Throughput of DAP-RARAP protocol as a function of ρ_H and ρ_L for all studied combinations of access policies.

attain it. CRDSAP+2-SCP and CRDSAP+CARP combinations, shown in Figures 18c and 18d, respectively, resulted in a suboptimal EE value, achieving the maximum EE of $\eta_T \approx 2.25$ k.packets/J. The uplink power levels observed in these optimal points shown that EE can be enhanced by selecting an operation point where $\rho_H > \rho_L$.

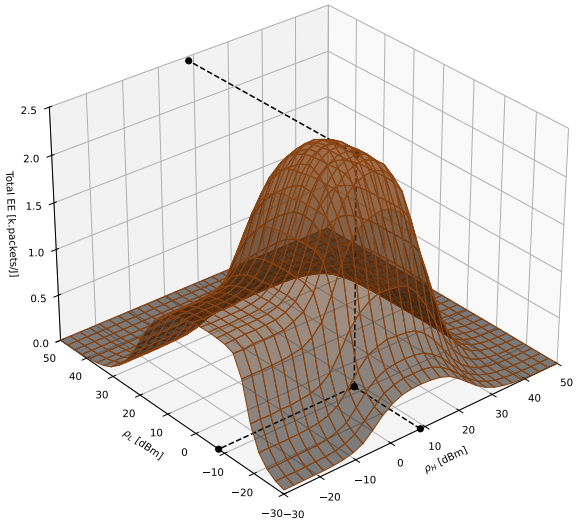

(a) IRSAP+2-SCP

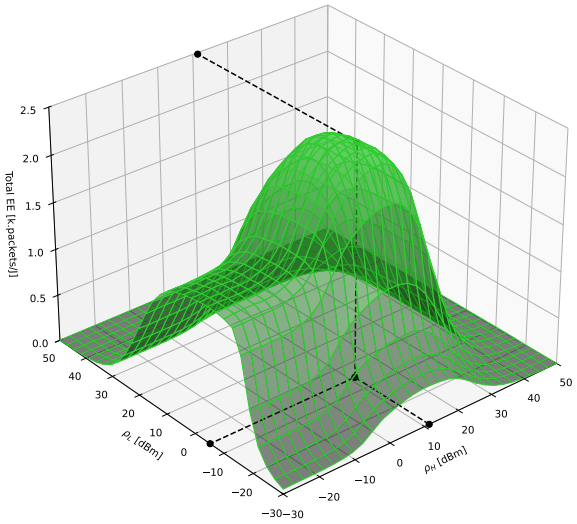

(b) IRSAP+CARP

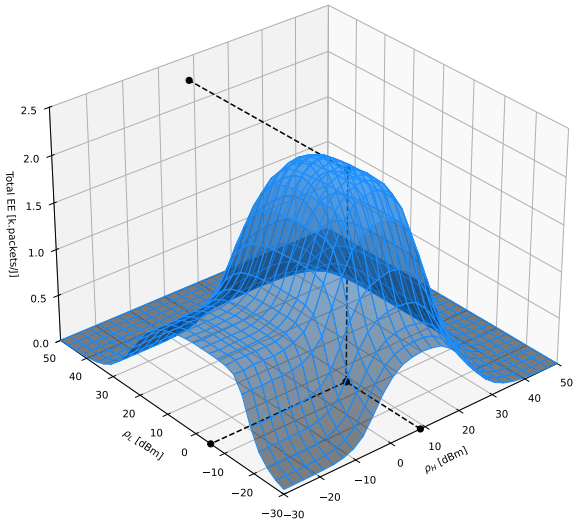

(c) CRDSAP+2-SCP

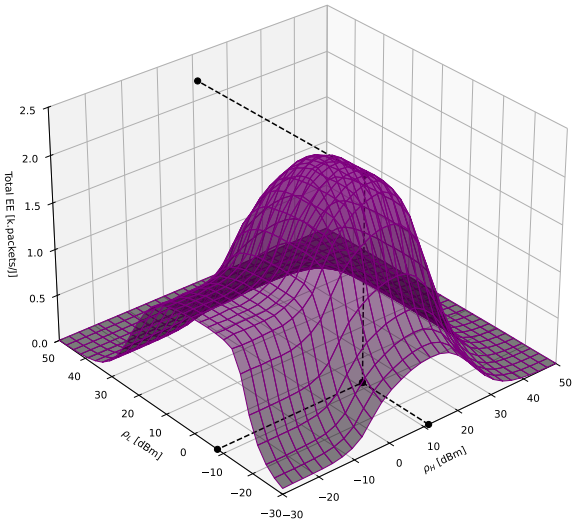

(d) CRDSAP+CARP

Figure 18 – Total EE of DAP-RARAP protocol as a function of ρ_{H} and ρ_{L} for all studied combinations of access policies.

DAP-RARAP MTDs EE Performance: The MTDs EE for DAP-RARAP as a function of MTDs uplink power are shown in Figure 19. For all combinations of access policies, it is possible to see that the optimal η_{MTDS} value also occurs at points where $\rho_{\mathrm{H}} > \rho_{\mathrm{L}}$. Furthermore, we notice that the optimal η_{MTDS} significantly varies depending on the combination of access policies adopted. Specifically, IRSAP+CARP achieved the best performance, reaching an EE of over 100 k.packets/J. Besides, IRSAP+2-SCP resulted in the second best performance, with $\eta_{\mathrm{MTDS}} \approx$ 93 k.packets/J. CRDSAP+CARP combination resulted in the third best performance with $\rho_{\mathrm{MTDS}} \approx$ 90 k.packets/J; and finally, the combination CRDSAP+2-SCP was able to reach only $\eta_{\mathrm{MTDS}} \approx$ 87 k.packets/J, being the worst choice w.r.t. MTDs EE. These results can be observed in Figures 19b, 19a, 19d and

19c, respectively.

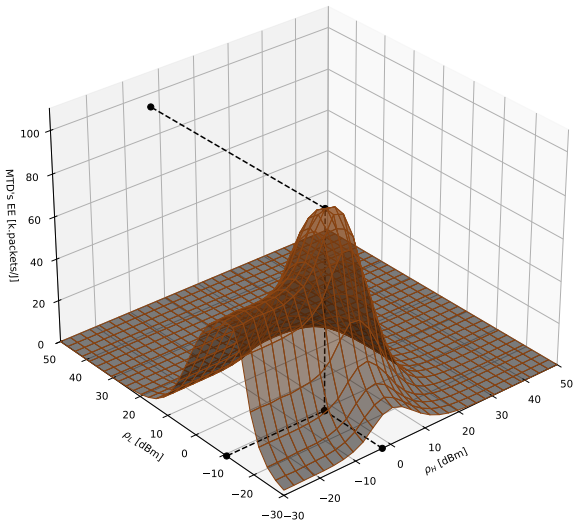

(a) IRSAP+2-SCP

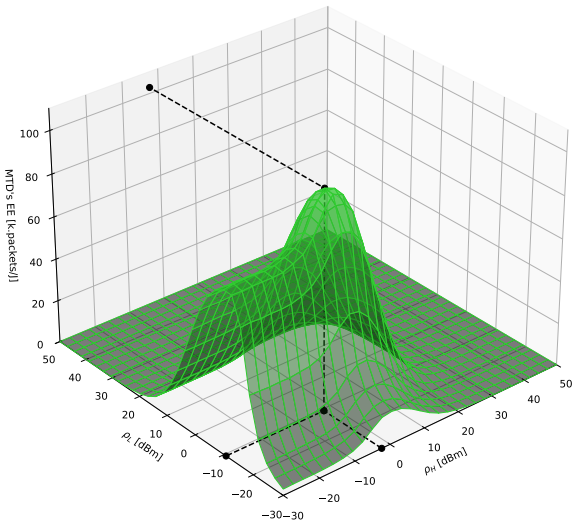

(b) IRSAP+CARP

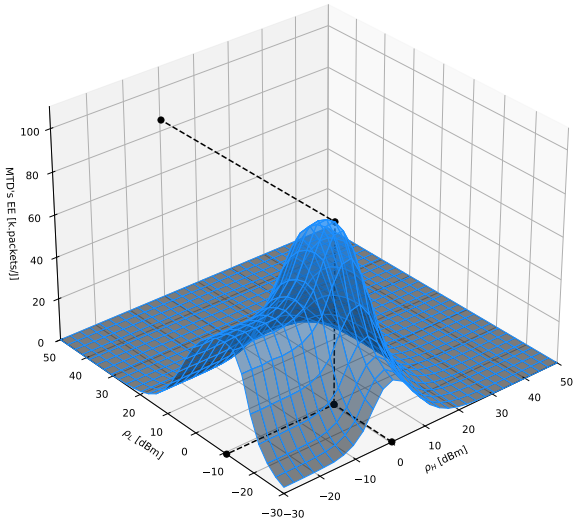

(c) CRDSAP+2-SCP

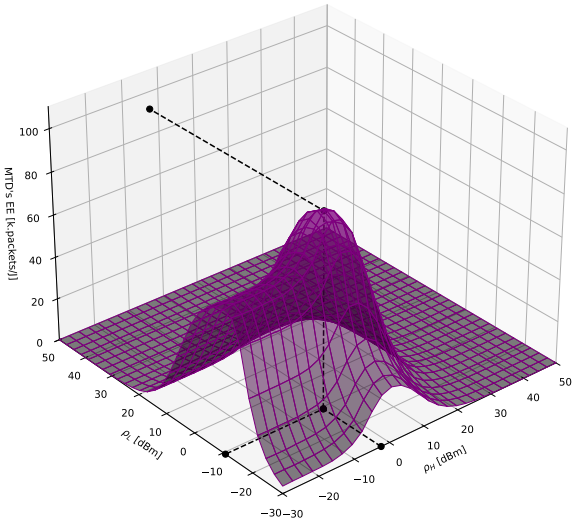

(d) CRDSAP+CARP

Figure 19 – Total MTD's EE of DAP-RARAP protocol as a function of ρ_{H} and ρ_{L} for all studied combinations of access policies.

The optimum points observed in Figures 17, 18 and 19 are summarized in Table 7. It is possible to see that the uplink power levels that maximize the MTDs' EE are lower than the uplink power levels that maximize the overall system EE. At higher power levels, the throughput G will be maximized; however, expending so much power with uplink severely harms the MTDs' EE.

Metric	**Policies**	**Subfigure**	**Maximum**	**MTDs Optimal Powers**	
				ρ_{L}	ρ_{H}
Throughput [k.packets/s]	IRSAP+2-SCP	17a	13.24	-13.45 dBm*	11.38 dBm*
	IRSAP+CARP	17b	13.54	-13.45 dBm*	11.38 dBm*
	CRDSAP+2-SCP	17c	12.15	-13.45 dBm*	11.38 dBm*
	CRDSAP+CARP	17d	12.05	-13.45 dBm*	14.34 dBm*
EE [k.packets/J]	IRSAP+2-SCP	18a	2.45	-7.93 dBm	8.62 dBm
	IRSAP+CARP	18b	2.48	-5.17 dBm	11.38 dBm
	CRDSAP+2-SCP	18c	2.25	-5.17 dBm	8.62 dBm
	CRDSAP+CARP	18d	2.20	-7.93 dBm	11.38 dBm
MTDs EE [k.packets/J]	IRSAP+2-SCP	19a	93.72	-10.69 dBm	-2.41 dBm
	IRSAP+CARP	19b	102.73	-10.69 dBm	-2.41 dBm
	CRDSAP+2-SCP	19c	85.06	-10.69 dBm	0.34 dBm
	CRDSAP+CARP	19d	91.87	-10.69 dBm	-2.41 dBm

*Minimal powers required to achieve *at least* 95 % of the maximum throughput value.

Table 7 – Optimal points achieved with simulation results.

SAP-RARAP Performances: Simulation results presenting the SAP-RARAP performance metrics are shown in Figure 20. Notice that, now, we have 2D plots because MTDs can perform uplink with a unique power level. In Figure 20a, one can notice that the access policy that was able to achieve the best peak throughput was IRSAP, followed by CRDSAP, 2-SCP and CARP, respectively. However, the maximum throughput for IRSAP and CRDSAP can be attained only under the adoption of an extremely high uplink power by MTDs, which makes these approaches unfeasible for mMTC scenarios. 2-SCP and CARP achieved a lower peak throughput when compared with non-CSI-aided access policies but could perform their respective peak performance using less power, which is essential for the studied protocols. It is also possible to notice a salience around $\rho_{\text{MTD}} \approx -12$ dBm for all access policies, which indicates the power level required for half of the communication cell – specifically the green side –surpasses the minimum SIC SNR threshold. At higher power levels, the throughput augments because MTDs from the red area can progressively achieve the minimum SIC requirement, causing their packets to be decoded and also facilitating the SIC process due to the resolution of more singletons.

The total system EE, shown in Figure 20b, can be enhanced when non-CSI-aided policies are adopted. Specifically, CRDSAP presented the best peak performance, followed by IRSAP, 2-SCP, and CARP. The fact that CRDSAP outperformed IRSAP in that region is mainly related to the achievable throughput. The throughput of CRDSAP is

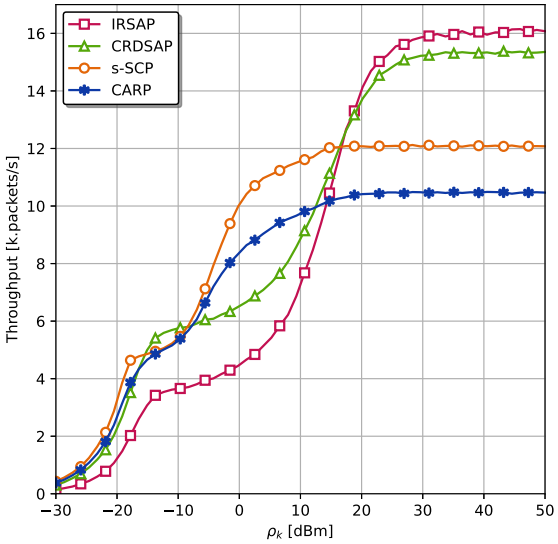

(a) SAP Throughput

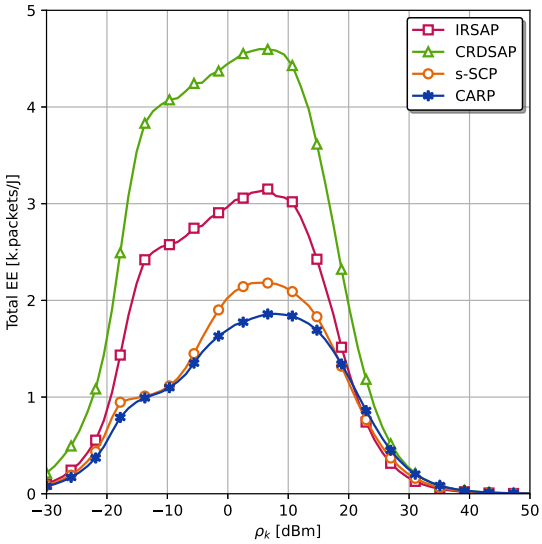

(b) SAP Total EE

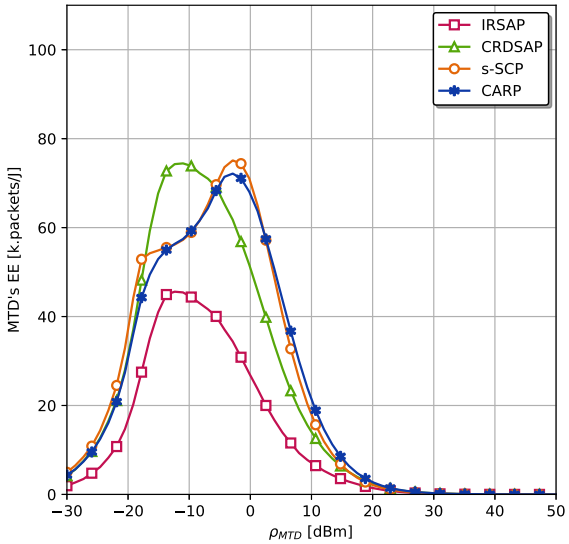

(c) SAP MTDs EE

Figure 20 – (a) Throughput (b) Total EE and (c) MTDs EE performances for SAP-RARAP as a function of ρ_{MTD} [dBm].

higher than IRSAP for $\rho_{\text{MTD}} < 17$ dBm (see Figure 20), which enhances the CRDSAP's total EE. We also have to emphasize that MTDs send an average number of packets lower than IRSAP in CRDSAP, contributing to the CRDSAP MTDs' EE. We notice that the average number of replicas impacts the system EE at $\rho_{\text{MTD}} \geq 17$, where even with a higher throughput performance, IRSAP is surpassed by CRDSAP due to the higher amount of replicas sent by each MTD. However, because the BS and RIS power consumption is much higher than the expenditure by the MTDs, this should be much more prominent at the MTDs' EE metric.

Analyzing the MTDs' EE, shown in Figure 20, one can notice that for approx-

imately $\rho_{\text{MTD}} > -5$ dBm RIS-aided access policies provided better performance when compared to IRSAP and CRDSAP. This result is also a consequence of the throughput curves: as we can observe in Figure 20a, for approximately $-2 < \rho_{\text{MTD}} < 20$ dBm the policies that use CSI outperforms the non-CSI-aided ones, and this higher throughput contributes to the overall MTDs' EE observed in Figure 20c. However, we also notice that the average number of packets sent by MTDs can significantly affects the devices' EE. By comparing IRSAP and CRDSAP, we notice that CRDSAP presented a higher MTD EE due to the fewer replicas sent at each frame. This result is even more apparent when we observe the 2-SCP and CARP curves: the average number of packets sent by CARP is lower than 2-SCP, which explains the fact that CARP presented a very competitive MTDs' EE when compared to 2-SCP even not being able to outperform 2-SCP throughput at any ρ_{MTD} studied.

5.5.4 SAP-RARAP and DAP-RARAP Performances as a Function of the Number of RIS Elements

SAP-RARAP and DAP-RARAP performances as a function of N are analyzed in this subsection. The obtained simulation results are depicted in Figure 21. The plots are organized as in previous subsections, with SAP-RARAP performances in the first column, DAP-RARAP performances in the second one, and the last column comparing both approaches. The throughput, total system EE, and MTDs EE are shown in the first, second, and third rows of the figure, respectively.

Parameter	**Value**
Number of MTDs	$K = 14$
Number of RIS Elements	$N \in (4, 625)$

Table 8 – Adopted simulation parameter values that overrides those from Table 3 in the simulation shown in Figure 21.

Concerning the throughput metric, we notice in Figure 21a that policies that leverages CSI (CARP and s-SCP) can achieve their maximum throughput with less RIS elements, around $N \approx 256$. On the contrary, when policies that do not need CSI are employed, it is possible to note that the maximum throughput plateau cannot be achieved even with $N = 625$ elements. Hence, when CSI is available, MTDs can effectively explore the spatiotemporal diversity imposed by an RIS with just ≈ 256 elements. On the other hand, if CSI is not available, the performance degradation of IRSAP and CRDSAP can be minimized by deploying RIS' with more elements, enhancing the channel quality of the MTDs. However, due to financial costs, smaller RIS' are preferable. By combining two access policies and employing DAP-RARAP, Figure 21b, we note a slight increase in the

overall throughput, resulting in almost 13 k packets/s, a gain of ≈ 1 k packets/s (≈ 8.3% gain) when compared with SAP-RARAP's peak throughput[6].

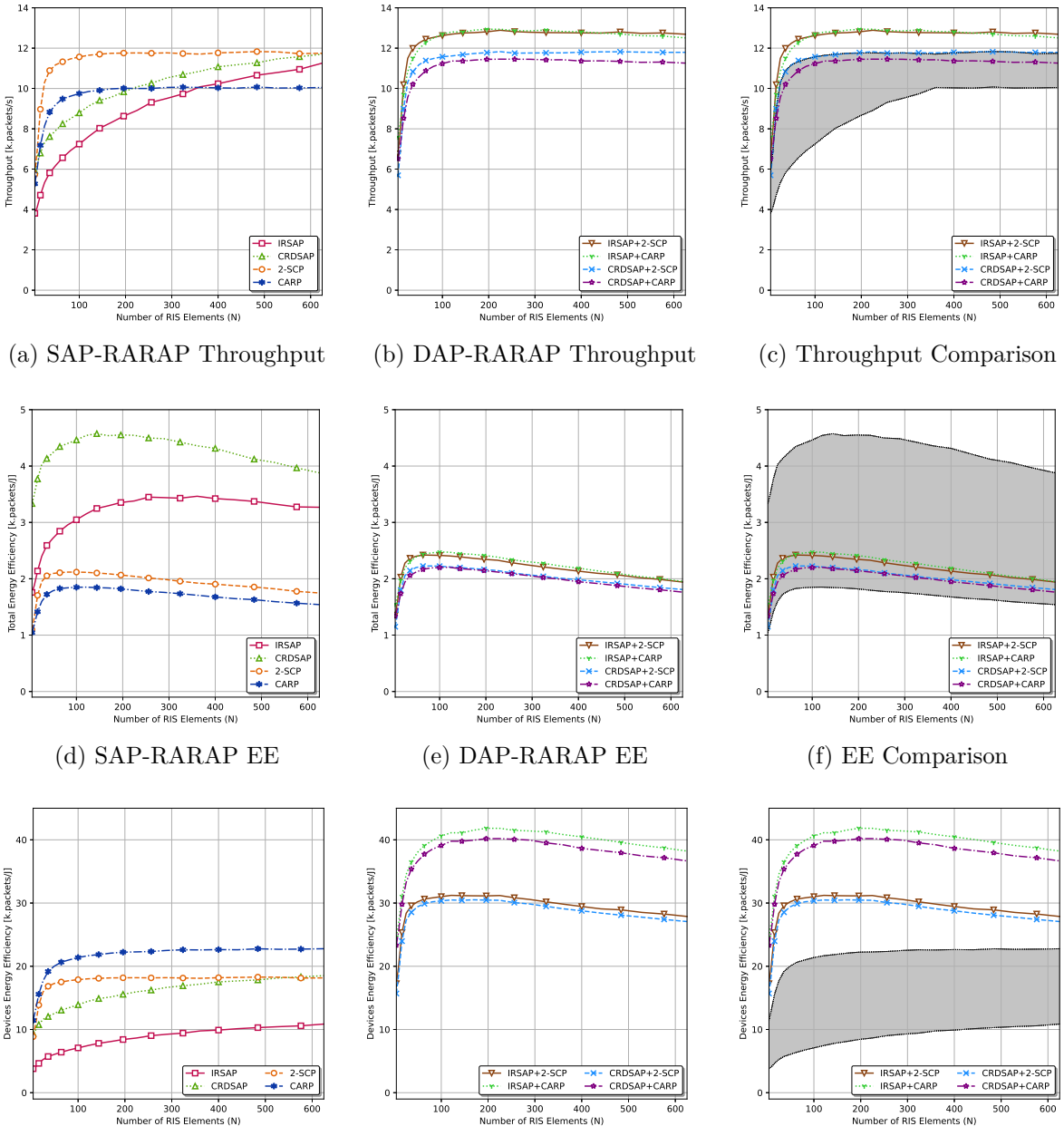

(a) SAP-RARAP Throughput (b) DAP-RARAP Throughput (c) Throughput Comparison

(d) SAP-RARAP EE (e) DAP-RARAP EE (f) EE Comparison

(g) SAP-RARAP MTDs EE (h) DAP-RARAP MTDs EE (i) MTDs EE Comparison

Figure 21 – SAP-RARAP and DAP-RARAP performances as a function of the number of RIS elements (N). The third column contains the DAP-RARAP lines plotted, and the shaded area represents the range between maximum and minimum values that can be achieved with SAP-RARAP.

In addition, the minimum throughput performance of DAP-RARAP – which is obtained with CRDSAP+CARP for the majority of N values presented – outperforms the minimum performance of SAP-RARAP, which is observed when IRSAP is used for

[6] Such gain of 1 k packets/s was already noted in Subsection 5.5.2

all N values presented, showing the double-policy approach efficiency. As was already discussed, in SAP-RARAP, if MTDs use CRDSAP or IRSAP from the red area, a higher number of unresolved singletons occurs and, consequently, a higher number of collisions, which significantly degrades the performance of this policy with SAP-RARAP. However, by deploying larger RIS', one can enhance these MTDs channel qualities, which explains the increasing throughput of IRSAP and CRDSAP curves in Figure 21a. Despite that, inducing MTDs from the red area to select a RIS-aided policy seems to be a much more convenient approach instead of deploying a larger RIS, as it would result in a higher throughput with a reduced implementation cost. The comparison of DAP-RARAP and SAP-RARAP throughput performances can be viewed in Figure 21c.

For the total EE metric, Figure 21d reveals that for SAP-RARAP, the s-SCP and CARP present a lower EE than those provided when access policies that do not use CSI are applied due to the extra amount of power expended at the BS with training pilots downlink. In addition, the optimal total EE for SAP-RARAP occurs at different N values, depending on the access policy: for CRDSAP, CARP, and s-SCP, it happens at $N = 100$, while for IRSAP, its peak can be achieved at around $N = 400$, which indicates that in IRSAP a much larger RIS is required to attain the maximum EE. The total EE performance of DAP-RARAP, shown in Figure 21e highlights that access policy combinations that use IRSAP can achieve higher performance, outperforming CRDSAP-included policy combinations by around 0.5 k packets/J for $N > 36$ elements. In addition, the total EE of DAP-RARAP cannot outperform the total EE of SAP-RARAP due to the mandatory performing training phase tasks, which consumes a high amount of power. However, the minimum performance of SAP-RARAP can be easily surpassed by DAP-RARAP, with ≈ 0.6 k packets/J for all N. This comparison is evident when we verify both methods plotted simultaneously in Figure 21f.

Finally, considering the MTDs EE metric, Figure 21i shows that MTDs are not able to achieve an EE higher than $\eta_{\text{MTD}} = 22.5$ k packets/J with SAP-RARAP. In addition, we notice that the MTDs EE is directly related to the average number of packets sent by MTDs: the higher the number of packets, the lower the η_{MTD} – except for s-SCP and CRDSAP, which the same amount of packets are sent on average. In that case, the MTD's EE is higher for s-SCP because this policy achieves a higher throughput when compared to CRDSAP. When the double-policy method is adopted, we notice that MTDs are able to achieve $\eta_{\text{MTD}} \approx 38$ k packets/J at $N = 200$ with IRSAP+CARP, which is almost twice as the maximum MTDs EE that can be achieved with SAP-RARAP. Results can be seen in Figure 21h, and a comparison between SAP-RARAP and DAP-RARAP is provided in Figure 21i. The behavior observed in Figure 21h happens because MTDs are able to perform smart power control when DAP-RARAP is adopted, allowing the reduction of MTDs uplink power if they are located at the green area of the communication cell.

In DAP-RARAP, we notice that policies that use CARP presented the best η_{MTD}, showing that the amount of packets sent by each access policy also matters, especially for MTDs at the red area. However, in Figure 21h, we note that by increasing the number of RIS elements, the MTD's EE achieves a peak and then starts to decrease. This is an intriguing result because the RIS power consumption is not included in the computation of η_{MTDS}; hence, the MTD's EE was expected to follow the same tendency of its achieved throughput, shown in Figure 21b, which have a plateau. Because of that, one may infer that P_{MTD} is increasing with N, affecting η_{MTD}. Due to the functionality of the protocol, this P_{MTD} increase can only happen when the amount of MTDs that transmits with higher power augments. To verify that, we investigate the optimal σ^2_{TH} as a function of N, and also simulate the percentage of MTDs that estimates their cell region as red and green as a function of N at a fixed σ^2_{TH} value. Both simulation results are shown in Figure 22.

5.5.5 Optimal Localization Threshold as a Function of N

In Figure 22a, the optimal localization threshold is obtained experimentally, as a function of N. Such optimal localization threshold is obtained as the median value of a large set of estimated localization threshold, σ^2_k, of MTDs randomly positioned within the communication cell shown in Figure 2. This median value is taken because the MTDs distribution through the adopted cell is uniform; hence, we have approximately half of them positioned at each cell region, which results in half of these MTDs being severely affected by the blockage and consequently having higher σ^2_k values. This median value will be where point the CDF of all obtained σ^2_k reaches 0.5, corresponding to half of the communication cell. See Figure 13c. The increasing behavior of the curve shown in Figure 22a can be explained by the fact that increasing the number of RIS' reflective elements allows augments the amount of power that is reflected by the RIS to MTDs located at the red side of the communication cell. As long as this higher power levels are experienced only at a small quantity of time slots, the variability of the channel qualities during the TDMA frame tends to increase, augmenting the optimal σ^2_{TH} value.

When this optimal value increases in practice but the localization threshold informed to MTDs remains fixed, MTDs positioned at the green side of the communication cell will begin to wrongly estimate their cell region as being red, which causes them to pick policy A_2 and power level ρ_{H} to perform uplink, augmenting the total amount of power expended by these devices. In Figure 22b, we show that if the localization threshold is kept $\sigma^2_{\text{TH}} = 1 \times 10^{-3}$ for all N values at larger RIS configurations, the number of missed classifications increases, augmenting the number of MTDs that classifies themselves as red in comparison to those that classifies themselves as green. Hence, if σ^2_{TH} remains constant, more uplink power is expended by MTDs, which reduces their EE. This explains the η_{MTD} decrease observed in Figure 21h.

To prove that, we repeated the simulation results presented in Figure 21 for DAP-RARAP and also the comparison among DAP-RARAP and SAP-RARAP. However, in this new setup, we consider that MTDs use the optimal σ^2_{TH} to make their decision rule instead of always using the value of $\sigma^2_{\text{TH}} = 1 \times 10^{-3}$. Results are shown in Figure 23. For this simulation, at each S value MTDs uses the threshold value plotted in Figure 22a as the variance boundary to estimate at which cell region they are. By comparing the results obtained with respect to the throughput (Figures 21b and 23a) and the total EE (Figures 21e and 23b) metrics, any remarkable difference can be noted. However, when we compare the MTDs' EE metric for DAP-RARAP (Figures 21h and 23c) we can notice a valuable performance gain when the localization threshold is adapted at each S.

5.5.6 SAP-RARAP and DAP-RARAP Performances as a Function of the Number of Time Slots

In this subsection, simulation results regarding the performance of SAP-RARAP and DAP-RARAP as a function of the number of time slots S are presented. We investigate the protocol performance in two scenarios:

1. The TDMA frame time, T_f, is kept fixed regardless of S; *i.e.*, at higher S values, the duration of each access and training slots are proportionally reduced in order to maintain T_f constant. Hence, G, η_{T}, and η_{MTD} metrics depend only on the number of packets successfully decoded with SIC.

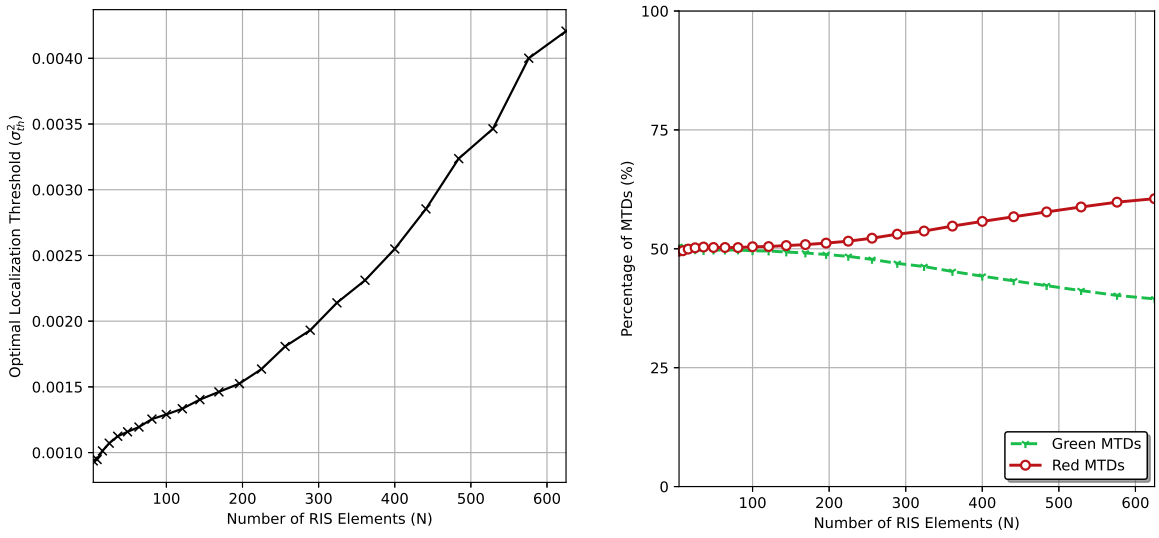

(a) (b)

Figure 22 – (a) Optimal localization threshold as a function of N and (b) classification percentage of MTDs as being at red and green areas as a function of N with a fixed threshold $\sigma^2_{\text{TH}} = 1 \times 10^{-3}$.

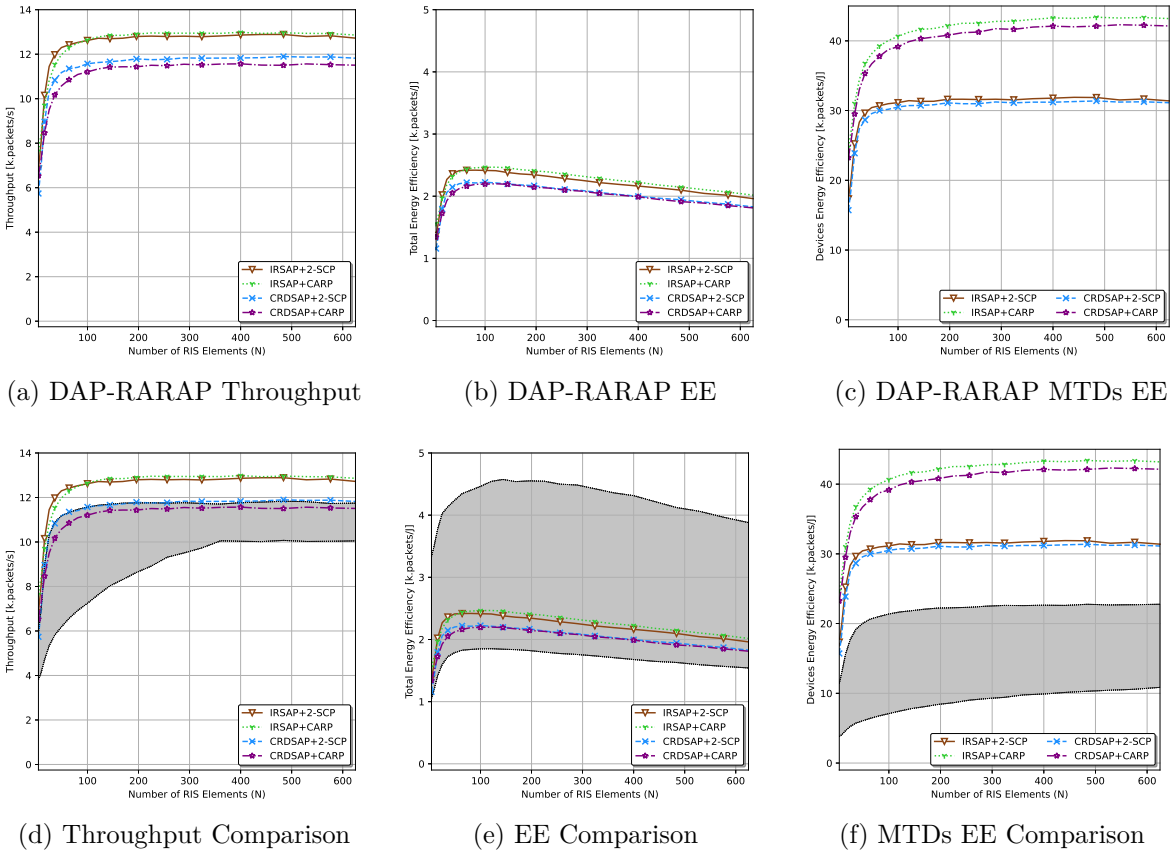

(a) DAP-RARAP Throughput (b) DAP-RARAP EE (c) DAP-RARAP MTDs EE

(d) Throughput Comparison (e) EE Comparison (f) MTDs EE Comparison

Figure 23 – DAP-RARAP performance as a function of N with optimal localization coefficients threshold adopted at each N value are shown in the first row. In the second row, a comparison performance of DAP-RARAP and SAP-RARAP is presented, where the SAP-RARAP performance is the same as the one obtained in Figure 21.

2. The duration of each access and training slot is fixed. In this scenario, at higher S values, the total frame time T_f also increases. Hence, G, η_{T} and η_{MTD} metrics depend not only on the number of packets that can be successfully decoded with SIC but also on the duration of the TDMA frame.

The obtained results for the scenario described in item (1) are presented and discussed in subsection 5.5.6.1, while scenario (2) is discussed in subsection 5.5.6.2.

In addition, similarly to what was observed in Subsection 5.5.4, varying S causes variations in the optimal localization coefficient used in DAP-RARAP. This variation was observed as a function of S, and simulation results are presented in Figure 24. Because of that, when the performance of DAP-RARAP is studied, we establish the optimal localization threshold as the correspondent value from the curve plotted in Figure 24 as the threshold used by MTDs to estimate at which cell region they are.

5.5.6.1 Protocols performance with fixed TDMA frame duration

We begin by analyzing the SAP-RARAP and DAP-RARAP performances as a function of S with a fixed TDMA frame duration. In such a case, as S increases, the duration of each training, access, and sigma slot (σ^*) are proportionally reduced in order to fit inside the pre-established frame time while keeping the training-access and the training-sigma ratios constant. Simulation results are presented in Figure 25, and Table 9 summarized the adopted simulation parameter values.

Parameter	**Value**
Number of MTDs	$K = 14$
Number of Time Slots	$S \in \{2, 40\}$
Frame Time	$T_f = 800$ μs

Table 9 – Adopted simulation parameter values that overrides those from Table 3 in the simulation shown in Figure 25.

By observing the throughput metric G of SAP and DAP approaches, which are shown in Figures 25a and 25b, respectively, we notice that the throughput increases when more time slots are available for MTDs. Indeed, by increasing S, MTDs can leverage this temporal diversity to perform the uplink of its data packets, and with more time slots available the collision probability can be reduced even for access policies that do not uses CSI, increasing the overall system throughput. One must also emphasize that by increasing S we are not only allowing MTDs to use more slots to perform the uplink, but also enhancing the spatial RIS diversity: the higher the S, the higher the number of

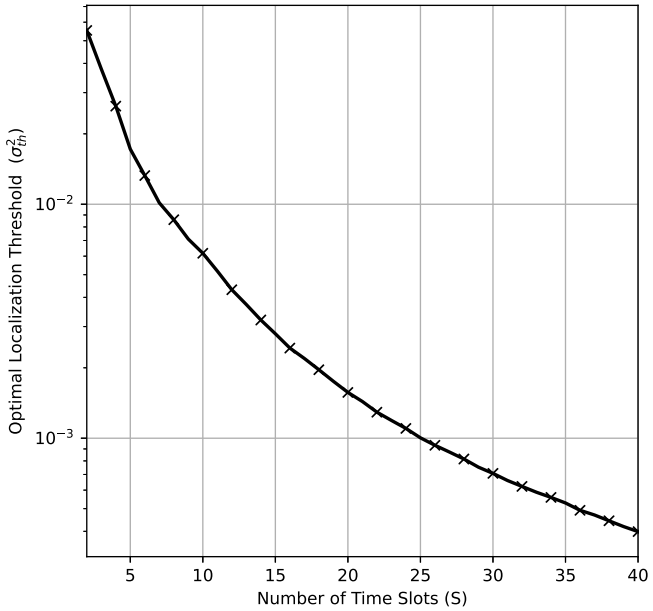

Figure 24 – Optimal localization thresholds (σ^2_{TH}) as a function of the number of time slots (S).

predefined RIS configurations that must be available at set $\mathbf{\Theta}$, which implies a smaller angular gap between two consecutive configurations (see Figures 5 and 6). As a result, more angular positions of the cell can be covered, which allows MTDs to select their slots with higher precision when a CSI-aided policy is adopted. Due to the constant T_f value, we notice that all throughput curves from Figures 25a and 25b tend to reach a maximum value at high S values, which can induce us to infer that the higher the S, the better.

However, increasing S can lead to several challenges during its real-life implementation. First of all, we must notice that in practice the RIS requires some time to shift from one configuration to another, which can cause SNR variations among consecutive slots in real applications. Hence, increasing S would augment the number of RIS re-configurations within a TDMA frame, which might be unfeasible due to hardware limitations. This limitation is associated with the fact that, with a constant T_f, the higher the S the faster the RIS must performs its elements adjustments, which depends on the available hardware. Finally, smaller slots can reduce the system SE, which harms the data transmission from MTDs to the BS. In Figure 25c it is possible to see that if $S \leq 14$, the SAP-RARAP is able to outperform DAP-RARAP's throughput. However, for higher S values, DAP-RARAP becomes the best protocol, surpassing the single-policy approach. This indicates that in DAP MTDs are able to better leverage the time slots to perform the uplink of data packets when a sufficient amount of slots are available. We must also notice that these values are observed for $K = 14$. Increasing K would certainly benefit the access policies that uses CSI because, as discussed in previous sections, these policies are able to take the spatiotemporal diversity into account when performing the uplink, preventing collisions and allowing a higher number of MTDs connected simultaneously.

With respect to the total system EE metric, we see in Figure 25d the policies that do not use CSI are able to achieve higher η_{T} in SAP-RARAP due to the absence of the training phase of the RA protocol. As a result, such policies can spare the downlink power that would be expended for broadcasting data pilots by the BS at S slots. However, these policies' performances still increasing for $S = 40$ slots, while 2-SCP presents an optimal operation point at $S = 22$ and CARP at $S = 16$. After this maximum point, CARP and 2-SCP start to decrease because the throughput gain provoked by adding more time slots is not as high as the power consumed by the whole system by adding these new slots; hence, the power consumption of the system continues to increase without throughput gains, harming the total EE. The tendency of IRSAP's and CRDSAP's EE is always increasing because the downlink of data pilots is not needed. Hence, the BS power consumption does not increase with S. Because of that, their η_{T} curves tend to reach a plateau, similarly to what happened with the throughput metric.

On the other hand, the total EE of DAP-RARAP (η_{T}) policies combinations, depicted in Figure 25e, reveal the same tendency of CARP and 2-SCP combinations, as

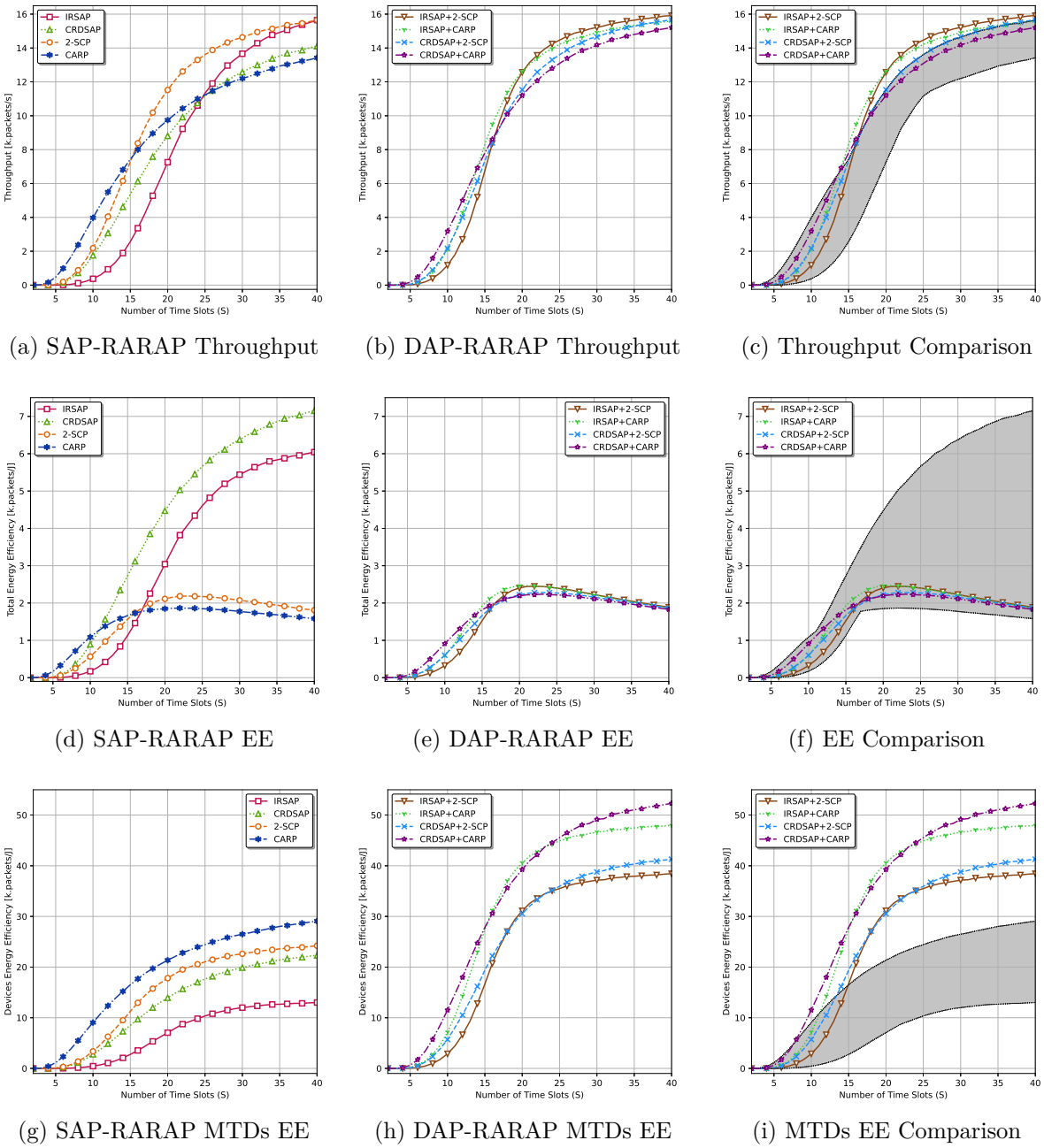

(a) SAP-RARAP Throughput (b) DAP-RARAP Throughput (c) Throughput Comparison

(d) SAP-RARAP EE (e) DAP-RARAP EE (f) EE Comparison

(g) SAP-RARAP MTDs EE (h) DAP-RARAP MTDs EE (i) MTDs EE Comparison

Figure 25 – [$T_f = 800$ **fixed,** S **variable**] – SAP-RARAP and DAP-RARAP performances as a function of the number of time slots (S). Regardless of S, we consider $T_f = 800$ μs. The third column contains the DAP-RARAP lines plotted, and the shaded area represents the range between maximum and minimum values that can be achieved with SAP-RARAP.

observed in SAP-RARAP, which can be explained by the fact that the broadcast of data pilots always must be performed in DAP-RARAP, increasing the BS consumption power with S regardless of the adopted policies combinations. For DAP-RARAP, the maximum η_{T} is attained at the same S for all access policies combinations, at $S = 22$. By comparing the η_{T} of both approaches in Figure 25f, we notice that SAP is able to outperform DAP for all S values, specially due to the non CSI-aided policies adopted in SAP. In that case, the peak EE achieved with IRSAP+CARP, which can be viewed as the '*global maximum*' η_{T} for DAP-RARAP, is much lower than the maximum EE achieved with SAP-RARAP.

Finally, analyzing the EE metric for the MTDs (η_{MTD}) under SAP-RARAP policies, shown in Figure 25g, one can notice that all curves follow the tendency of the throughput plotted in Figure 25a, tending to a plateau at higher S. However, we notice that access policies that send fewer packets are more beneficial for MTDs' EE because CARP presented the best η_{MTD} for all S, followed by 2-SCP, CRDSAP and IRSAP, respectively. The variant 2-SCP, despite presenting the best throughput among the four policies analyzed in a vast S region ($S > 16$), it was not able to surpass the CARP η_{MTD} for any S because CARP sends, on average, 33.5 % less packets than s-SCP, saving a significant amount of power. MTDs that use 2-SCP and CRDSAP consume the same power because both policies require the uplink of two packets replicas; however, 2-SCP outperforms CRDSAP since it can achieve higher throughput for all S. Due to the fact that IRSAP sends a higher number of replicas, on average, when compared with the other three policies, it presented the worse η_{MTD} for all S.

In DAP-RARAP, the MTDs' EE shown in Figure 25h also follows the same tendency of the achieved throughput curves from Figure 25b, also reaching a plateau at higher S. We notice that combinations that adopt CARP achieved better performance when compared with combinations that use 2-SCP, which can also be explained by the smaller number of replicas sent. CRDSAP+CARP presented the best performance for $S \leq 15 \cup S \geq 24$, being very competitive with IRSAP+CARP for $16 \leq S \leq 23$. We notice that the average number of packets sent by MTDs located at the red region dictates the overall MTDs' EE. Indeed, these MTDs use higher power levels to transmit; hence, reducing the number of replicas sent by them is paramount. Moreover, because the number of replicas sent by CARP is smaller than 2-SCP, both CARP combinations outperform the η_{MTD} of 2-SCP approaches. Furthermore, by allowing MTDs from the green area to transmit their packets at lower power levels, the EE of them can be drastically enhanced. As a result, the overall η_{MTD} of DAP-RARAP can easily outperform the SAP-RARAP for almost all S values analyzed, achieving near twice (1.85) the maximum EE obtained with SAP-RARAP for higher S values, as we can see in Figure 25i.

5.5.6.2 Performance under variable TDMA frame duration

In this subsection we repeated the simulation setup shown in Figure 25, but now varying the duration of the TDMA at each S value. Hence, T_{as}, T_{ts} and T_{σ} are fixed. We also ensure that $T_f = 800$ μs for $S = 20$ slots, as adopted in Figure 25 for all S. This approach is paramount because if the duration of each training and access slot can not be proportionally reduced with the addition of more access slots (*e.g.*, due to RIS hardware limitations or minimal duration of time slots requirement) one can observe the number of time slots and the access policies or combinations of access policies that can be adopted in order to maximize the performance of the GF-RA protocols. Adopted simulation parameter values different from the default values (Table 3) are highlighted in Table 10.

Parameter	**Value**
Number of MTDs	$K = 14$
Number of Time Slots	$S \in \{2, 40\}$
Access Slot duration	$T_{as} \approx 33.195$ μs
Training Slot duration	$T_{ts} \approx 6.639$ μs
Sigma Slot duration	$T_{\sigma} \approx 3.319$ μs

Table 10 – Adopted simulation parameter values that overrides those from Table 3 in the simulation shown in Figure 26. The values adopted for T_{as}, T_{ts} and T_{σ} ensure that for $S = 20$, $T_f = 800$ μs.

By observing Figure 26a, we notice that if large quantities of time slots are available, the system throughput is harmed, differently from what was observed in Figure 25a, where a monotonically increasing tendency was noted. This happens because at higher S, if the number of contending MTDs is sufficiently low, adding more slots will only increase the duration of the TDMA frame without allowing the transmission of more data packets, causing a throughput reduction. We also notice that each access policy has an optimal operation point: for CARP, the maximum throughput is achieved at $S = 17$, for 2-SCP at $S = 20$ and for CRDSAP and IRSAP when $S = 22$ and $S = 28$ slots are available, respectively. One can affirm that access policies that use CSI can attain their maximum operation point at a lower S when compared to policies that require CSI. Furthermore, CARP and s-SCP peaks can outperform those from CRDSAP and IRSAP, while CARP and s-SCP are able to provide $G \approx 10.0$ and $G \approx 11.5$ k.packets/s, CRDSAP and IRSAP can attain at most $G \approx 9.0$ k.packets/s, revealing the importance of CSI availability for MTDs.

By combining two access strategies inside DAP-RARAP policy, one can notice that depending on the access policy adopted, the optimal S value changes. Simulation results can be observed in Figure 26b. For CRDSAP+CARP, its peak is observed at $S = 18$, while when IRSAP+CARP policy is adopted, we notice the maximum throughput value at

$S = 19$. Both combinations that use 2-SCP as policy A_1 attain the maximum throughput at $S = 20$ slots, with IRSAP+2-SCP outperforming CRDSAP+2-SCP by approximately 1 k.packets/s. Despite DAP-RARAP requiring more time slots to attain its maximum G, when compared to SAP-RARAP with policies that require CSI, the double-policy approach is able to outperform SAP-RARAP if $S \geq 14$ slots are available, and if proper combinations of access policies are selected in DAP-RARAP. Specifically, IRSAP+CARP

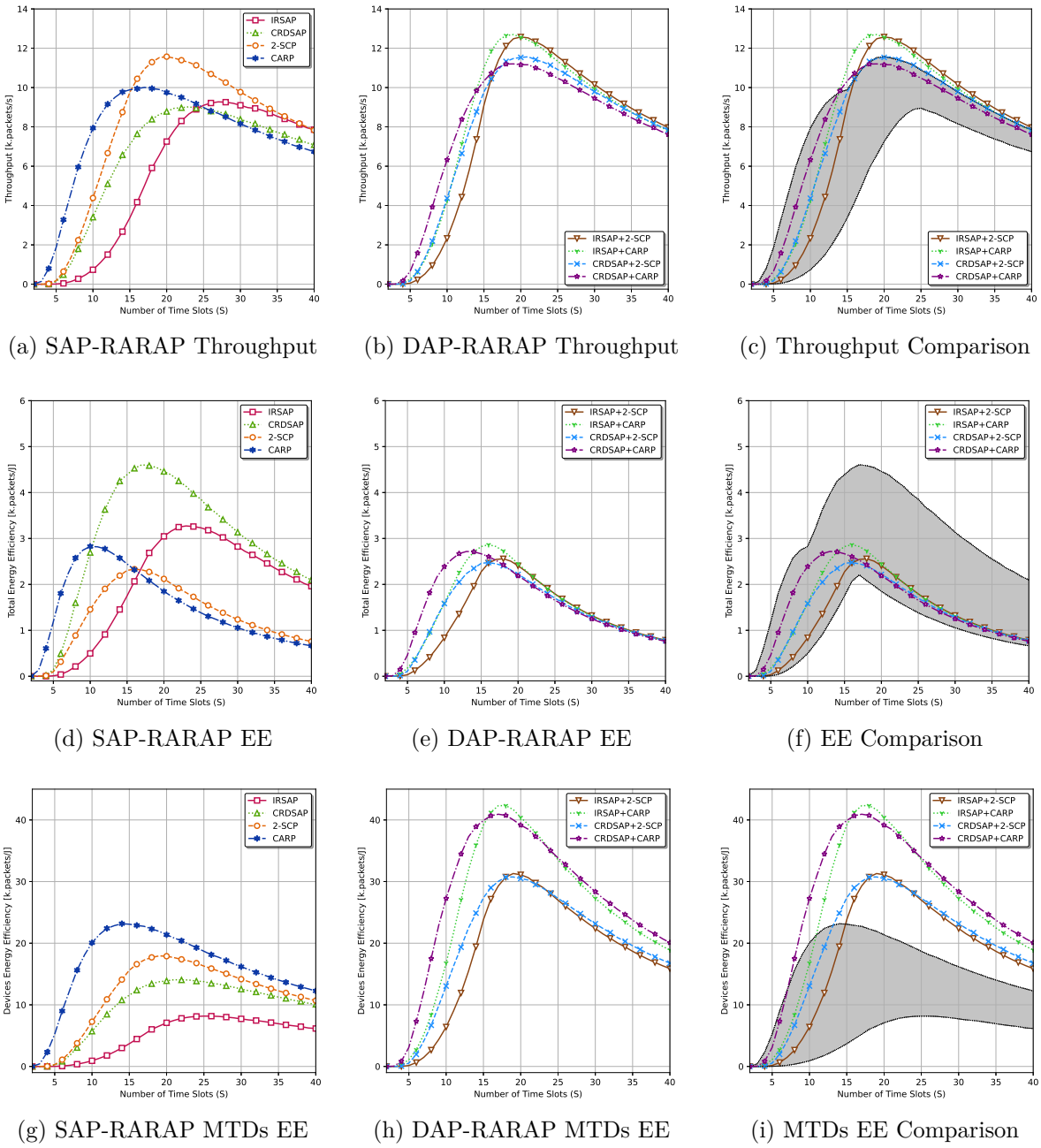

(a) SAP-RARAP Throughput (b) DAP-RARAP Throughput (c) Throughput Comparison

(d) SAP-RARAP EE (e) DAP-RARAP EE (f) EE Comparison

(g) SAP-RARAP MTDs EE (h) DAP-RARAP MTDs EE (i) MTDs EE Comparison

Figure 26 – [T_f **variable,** $S = 20$ **fixed**] – SAP-RARAP and DAP-RARAP performances as a function of the number of time slots (S). T_f varies with S, and at $S = 20$ we have $T_f = 800$ μs. The third column contains the DAP-RARAP lines plotted, and the shaded area represents the range between maximum and minimum values that can be achieved with SAP-RARAP.

and IRSAP+2-SCP combinations presented the most notorious throughput for $S \geq 14$ gains when compared with SAP-RARAP, as we can see in Figure 26c.

When we analyze the η_{T} of SAP-RARAP protocol, Figure 26d, we can notice one more time that the access policies that perform the data uplink blindly (CRDSAP and IRSAP) can achieve the best performance. The peaks of these curves happen at $S = 17$ and $S = 23$ slots, respectively. CARP and 2-SCP are able to achieve an $\eta_{\text{T}} \approx 2.8$ and $\eta_{\text{T}} \approx 2.3$ [k.packets/s], respectively, with its maximum occurring when $S = 10$ and $S = 16$ slots, respectively. When DAP-RARAP is employed, the achievable peak η_{T} is similar to the peak performance of SAP-RARAP when RIS-aided policies are used due to the downlink training step. CRDSAP+CARP policy presented its maximum EE performance at $S = 13$ slots, while CRDSAP+2-SCP and IRSAP+CARP performed better at $S = 16$ slots. IRSAP+2-SCP requires more time slots to achieve its optimum EE performance, requiring $S = 18$ slots. Regardless of S, DAP-RARAP's η_{T} have been outperformed by SAP-RARAP's, as we can see in Figure 26f.

Finally, by analyzing the MTD's EE of SAP-RARAP (Figure 26g) and DAP-RARAP (Figure 26h), we notice that the curves follows the tendency of the respective throughput, shown in Figures 26a and 26b, with the difference that the less the amount of packets sent, the greater the η_{MTD}. Furthermore, we notice in Figure 26i that DAP-RARAP can easily outperform SAP-RARAP, especially when CARP-aided combinations are employed. This remarkable performance is a consequence of the low amount of packets required in this policy.

5.5.7 Fairness

5.5.7.1 Fairness as a Function of Number of RIS Elements

Simulation results regarding the fairness performance of SAP-RARAP and DAP-RARAP protocols are presented in Figure 27. Specifically, Figure 27a shows the results for the single-policy approach, and as we can see, higher Jain's indexes can be obtained when access policies that leverage CSI are employed. When CSI is available for 2-SCP and CARP, MTDs avoid sending their packets in slots with poor channel conditions, reducing their probability of losing the packet and also utilizing slots with good qualities. Hence, more MTDs can be connected at similar SE levels, which explains the higher Jain's fairness index for these policies. Despite that, we notice that due to the vast area, the blockage, and the single uplink power level available for MTDs, even with CSI, their fairness can attain at most $J = 0.615$. When policies that do not use CSI are adopted, we notice that they increase with N due to the higher probability that these policies have of sending a packet in a slot that fulfills the minimum SIC requirement. In that case, the increasing behavior is associated with the throughput: we saw in Figure 21a that for IRSAP and CRDSAP, the throughput is very sensitive with N, and by increasing the

throughput, we are allowing more MTDs on the network, avoiding them to have a null SE, which enhances their fairness.

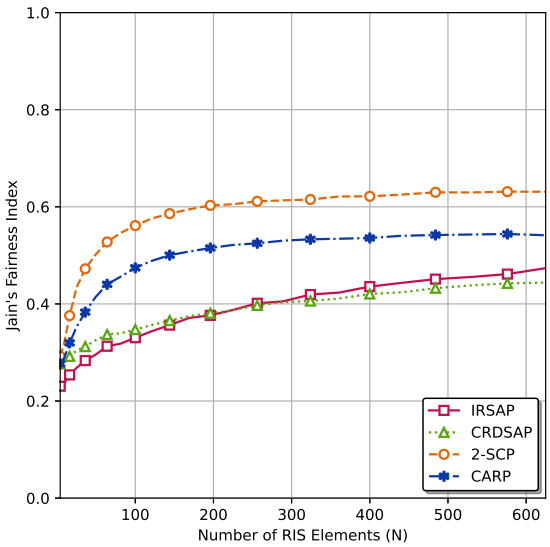

(a) SAP-RARAP Fairness

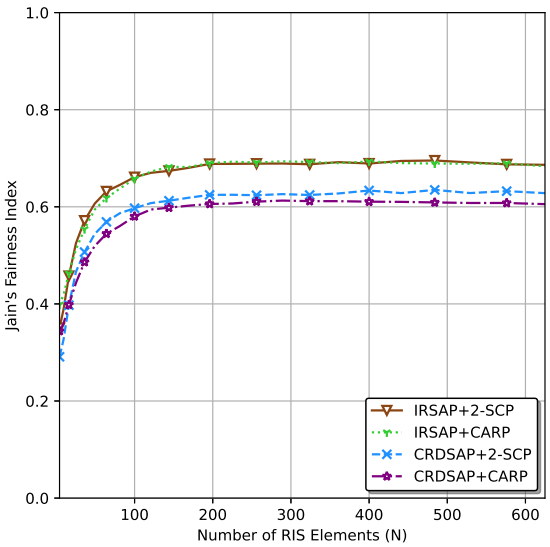

(b) DAP-RARAP Fairness

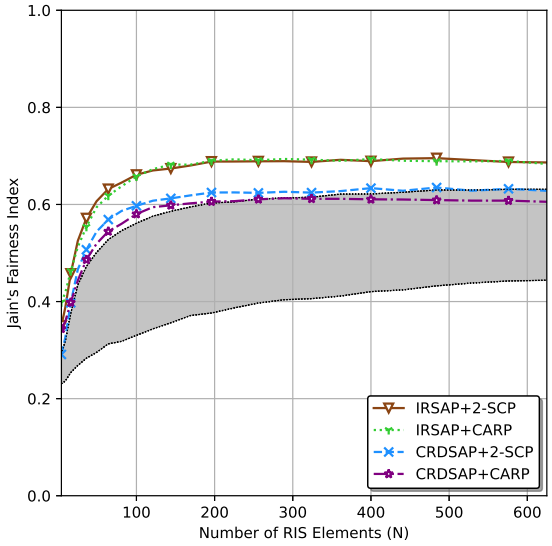

(c) Fairness Comparison

Figure 27 – SAP-RARAP and DAP-RARAP fairness performance as a function of the number of RIS elements (N). The third column contains the DAP-RARAP lines plotted, and the shaded area represents the range between maximum and minimum values that can be achieved with SAP-RARAP.

On the other hand, if DAP-RARAP is adopted, its flexibility w.r.t. the adopted access policy and the availability of two power levels for the uplink allows a slight increase in the Jain's fairness index, as we can see in Figure 27b. Hence, one can say that in DAP-RARAP, MTDs present a more balanced SE. Indeed, this behavior occurs because in the double-policy approach, one can induce MTDs from the green area to uplink their packets at a low power level, reducing their SNRs and letting them more similar to red-

side ones, enhancing the fairness. Because of that, we notice that in DAP-RARAP the fairness is enhanced at the expense of a SE reduction, especially for MTDs in the green area. However, as in mMTC scenarios, we do not have high data traffic requirements, but high-density of MTDs; this can be done without harming the scenario's functionality if carefully designed.

Finally, Figure 27c shows the fairness comparison of both approaches. We notice that if proper access policies are adopted, specifically IRSAP+2-SCP and IRSAP+CARP one can obtain a gain of approximately 10 % in the system fairness.

5.5.7.2 Fairness as a Function of MTDs Uplink Power

Simulation results regarding the fairness performance of DAP-RARAP protocol are provided in Figure 28. The dotted lines at the xy-plane are the minimal uplink power values necessary to attain 95 % of the maximum fairness. The maximum fairness values and these 95 % points are summarized in Table 11. We notice that the surface plots of Figure 28 reveal a similar shape as the throughput surfaces shown in Figure 17. However, the minimum power required to attain 95 % peak fairness performance is much higher in the fairness metric. Indeed, the communication cell's size and the presence of blockage make it challenging to obtain extremely fair scenarios. Furthermore, some MTDs are not able to connect to the network due to collisions and/or poor channel conditions, which leaves them with a null SE, harming fairness.

With respect to the system performance, we notice that the combination of access policies that attained the maximum peak fairness was IRSAP+CARP, as shown in Figure 28b, attaining a peak Jain's index of $J \approx 0.76$. MTDs are able to attain 95 % of this fairness, *i.e.,* $J_{95\%} \approx 0.722$ at $(\rho_{\text{L}}; \rho_{\text{H}}) = (3.10; 19.56)$ dBm. The second fairer combination of access polices was IRSAP+2-SCP, and as we can see in Figure 28a it attains a peak fairness of $J \approx 0.7539$. In this case, MTDs are able to achieve $J_{95\%} = 0.759 \cdot 95\ \% \approx 0,716$ at $(\rho_{\text{L}}; \rho_{\text{H}}) = (5.86; 25.17)$ dBm. The third best fairness was obtained with CRDSAP+2-SCP, which fairness surface is shown in Figure 28c. In this case, the maximum fairness was $J \approx 0.6845$, with 95 % of it being attained at $(\rho_{\text{L}}; \rho_{\text{H}}) = (3.10; 19.65)$ dBm. Finally, CRDSAP+CARP presented the worst fairness performance, with a peak value of $J \approx 0.6764$, as we can see in Figure 28d. In this last case, such fairness is attained with $(\rho_{\text{L}}; \rho_{\text{H}}) = (5.86; 22.41)$ dBm. For all four combination policies, one can notice that higher power levels result in higher fairness; hence, for the studied scenario, higher power levels are unfeasible due to the drastic reduction in the MTDs' EE, as previously discussed.

SAP-RARAP Jain's fairness performance is shown in Figure 29. We notice that when SAP-RARAP's fairness performance is observed, access policies that use CSI are able to achieve its 95 % peak fairness at lower uplink power levels. Specifically, the access policy that achieved the best fairness with SAP-RARAP was IRSAP with $J \approx 0.7406$,

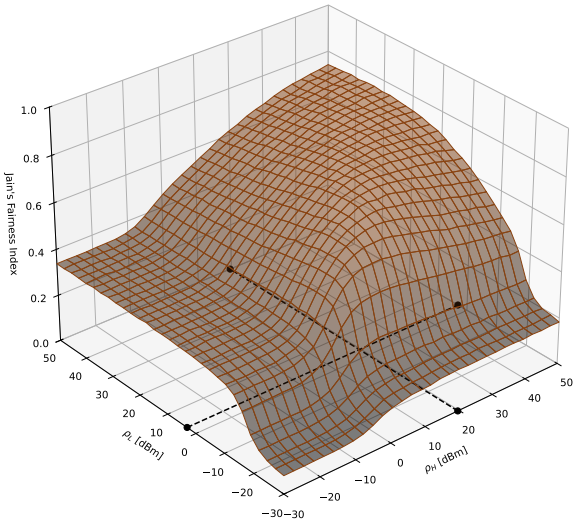

(a) IRSAP+2-SCP

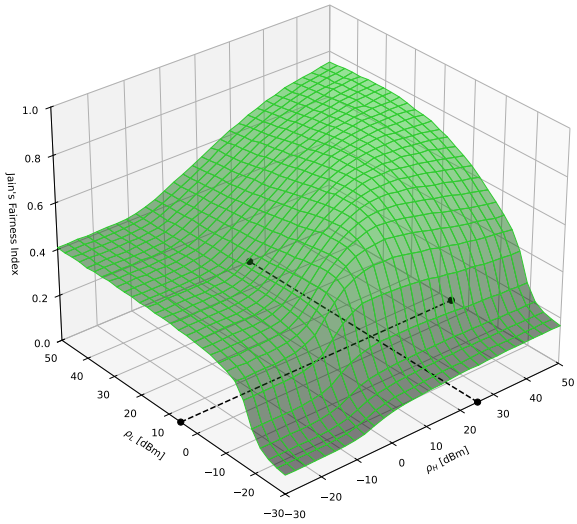

(b) IRSAP+CARP

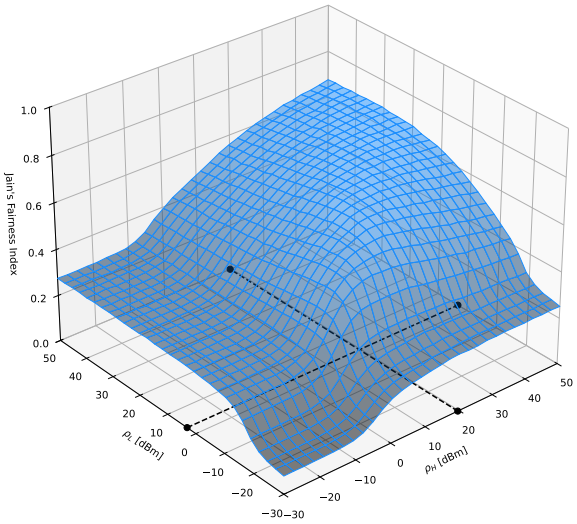

(c) CRDSAP+2-SCP

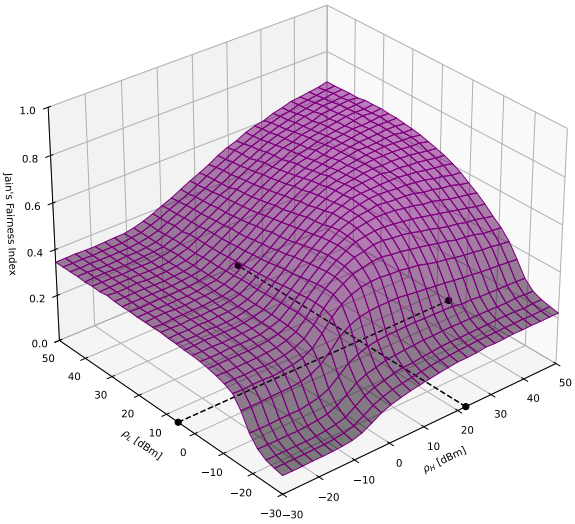

(d) CRDSAP+CARP

Figure 28 – Fairness of DAP-RARAP protocol as a function of ρ_{H} and ρ_{L} for all studied combinations of access policies.

Metric	**Policies**	**Subfigure**	**Maximum**	**MTDs Optimal Powers**	
				ρ_{L}	ρ_{H}
Fairness	IRSAP+2-SCP	28a	0.7539	3.10 dBm*	19.65 dBm*
	IRSAP+CARP	28b	0.7652	5.86 dBm*	25.17 dBm*
	CRDSAP+2-SCP	28c	0.6845	3.10 dBm*	19.65 dBm*
	CRDSAP+CARP	28d	0.6764	5.86 dBm*	22.41 dBm*

*Minimal powers required to achieve *at least* 95 % of the maximum fairness value.

Table 11 – Optimal fairness points achieved with simulation results for DAP-RARAP protocol.

requiring $\rho_k \approx 38.96$ dBm to attain 95 % of it. CRDSAP and 2-SCP presented very similar peak fairness performance, with $J \approx 0.6628$ and $J \approx 0.6709$, respectively. These

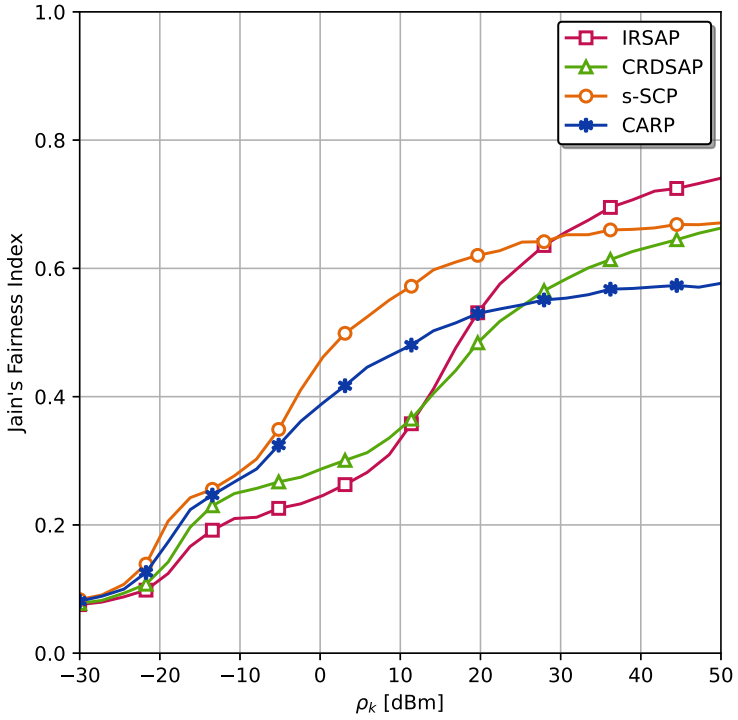

Figure 29 – Fairness of SAP-RARAP protocol as a function of ρ_k.

access policies can achieve 95 % of their respective peak fairness respectively at $\rho_k = \rho_{\text{H}} = 41.72$ dBm and $\rho_k = 27.93$ dBm. one can notice that 2-SCP can achieve this 95 % threshold with a significant lower uplink power, which is paramount in mMTC scenarios. The access policy that performed worse w.r.t. the fairness metric was CARP, which its peak being $J = 0.5767$, and its 95 % threshold happening with $\rho_k = \rho_{\text{H}} = 27.93$ dBm. Again, the fact that CARP achieves 95 % of its peak fairness performance at lower power levels when compared with IRSAP and CRDSAP shows that although these policies are not able to present higher fairness levels with SAP-RARAP, they can let these fairness level be attained at lower power levels, which is essential for mMTC scenarios.

Metric	**Policies**	**Figure**	**Maximum**	**MTDs Optimal Powers**
				ρ_k
Fairness	IRSAP	29	0.7406	38.96 dBm*
	CRDSAP	29	0.6628	41.72 dBm*
	2-SCP	29	0.6709	25.17 dBm*
	CARP	29	0.5767	27.93 dBm*

Minimal powers required to achieve *at least* 95 % of the maximum fairness value.

Table 12 – Optimal fairness points achieved with simulation results for SAP-RARAP protocol.

Remark: when we vary the MTDs uplink power, DAP-RARAP fairness performance is able to slightly outperform SAP-RARAP's, with a remarkable reduction in the MTDs uplink power. This reduction is even more crucial when we compare ρ_k in SAP-RARAP

with ρ_{L} in DAP-RARAP: MTDs from the green area can reduce 20 dBm in their uplink power and still achieve a relatively fair performance.

5.5.8 SAP-RARAP and DAP-RARAP Performances as a Function of the Blockage Attenuation

This subsection presents the performance of RA SAP and DAP RARAP protocols under different **blockage attenuation** (ξ) scenarios, which might be useful depending on the blockage's physical properties. Blockage attenuation was defined in Equation (4.5). Table 13 illustrates blockage attenuation (dB) values for different wall materials. In our previous simulations, we adopted $\xi = 40$ dB, which, according to Table 13, can be applied if the blockage is made of reinforced concrete, metal, or stone. The values provided in the table are based on general observations and studies in wireless communications and signal propagation [50, 51]. These values are commonly referenced in research papers, textbooks, and technical reports on radio frequency (RF) propagation and wireless network planning. Basically, the *blockage attenuation factor* depends on:

- *Frequency Dependence:* Attenuation increases with higher frequencies (e.g., 5 GHz signals experience more attenuation than 2.4 GHz signals).
- *Wall Thickness:* Thicker walls generally result in higher attenuation.
- *Material Composition:* Variations in material density, moisture content, and reinforcement can significantly affect attenuation.

Before presenting the throughput, the EE and MTDs' EE results, similarly to what was made for DAP-RARAP protocol in subsection 5.5.6, we find the optimal localization thresholds, σ^2_{TH}, and results are presented in Figure 30.

The performances of the studied protocols as a function of the blockage attenuation ξ are presented in Figure 31. For the DAP-RARAP protocol, for each ξ value, we adopted the optimal localization threshold σ^2_{TH} as the correspondent value shown in Figure 30. By observing the SAP-RARAP throughput results in Figure 31a, we notice that access policies that uses CSI are less affected by higher levels of blockage attenuation because even with its direct link completely blocked (*i.e.*, at higher ξ values), these access policies can explore the channel diversity induced by the RIS efficiently to perform the data uplink. However, under lower blockage attenuation scenarios, CRDSAP and IRSAP can outperform the RIS-aided policies by a few k.packets/s. In fact, these policies perform the data uplink blindly, *i.e.*, without knowing the channel qualities, and when the attenuation imposed by the blockage augments, MTDs have a higher probability of sending data packets in a slot whose SNR will not fulfill the SIC requirement, which harms the throughput.

Wall Type	**Blockage Attenuation ξ (dB)**	**Description**
Drywall (Plasterboard)	3–5	Common in interior walls; low attenuation due to lightweight material.
Wooden Wall	5–12	Moderate attenuation depending on thickness and density of the wood.
Glass (Non-Tinted)	2–6	Low attenuation for plain glass; higher for thicker glass.
Glass (Tinted/Metalized)	10–20	Higher attenuation due to metallic coating or tinting.
Brick Wall	10–20	Significant attenuation depending on brick density and wall thickness.
Concrete Wall	15–30	High attenuation due to dense material and reinforcement.
Reinforced Concrete	20–40	Very high attenuation due to steel reinforcement and dense concrete structure.
Metal Wall	40–60+	Extremely high attenuation; metal acts as a strong barrier to signal propagation.
Cinder Block Wall	10–25	Moderate to high attenuation depending on block density and wall thickness.
Stone Wall	20–40	High attenuation due to dense and irregular material composition.

*Table adapted from [50, 52, 51, 53, 54].

Table 13 – Blockage attenuation for different wall types.

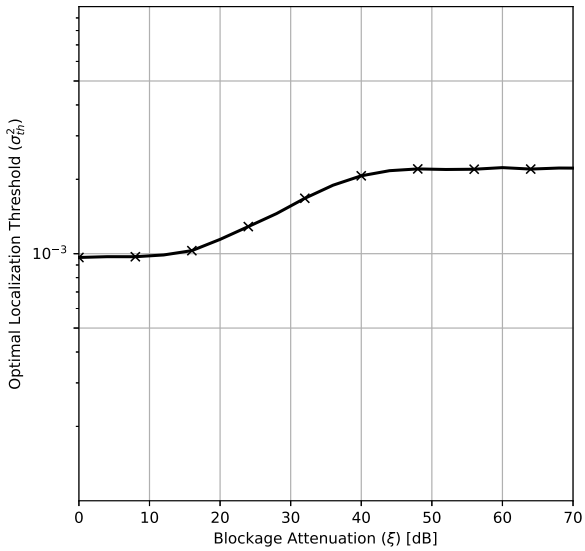

Figure 30 – Optimal localization thresholds (σ^2_{TH}) as a function of the blockage attenuation (ξ).

By adopting DAP-RARAP, Figure 31b, the overall system throughput suffers a slight reduction from $\xi = 15$ to $\xi = 40$, as in SAP-RARAP. Because of that, one can affirm that DAP-RARAP is a robust protocol that presents similar performance under a vast range of ξ scenarios. Specifically, the gap between the maximum and minimum throughput performance of DAP-RARAP protocol is less than 2 k.packets/s regardless

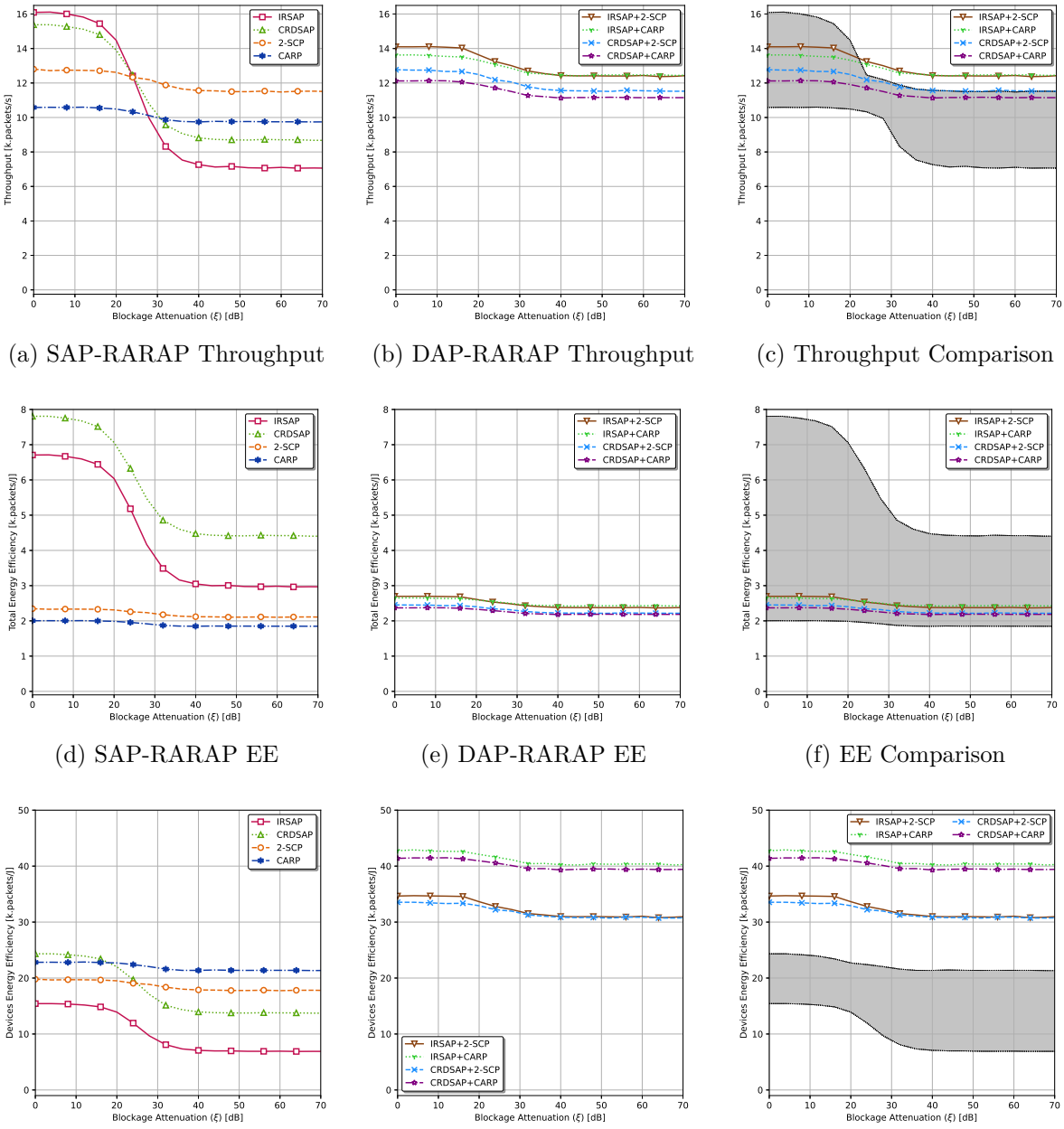

(a) SAP-RARAP Throughput (b) DAP-RARAP Throughput (c) Throughput Comparison

(d) SAP-RARAP EE (e) DAP-RARAP EE (f) EE Comparison

(g) SAP-RARAP MTDs EE (h) DAP-RARAP MTDs EE (i) MTDs EE Comparison

Figure 31 – SAP-RARAP and DAP-RARAP performances as a function of the blockage attenuation (ξ). The third column contains the DAP-RARAP lines plotted, and the shaded area represents the range between maximum and minimum values that can be achieved with SAP-RARAP

of the combination of access policies adopted. Furthermore, when the double-policy approach is adopted, if proper combinations of access policies are selected, the overall system throughput can outperform the peak SAP-RARAP performance, as shown in Figure 31c. Specifically, DAP-RARAP presented better performance than SAP-RARAP for $\xi > 22$ dB when IRSAP-included policies are used, with both of them performing very close to each other regardless of ξ value into a wide range.

For the EE metric, we notice that SAP-RARAP's and DAP-RARAP's η_{T} are strictly related to the system throughput because the EE curves shown in Figures 31d and 31e presents the same tendency as the respective throughput ones, shown in Figures 31a and 31b, respectively. Indeed, the blockage attenuation does not cause any additional power consumption, which makes the EE performance only throughput-dependent if all other parameters are kept constant, as is the case here. In Figure 31f, we see that DAP-RARAP is not able to surpass the SAP-RARAP EE at any ξ, which again is due to the obligation of performing the training step regardless of the combination of access policies adopted.

For MTD's EE calculation, we again notice that for both SAP and DAP-RARAP (Figures 31g and 31h, respectively), the curves follows the same shape as the respective throughput curves. However, differently from the EE metric, we see that policies that send less packets performed better than policies that require more replicas. By comparing both approaches in Figure 31i, we see a remarkable gain in the η_{MTD} metric in DAP-RARAP protocol for all ξ, achieving almost twice as the peak η_{MTD} than SAP if proper access policies are employed, specially DAP-RARAP policies combinations that use CARP.

5.5.9 Computational Complexity of SAP-RARAP and DAP-RARAP

In this section, we derive the expressions regarding the computational complexity of the studied RA protocols. The complexity is analyzed on the MTD side, and the presented expressions take into account the number of operations needed to perform the channel estimation, the calculation of the channel qualities, and the access policy rules. We start by counting the number of each math operation needed to be performed by MTDs, then we convert such amount of operations to *floating point operation* (flops) aiming to compare both approaches and access policies in an appropriate basis. To derive the computational complexity expressions, we use a to represent the number of flops required to perform additions and subtractions, m is the number of flops required in each multiplication, and d in each division. c and s are the number of flops required for a comparison and for a square-root operation, respectively. Finally, an operation of randomization is considered to consume r flops.

Channel Estimation Complexity: For both RA protocols, if MTDs need CSI, they must perform the estimation of S channel coefficient during the TDMA frame. Recall that these coefficients are denoted by $\hat{h}_k[s]$ and are calculated by equation (4.13). To calculate that, each MTD requires τ complex-complex multiplications (m_{cc}), also $\tau - 1$ complex-complex sums (a_{cc}), a single real-complex multiplication (m_{rc}) and a single real-real multiplication (m_{rr}). These computations are made S times within the TDMA frame. Hence, to perform the channel estimation, MTDs require the number of flops n_f^{CE} described

by equation (5.10) to perform the channel estimation within a TDMA frame.

$$n_f^{\text{CE}} = \tau \cdot m_{cc} + (\tau - 1) \cdot a_{cc} + m_{rc} + m_{rr}. \tag{5.10}$$

Channel Qualities Computation: Given the estimated channel coefficients, MTDs must estimate S channel qualities, given by equation (4.14). For that, they must perform 2 real-real multiplications, 1 real-real sum and 1 square-root (s) operation. Again, this computation is made S times per frame. The amount of flops required to perform the computation of the channel qualities is expressed in equation (5.11).

$$n_f^{\text{CQ}} = S \cdot (2m_{rr} + a_{rr} + s) \tag{5.11}$$

Complexity of Access Policies: Depending on the access policy, we have different complexities. We list the complexity of each access policy adopted in SAP-RARAP in the following.

1. **IRSAP:** First, each MTD picks a random number according to the PDF distribution of equation (4.19). The result of this randomization will be s_k, the number of replicas that this MTD will send. Then, this MTD selects s_k slots from a total of S in order to perform the uplink. Hence, we need $s_k + 1$ randomizations in IRSAP. This is performed once per frame. On average, MTDs with IRSAP requires

   $$n_f^{\text{IRSAP}} = (\overline{n}_k^{\text{IRSAP}} + 1) \cdot r \tag{5.12}$$

   flops to decide in which slots they will uplink its data packets, where $\overline{n}_k^{\text{IRSAP}}$ is the average number of packets sent by MTDs when IRSAP is adopted.

2. **CRDSAP:** MTDs using this policy will always send two replicas. Hence, this policy requires only a total of $s_k = 2$ randomizations:

   $$n_f^{\text{CRDSAP}} = 2 \cdot r \tag{5.13}$$

3. **s-SCP:** This policy requires the computation of the s maximum values among a collection of S samples. Hence, for 2-SCP, two maximum operations must be performed. The maximum can be obtained by comparing all S channel qualities, and the second greater value would require $S - 1$ comparisons. Hence, we can write that s-SCP requires

   $$n_f^{\text{S-SCP}} = \frac{S!}{(S-s)!} \cdot c \tag{5.14}$$

4. **CARP:** This policy requires the computation of the S $p_k[s]$ values described in equation (4.20). To do that, the denominator can be computed only once, requiring $S-1$ real-real sums. Then, for each slot, equation (4.20) must be computed, requiring

one real-real division. Next, MTD randomized S values and compare each one with the obtained $p_k[s]$ values. Hence, S randomizations plus S comparisons are required in each TDMA frame. Mathematically, the total amount of flops required by CARP is calculated by equation (5.15)

$$n_f^{\text{CARP}} = (S-1) \cdot a_{rr} + S \cdot d_{rr} + S \cdot (r+c). \tag{5.15}$$

Complexity of Localization Coefficients: When DAP-RARAP is adopted, MTDs must normalize their estimated channel qualities, then calculate their variance in order to obtain their localization coefficient, σ_k^2. The normalization, computed as in equation (4.17), requires $S-1$ real-real sums and S real-real divisions. Furthermore, the computation of σ_k^2, shown in equation (4.18), requires $S-1$ real-real sums and one real-real division to compute the mean of $z_k[s]$ and additional $2S$ real-real sums, S real-real products and a real-real division. Mathematically, we obtain the number of flops required for that as shown in equation (5.16):

$$n_f^{\text{LC}} = 2 \cdot (S-1) \cdot a_{rr} + S \cdot d_{rr} + 2 \cdot d_{rr} + 2 \cdot S \cdot a_{rr} + S \cdot m_{rr} \tag{5.16}$$

5.6 Comparison: Synthesis and Findings

This section presents a comparative analysis of the proposed SAP and DAP RA protocols. For each approach, all access policies (IRSAP, CRDSAP, s-SCP, CARP) are summarized in Table 14 and complemented with observations and insights obtained from previous sections of this chapter.

Remarks

CSI Usage: Access policies that *always leverages CSI*, namely s-SCP, and CARP, generally provide better throughput and fairness, especially in more challenging scenarios (*e.g.*, under high blockage attenuation). However, when DAP-RARAP is employed, all MTDs must obtain the S channel estimates during training in order to perform the estimation of their respective σ_k^2. When $\sigma_k^2 < \sigma_{\text{TH}}^2$, MTDs in DAP-RARAP adopt CRDSAP or IRSAP to perform the uplink, which does not leverage CSI in their decision rules. Hence, one can say that when it happens, IRSAP and CRDSAP are performed without its main advantage, *i.e.*, the non-necessity of channel estimation. Regardless of that, we have shown in the numerical results section that when CRDSAP and IRSAP are performed only by MTDs in the green area, the overall G and η_{MTD} can be enhanced, which seems like a fair trade-off for the studied scenario.

DAP-RARAP Advantages: DAP-RARAP's adaptive nature leads to significant performance improvements over SAP-RARAP in many interesting scenarios: higher throughput can be provided with it at scenarios where the blockage attenuation is high, which highlights the double-policy approach robustness; higher throughput can also be observed

with the deployment of smaller RIS', which is crucial for the project cost in a future implementation. Finally, with DAP-RARAP, the MTDs' EE is remarkable higher than in SAP-RARAP due to the smart uplink power level and proper access policy selection in the majority of the cases studied throughout this Master's Dissertation. All of that is obtained with a slight system's fairness increase.

Trade-offs: A clear trade-off exists between the adopted RA protocols and the adopted access policies. When access policies that use CSI are employed in SAP-RARAP, one can note a G gain in detriment of η_{T}. On the other hand, when DAP-RARAP is adopted, we note remarkable gains in the overall η_{MTD}, a slight increase in the system throughput and fairness in detriment of a huge loss in the total energy efficiency η_{T}. Especially about the fairness metric, we recall that the fairness increasing occurs in DAP-RARAP due to the reduction of the uplink power of MTDs at the red area, which causes a SE loss. These trade-offs are intrinsic to the system and must be taken into account in order to assess the desired system requirements.

mMTC Suitability: DAP-RARAP with appropriate policies (like CARP) better suits the needs of mMTC due to its adaptability, power efficiency, and superior performance in more complex environments. Under this suitability, one can enhance the devices' battery lifetime, avoiding frequent human interventions, which is crucial for mMTC scenarios.

Table 14 – Comparative analysis of access policies (SAP & DAP)

Variable	**Metric**	IRSAP	CRDSAP	s-SCP	CARP	**Observations**	
						SAP	DAP
Contending MTDs (K)	Throughput	Lower	Lower	Higher	Higher	CSI-aided policies outperform non-CSI policies.	DAP presented a higher throughput at higher K values and slightly outperforms SAP.
	Total EE	Higher	Higher	Lower	Lower	Non-CSI policies show higher EE due to the absence of training overhead.	The training step is mandatory, which augments the consumed power and harms the system EE.
	MTD's EE	Lower	Lower	Higher	Higher	Non-CSI policies have less energy consumption per MTD due to fewer packets replicas.	Significantly improved MTD EE due to adaptive uplink power and access policy.
MTD's Uplink Power (ρ_{MTD})	Throughput	Lower	Lower	Higher	Higher	Higher powers augments the throughput, but is unpractical for mMTC.	DAP's flexibility enables better performance at lower power levels.
	Total EE	Higher	Higher	Lower	Lower	Optimal EE varies depending on the access policy.	Similar to SAP, optimal total EE points vary but can not outperform SAP
	MTD's EE	Depends	Depends	Medium	Higher	Optimal MTD's EE varies with policy; higher values are observed at medium power.	Higher MTD's EE compared to SAP, particularly at lower uplink power levels.
	Fairness	Lower	Lower	Higher	Higher	When policy uses CSI, fairness is higher. Fairness augments with ρ_{MTD}.	Can achieve slightly better fairness than SAP due to the availability of ρ_{L} and ρ_{H}.
RIS Elements (N)	Throughput	Lower	Lower	Higher	Higher	CSI-based policies reaches plateaus faster than non-SCI-based ones.	Peak performance achieved at low N for all cases due to CSI availability.
	Total EE	Varies	Varies	Varies	Varies	Optimal EE occurs at a low # of RIS elements.	DAP can not outperform SAP due to the obligation of the training step.
	MTD EE	Varies	Varies	Varies	Varies	Lower MTD's EE due to the lack of power control	DAP easily outperforms SAP. Can be harmed with N if proper σ^2_{TH} are not informed to MTDs.
	Fairness	Varies	Lower	Higher	Varies	When policy uses CSI, fairness is higher. Fairness follows the shape of respective throughput curves	Can achieve slightly better fairness than SAP due to the availability of ρ_{L} and ρ_{H}.
Time Slots (S)	Throughput	Depends	Depends	Depends	Depends	If T_f is fixed, G tends to plateaus. On the contrary, each policy presents a specific maximum point.	Similar to SAP, with the maximum points being near to each other.
	Total EE	Depends	Depends	Depends	Depends	The same behavior of throughput curves is noted, with non-CSI-aided policies outperforming RIS-aided ones.	Similar as SAP curves, poor η_{T} performance when compared to SAP.
	MTD's EE	Depends	Depends	Depends	Depends	MTD's EE varies according to throughput and average number of replicas sent.	Easily outperforms SAP for higher S
Blockage Attenuation	Throughput	Decreases	Decreases	Decreases	Decreases	Policies with CSI show resilience to attenuation.	DAP exhibits better robustness compared to SAP.
	Total EE	Decreases	Decreases	Decreases	Decreases	EE decreases with increasing attenuation; non-CSI-aided policies suffer more severely.	Similar trend to SAP.
	MTD EE	Decreases	Decreases	Decreases	Decreases	MTD EE decreases with attenuation.	Similar trend to SAP.

6 CONCLUSIONS

This Master's Dissertation explores two novel random access protocols for B5G mMTC networks, effectively leveraging reconfigurable intelligent surfaces (RIS) to aid a specific group of users that suffers from poor channel conditions. A flexible wireless channel model for MTC and mMTC use modes were presented and validated, accurately capturing the characteristics of RIS-aided direct and reflected links, forming a robust basis for performance analysis. The variety of channel parameters, such as $\kappa_1, \kappa_2, \sigma$ and ξ allows the system designer to adapt such parameters according to the physical scenario's characteristics; hence, the expected performance can be precisely studied before the system deployment. Two new random access protocols were studied: SAP-RARAP and DAP-RARAP, where both of them can follows four access rules to perform uplink. The main difference between SAP and DAP strategies is that in DAP, MTDs are able to adapt their uplink power and access policy according to a calculated *localization coefficient*, which always requires CSI, while in SAP random access protocol, CSI is not always required, where both a single access policy rule and uplink power level selection are available. To evaluate the performance of the studied protocols, comprehensive numerical simulation results, obtained via Monte Carlo simulations were presented, providing valuable insights into the performance of both approaches. Specifically, the system throughput, total EE, MTD's EE, and fairness performance figure of merit were investigated according to a variety of system parameters, such as the number of contending MTDs, number of RIS elements, number of available time slots, MTD's transmit power, and blockage attenuation. The presented results reveal, in the majority of the studied scenarios, the superiority of DAP-RARAP in comparison to SAP-RARAP with respect to the throughput, MTDs' EE, and fairness performance metrics in detriment of a reduction in the total system EE and a higher computational complexity, which occurs due to the mandatory acquisition of CSI under DAP protocol, and the computation of the localization coefficients by MTDs, respectively. Despite that, one can say that DAP-RARAP seems like a promising approach for mMTC B5G networks due to the enormous achievable MTD's EE improvement, which is paramount for B5G IoT scenarios. These findings highlight the potential of RIS technology in meeting the growing demands of mMTC use mode services.

Future research should focus on even more sophisticated channel modeling, deeper investigations into the practical limitations of RIS hardware, advanced optimization algorithms for dynamic RIS configurations, and exploration of machine learning techniques for random access and decentralized adaptive resource management. These directions will pave the way for more efficient and sustainable mMTC solutions in 6G and beyond.

BIBLIOGRAPHY

[1] Recommendation ITU-R M.2410-0. *Minimum requirements related to technical performance for IMT-2020 radio interface(s)*. [S.l.], 2017.

[2] Recommendation ITU-R M.2083-0. *Framework and overall objectives of the future development of IMT for 2020 and beyond*. [S.l.], 2015.

[3] SANGUINETTI, L.; BJöRNSON, E.; HOYDIS, J. Toward Massive MIMO 2.0: Understanding Spatial Correlation, Interference Suppression, and Pilot Contamination. *IEEE Transactions on Communications*, v. 68, n. 1, p. 232–257, Jan 2020. ISSN 1558-0857.

[4] Recommendation ITU-R M.2160-0. *Framework and overall objectives of the future development of IMT for 2030 and beyond*. [S.l.], 2023.

[5] BJORNSON, E. et al. Massive MIMO is a reality–What is next? Five promising research directions for antenna arrays. *Digital signal processing*, Elsevier B.V, v. 94, p. 3, 2019. ISSN 1051-2004.

[6] NGO, H. Q. et al. Cell-Free Massive MIMO Versus Small Cells. *IEEE Transactions on Wireless Communications*, v. 16, n. 3, p. 1834–1850, March 2017. ISSN 1558-2248.

[7] ALWIS, C. D. et al. Survey on 6G Frontiers: Trends, Applications, Requirements, Technologies and Future Research. *IEEE Open Journal of the Communications Society*, v. 2, p. 836–886, 2021. ISSN 2644-125X.

[8] HASAN, M.; HOSSAIN, E.; NIYATO, D. Random Access for Machine-to-Machine Communication in LTE-Advanced Networks: Issues and Approaches. *IEEE Communications Magazine*, v. 51, n. 6, p. 86–93, June 2013. ISSN 1558-1896.

[9] BJöRNSON, E. et al. A Random Access Protocol for Pilot Allocation in Crowded Massive MIMO Systems. *IEEE Transactions on Wireless Communications*, v. 16, n. 4, p. 2220–2234, April 2017. ISSN 1558-2248.

[10] HAN, H.; GUO, X.; LI, Y. A High Throughput Pilot Allocation for M2M Communication in Crowded Massive MIMO Systems. *IEEE Transactions on Vehicular Technology*, v. 66, n. 10, p. 9572–9576, Oct 2017. ISSN 1939-9359.

[11] HAN, H.; LI, Y.; GUO, X. A Graph-Based Random Access Protocol for Crowded Massive MIMO Systems. *IEEE Transactions on Wireless Communications*, v. 16, n. 11, p. 7348–7361, Nov 2017. ISSN 1558-2248.

[12] MARINELLO, J. C.; ABRãO, T. Collision Resolution Protocol via Soft Decision Retransmission Criterion. *IEEE Transactions on Vehicular Technology*, v. 68, n. 4, p. 4094–4097, April 2019. ISSN 1939-9359.

[13] MARINELLO, J. C. et al. Achieving Fair Random Access Performance in Massive MIMO Crowded Machine-Type Networks. *IEEE Wireless Communications Letters*, v. 9, n. 4, p. 503–507, April 2020. ISSN 2162-2345.

[14] NISHIMURA, O. S.; MARINELLO, J. C.; ABRãO, T. A Grant-Based Random Access Protocol in Extra-Large Massive MIMO System. *IEEE Communications Letters*, v. 24, n. 11, p. 2478–2482, Nov 2020. ISSN 1558-2558.

[15] NISHIMURA, O. S. et al. Fairness in a Class Barring Power Control Random Access Protocol for Crowded XL-MIMO Systems. *IEEE Systems Journal*, v. 16, n. 3, p. 4574–4582, Sep. 2022. ISSN 1937-9234.

[16] CARVALHO, E. D. et al. Non-stationarities in extra-large-scale massive mimo. *IEEE Wireless Communications*, v. 27, n. 4, p. 74–80, August 2020. ISSN 1558-0687.

[17] FILHO, J. C. M. et al. Exploring the Non-Overlapping Visibility Regions in XL-MIMO Random Access and Scheduling. *IEEE Transactions on Wireless Communications*, v. 21, n. 8, p. 6597–6610, Aug 2022. ISSN 1558-2248.

[18] KUAI, X. et al. Coexistence of Human-Type and Machine-Type Communications in Uplink Massive MIMO. *IEEE Journal on Selected Areas in Communications*, v. 39, n. 3, p. 804–819, March 2021. ISSN 1558-0008.

[19] SANTOS, H. L. dos et al. Lstm-acb-based random access for mixed traffic iot networks. In: *2022 IEEE 8th World Forum on Internet of Things (WF-IoT)*. [S.l.: s.n.], 2022. p. 1–6.

[20] KUO, F. F. Computer networks—the aloha system. *JOURNAL OF RESEARCH of the National Bureau of Standards*, National Institute of Standards and Technology, v. 86, n. 6, p. 591, 1981.

[21] ROBERTS, L. G. Aloha packet system with and without slots and capture. *SIGCOMM Comput. Commun. Rev.*, Association for Computing Machinery, New York, NY, USA, v. 5, n. 2, p. 28–42, abr. 1975. ISSN 0146-4833. Disponível em: <https://doi.org/10.1145/1024916.1024920>.

[22] LIVA, G. Graph-based analysis and optimization of contention resolution diversity slotted aloha. *IEEE Transactions on Communications*, v. 59, n. 2, p. 477–487, February 2011. ISSN 1558-0857.

[23] TRALLI, V.; PAOLINI, E. IRSA-based Unsourced Random Access over Gaussian Channel. In: *2023 12th International Symposium on Topics in Coding (ISTC)*. [S.l.: s.n.], 2023. p. 1–5.

[24] HMEDOUSH, I. et al. Multi-Power Irregular Repetition Slotted ALOHA in Heterogeneous IoT networks. In: *2020 9th IFIP International Conference on Performance Evaluation and Modeling in Wireless Networks (PEMWN)*. [S.l.: s.n.], 2020. p. 1–6.

[25] LIU, J.; WANG, X. A Grant-Based Random Access Scheme with Low Latency for mMTC in IoT Networks. *IEEE Internet of Things Journal*, p. 1–1, 2023. ISSN 2327-4662.

[26] AHMED, S. F. et al. Toward a Secure 5G-Enabled Internet of Things: A Survey on Requirements, Privacy, Security, Challenges, and Opportunities. *IEEE Access*, v. 12, p. 13125–13145, 2024. ISSN 2169-3536.

[27] AKPAKWU, G. A. et al. A Survey on 5G Networks for the Internet of Things: Communication Technologies and Challenges. *IEEE Access*, v. 6, p. 3619–3647, 2018. ISSN 2169-3536.

[28] SOUZA, J. H. I. de et al. Energy Efficiency and Throughput of Random Access Protocols for RIS-Aided IoT Networks. In: *2022 IEEE 8th World Forum on Internet of Things (WF-IoT)*. [S.l.: s.n.], 2022. p. 1–6.

[29] RENZO, M. D. et al. Smart Radio Environments Empowered by Reconfigurable Intelligent Surfaces: How It Works, State of Research, and The Road Ahead. *IEEE Journal on Selected Areas in Communications*, v. 38, n. 11, p. 2450–2525, Nov 2020. ISSN 1558-0008.

[30] YOU, L. et al. Energy Efficiency and Spectral Efficiency Tradeoff in RIS-Aided Multiuser MIMO Uplink Transmission. *IEEE Transactions on Signal Processing*, v. 69, p. 1407–1421, 2021.

[31] HASSAN, N. U. et al. Efficient Beamforming and Radiation Pattern Control Using Stacked Intelligent Metasurfaces. *IEEE Open Journal of the Communications Society*, v. 5, p. 599–611, 2024.

[32] LI, H. et al. Beyond Diagonal Reconfigurable Intelligent Surfaces With Mutual Coupling: Modeling and Optimization. *IEEE Communications Letters*, v. 28, n. 4, p. 937–941, 2024.

[33] BJöRNSON, E. et al. Reconfigurable Intelligent Surfaces: A Signal Processing Perspective With Wireless Applications. *IEEE Signal Processing Magazine*, v. 39, n. 2, p. 135–158, March 2022. ISSN 1558-0792.

[34] RENZO, M. D. et al. Smart Radio Environments Empowered by Reconfigurable Intelligent Surfaces: How It Works, State of Research, and The Road Ahead. *IEEE Journal on Selected Areas in Communications*, v. 38, n. 11, p. 2450–2525, 2020.

[35] WU, Q. et al. Intelligent Surfaces Empowered Wireless Network: Recent Advances and the Road to 6G. *Proceedings of the IEEE*, v. 112, n. 7, p. 724–763, 2024.

[36] RENZO, M. D. Reconfigurable Surfaces for Wireless Communications. In: *2023 17th European Conference on Antennas and Propagation (EuCAP)*. [S.l.: s.n.], 2023. p. 1–2.

[37] JIANG, W. et al. Terahertz Communications and Sensing for 6G and Beyond: A Comprehensive Review. *IEEE Communications Surveys & Tutorials*, v. 26, n. 4, p. 2326–2381, 2024.

[38] CROISFELT, V. et al. A Random Access Protocol for RIS-Aided Wireless Communications. In: *2022 IEEE 23rd International Workshop on Signal Processing Advances in Wireless Communication (SPAWC)*. [S.l.: s.n.], 2022. p. 1–5. ISSN 1948-3252.

[39] SOUZA, J. H. I. de et al. Uplink Multiplexing of eMBB/URLLC Services Assisted by Reconfigurable Intelligent Surfaces. *IEEE Communications Letters*, v. 28, n. 9, p. 2206–2210, 2024.

[40] CROISFELT, V. et al. Random Access Protocol With Channel Oracle Enabled by a Reconfigurable Intelligent Surface. *IEEE Transactions on Wireless Communications*, v. 22, n. 12, p. 9157–9171, Dec. 2023.

[41] ROSS, C. et al. Engineering Reflective Metasurfaces With Ising Hamiltonian and Quantum Annealing. *IEEE Transactions on Antennas and Propagation*, v. 70, n. 4, p. 2841–2854, April 2022. ISSN 1558-2221.

[42] POLVANI, G.; SOUZA, J. H. Inacio de; ABRãO, T. Enabling Decentralized Access Policy Selection by Exploiting RIS-Induced Channel Diversity. In: *2024 19th International Symposium on Wireless Communication Systems (ISWCS)*. [S.l.: s.n.], 2024. p. 1–6. ISSN 2154-0225.

[43] CHEN, Z. et al. Energy Efficiency Optimization for Irregular Repetition Slotted ALOHA-Based Massive Access. *IEEE Wireless Communications Letters*, v. 11, n. 5, p. 982–986, 2022.

[44] CASINI, E.; GAUDENZI, R. D.; HERRERO, O. D. R. Contention Resolution Diversity Slotted ALOHA (CRDSA): An Enhanced Random Access Scheme for Satellite Access Packet Networks. *IEEE Transactions on Wireless Communications*, v. 6, n. 4, p. 1408–1419, 2007.

[45] JAIN, R.; CHIU, D. M.; WR, H. A Quantitative Measure Of Fairness And Discrimination For Resource Allocation In Shared Computer Systems. *CoRR*, cs.NI/9809099, 01 1998.

[46] RAAB, F. et al. Power amplifiers and transmitters for RF and microwave. *IEEE Transactions on Microwave Theory and Techniques*, v. 50, n. 3, p. 814–826, 2002.

[47] EARTH Deliverable 2.3. *Energy efficiency analysis of the reference systems, areas of improvements and target breakdown*. [S.l.], 2010. Available at: <https://cordis.europa.eu/docs/projects/cnect/3/247733/080/deliverables/001-EARTHWP2D23v2.pdf>.

[48] ANDERSSON, C. et al. Improving energy performance in 5G networks and beyond. *Ericsson Technology Review*, Ericsson, v. 2022, n. 8, p. 2–11, 2022.

[49] MARTINEZ, B. et al. The Power of Models: Modeling Power Consumption for IoT Devices. *IEEE Sensors Journal*, v. 15, n. 10, p. 5777–5789, 2015.

[50] RAPPAPORT, T. S. *Wireless Communications: Principles and Practice*. 2nd. ed. Upper Saddle River, NJ, USA: Prentice Hall, 2002.

[51] GOLDSMITH, A. *Wireless Communications*. Cambridge, UK: Cambridge University Press, 2005.

[52] MOLISCH, A. F. *Wireless Communications*. 2nd. ed. Hoboken, NJ, USA: Wiley-IEEE Press, 2011.

[53] 3rd Generation Partnership Project (3GPP). *Study on channel model for frequencies from 0.5 to 100 GHz*. Sophia Antipolis, France, 2019.

[54] International Telecommunication Union. *Propagation data and prediction methods for the planning of indoor radio communication systems and radio local area networks in the frequency range 900 MHz to 100 GHz*. Geneva, Switzerland, 2017.